

Turbulence
and
Low-Level Jets
in the
Stable Boundary Layer

Peter Baas

Thesis committee**Thesis supervisor**

Prof. dr. A.A.M. Holtslag
Professor of Meteorology
Wageningen University

Thesis (co)supervisor

Dr. F.C. Bosveld
Senior Scientist
KNMI, De Bilt

Other members

Dr. A.C.M. Beljaars, ECMWF, Reading, England
Dr. F. Beyrich, Deutsche Wetter Dienst, Lindenberg, Germany
Prof. dr. M.C. Krol, Wageningen Universiteit, Stichting voor Ruimteonderzoek
Nederland, Utrecht
Prof. dr. A.P. Siebesma, KNMI, De Bilt, Technische Universiteit Delft

This research was conducted under the auspices of the Buys-Ballot Research
School

Turbulence and Low-Level Jets in the Stable Boundary Layer

Peter Baas

Thesis

submitted in partial fulfillment of the requirements for the degree of doctor
at Wageningen University
by the authority of the Rector Magnificus
Prof. dr. M.J. Kropff,
in the presence of the
Thesis Committee appointed by the Doctorate Board
to be defended in public
on Wednesday 14 October 2009
at 4 PM in the Aula.

Peter Baas

Turbulence and Low-Level Jets in the Stable Boundary Layer, 152 pages.

Thesis, Wageningen University, Wageningen, NL (2009)

With references, with summaries in Dutch and English

ISBN 978-90-8585-446-3

Abstract

During nighttime the atmospheric boundary layer is in general stably stratified due to radiative cooling of the surface. Often, at the top of this stable boundary layer (SBL) a maximum in the wind speed develops, named the low-level jet (LLJ). In weather and climate models, a realistic parameterization of turbulent mixing for stably stratified conditions is crucial for a correct representation of vertical profiles of temperature and wind and of phenomena like the LLJ. The complex interactions between different processes complicate modeling of the SBL, especially in weak wind conditions. The aim of this thesis is to improve the understanding of SBL processes and their representation in atmospheric models, in particular turbulent mixing and the formation of the nocturnal LLJ.

Characteristics of the LLJ are derived by analyzing seven years of data from the Cabauw measurement site (The Netherlands). It was found that in about 20% of the nights a maximum in the wind speed profile occurs. LLJs are typically situated at 140 to 200 m above the surface and have a speed of 6 to 10 m s⁻¹. A classification was made in terms of the two main forcings of the SBL, i.e. the geostrophic wind and radiative cooling. The development of a significant LLJ is most likely for moderate geostrophic forcing and high radiative cooling.

The turbulence formulation in atmospheric models often contains semi-empirical relations derived from field experiments, for instance the frequently applied flux-gradient relations. It is demonstrated that these relations are seriously affected by self-correlation, a mathematical phenomenon that spuriously masks spread in scatter plots. This may lead to false confidence in the obtained relations.

Different turbulence formulations are tested in a single-column model (SCM). The scaling behavior of a TKE closure scheme was analyzed in terms of traditional Monin-Obukhov Similarity Theory and local scaling. It turned out that the TKE scheme strictly follows local scaling theory. Together with a sensitivity study to relevant parameters of the TKE scheme, this improved the understanding of the model, which enables a more realistic choice of the values of these parameters.

SCMs are widely employed to evaluate boundary layer parameterizations by comparing model results to observations. These models must be driven by the large scale forcing on the column. To investigate the effect of these inherently uncertain forcings on the model results, a sensitivity study is performed to both the forcings and the turbulence formulation. The sensitivity of the SCM results to the turbulence formulation is largest in the bulk of the SBL, while the influence of the forcings manifests itself mainly in the upper part of the SBL and above. In addition, it is shown that SCM comparison studies based on multiple cases enable a better judgment of the quality of boundary layer parameterizations.

Table of contents

1	Introduction	1
1.1	The atmospheric boundary layer	1
1.2	Characteristics of the stable boundary layer	3
1.3	Modeling SBL turbulence	9
1.4	The SBL and large-scale models	13
1.5	Evaluation studies	16
1.6	Goals and set-up of thesis	18
2	A Climatology of Nocturnal Low-Level Jets at Cabauw	21
2.1	Introduction	21
2.2	Mechanisms	23
2.3	Site characteristics and observations	25
2.4	Criteria for LLJ detection	27
2.5	Classifying SBL observations	29
2.6	Climatology of LLJs	32
2.7	Comparison with ERA40 climatology	40
2.8	Concluding remarks	42
3	Exploring Self-Correlation in Flux-Gradient Relationships for Stably Stratified Conditions	45
3.1	Introduction	45
3.2	Monin-Obukhov similarity theory	47
3.3	Observational data	48
3.4	Influence of self-correlation on flux-gradient relationships	49
3.5	Stability dependence of self-correlation	53
3.6	Randomizing real observations	55
3.7	Discussion and future research	57
3.8	Conclusions	57
	Appendix 3A: Sensitivity of flux-gradient relationships for changes in the momentum and the heat flux	59
4	The Scaling Behaviour of a Turbulent Kinetic Energy Closure Model for Stably Stratified Conditions	61
4.1	Introduction	61
4.2	Background	63
4.3	Model description	66
4.4	Analytical solution for the stable limit of the TKE model	68

4.5	Comparison of the analytical solutions with model simulations of the TKE model	72
4.6	Discussion	79
4.7	Conclusions	81
5	How to Design Single-Column Model Experiments for Comparison with Observed Nocturnal Low-Level Jets?	83
5.1	Introduction	83
5.2	Model description	85
5.3	Introduction to the case and set-up of simulations	87
5.4	Sensitivity analysis using the GABLS3 set-up	89
5.5	Composite case	99
5.6	Conclusions	105
	Appendix 5A: Dynamical forcings for SCM integrations from RACMO2	107
6	Summary, Reflections and Outlook	109
6.1	Summary	109
6.2	Reflections	112
6.3	Perspectives	119
6.4	Final remarks	121
	Reference list	123
	Nederlandse samenvatting	139
	Dankwoord	143
	Curriculum Vitae	145
	Publications	146
	Buys-Ballot Research School Education Plan Activities	147

1 Introduction

“From our first breath, we spend most of our lives near the Earth’s surface. We feel the warmth of the daytime sun and the chill of the nighttime air. It is here where our crops are grown, our dwellings are constructed, and much of our commerce takes place. We grow familiar with our local breezes and microclimates, and we sense the contrasts when we travel to other places.”
(Stull, 1988)

The subject of this thesis is the nocturnal stable boundary layer (SBL) over land, in particular turbulent mixing and the formation of the nocturnal low-level jet (LLJ). These processes typically interact with each other, since the amount of turbulence in the SBL impacts on the LLJ characteristics, while the presence of a LLJ can influence the turbulent structure of the SBL below.

In this first chapter a general introduction is given on the boundary layer and its daily cycle. Next, the major processes in the SBL are summarized. An overview of the various forms of turbulent mixing parameterizations that have been applied in SBL modeling will be presented. Subsequently, the role of the SBL in large-scale atmospheric models is discussed, and the concept of single-column modeling is introduced. Finally, the goals and set-up of this thesis are formulated.

1.1 The atmospheric boundary layer

The atmospheric boundary layer (ABL) is commonly defined as the lowest part of the atmosphere that is directly influenced by the presence of the Earth’s surface and responds to surface changes with a time scale of about an hour or less (e.g. Stull, 1988). The surface warms and cools in response to received and emitted radiation. In turn, the surface forces the ABL by transport processes of which turbulence is the most important.

The ABL is characterized by large diurnal variations in temperature, wind and humidity. Figure 1.1 shows observations of potential temperature and wind speed from the 200 m measuring tower at Cabauw. (Note that the potential temperature, θ , equals the actual temperature, T , that an air parcel would acquire if brought adiabatically to a reference pressure.) Figure 1.1a shows that during daytime, the difference in θ between 10 and 200 m is small. The warmed air parcels close to the ground have a lower density than the overlying air. As a result, convective thermals rise from the surface to the upper part of the ABL: they are called positively buoyant. In this way heat, moisture and momentum are

transported very efficiently to the upper parts of the ABL. Vigorous turbulent mixing causes the potential temperature to be almost constant with height. Also the wind in the daytime boundary layer is relatively well-mixed, although less effective than temperature, because turbulent motions are primarily driven by vertical differences in θ .

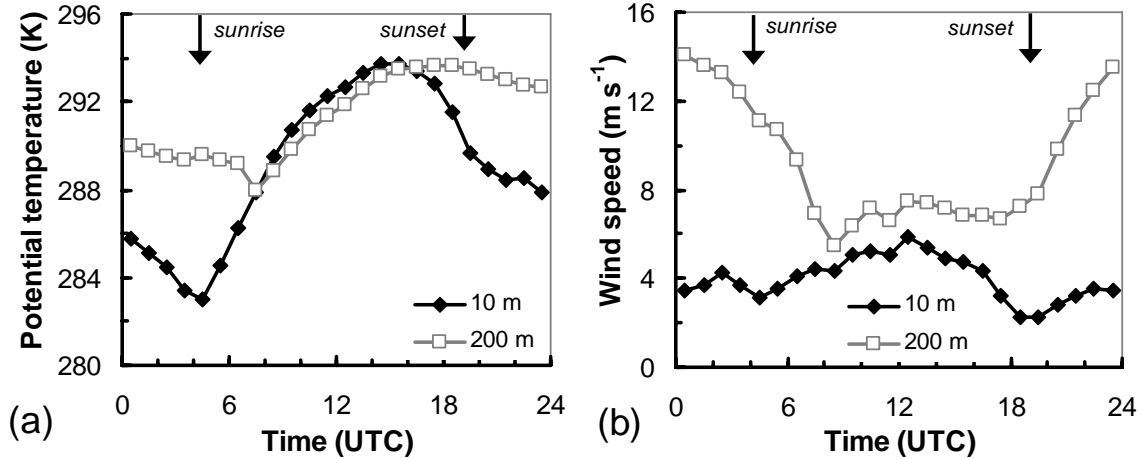


Figure 1.1: Diurnal cycle of potential temperature (a) and wind speed (b) as observed on 5 May 2008 at 10 and 200 m height in the Cabauw tower.

Already a few hours before sunset the near-surface temperature starts to drop. By the end of the afternoon the decreasing shortwave radiation from the sun does not compensate anymore for the loss of thermal radiation at the surface. Consequently, heat is extracted from the lower part of the ABL, which therefore starts to cool as well. During the night the coldest air is situated close to the ground. Air parcels that move upward are heavier than the surrounding air, while downward moving parcels are lighter than their environment. As a result, they tend to move back to their original position and vertical movements are suppressed. The ABL is said to be stably stratified, hence the name stable boundary layer (SBL).

The upper part of this stably stratified layer does not ‘feel’ the presence of the surface anymore. As a result the wind at 200 m accelerates after sunset (Figure 1.1b); due to a dynamical effect a maximum in the vertical wind speed profile arises at the top of the SBL, above which the wind speed decreases again. This phenomenon is called the nocturnal low-level jet (LLJ). Its speed can be larger than the geostrophic wind speed, which is the (theoretical) large-scale wind derived from the horizontal pressure gradient.

Figure 1.2 presents a conceptual picture of the diurnal cycle of the ABL. The daytime ABL is called the convective boundary layer (CBL) and has a typical

depth of 1 to 2 km. The CBL is bounded at the top by the capping inversion, which marks the transition to the free atmosphere above. After sunset the SBL forms adjacent to the surface. Since the stable stratification inhibits vertical motions, the SBL is much shallower than the CBL, typically 100 to 300 m. Above the SBL, the air that is not influenced by the surface cooling is called the residual layer. In this layer θ is almost constant with height. The surface layer is the bottom part of the ABL (usually taken as the lowest 10%) in which the turbulent transport is approximately constant with height.

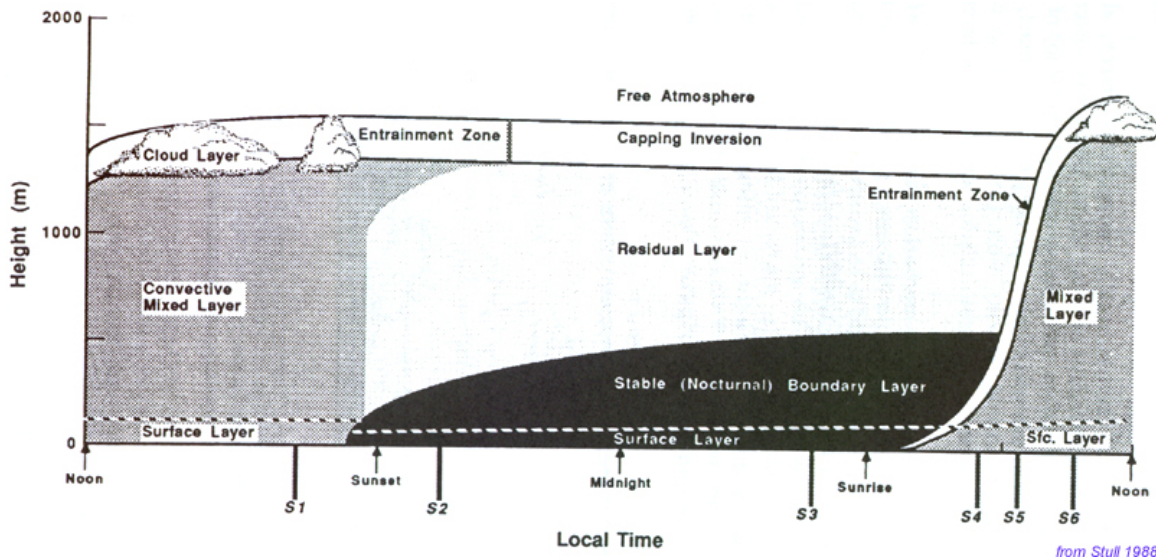


Figure 1.2: Conceptual picture of the ABL diurnal cycle (from Stull, 1988).

1.2 Characteristics of the stable boundary layer

The structure of the SBL is mainly determined by two external forcings: the geostrophic wind speed and the net long-wave cooling of the surface. The latter depends mainly on the cloudiness. The most stable conditions occur for weak geostrophic forcing in combination with clear skies. In this case the SBL consists of only a shallow layer, which is characterized by a strong inversion. When the geostrophic wind is strong and the presence of clouds reduces the radiative loss to space, the SBL is much deeper and only weakly stratified.

During nighttime turbulence is much weaker than during daytime. It often occurs in isolated patches and is not continuous, especially when the winds are weak. For this reason, other processes become relatively more important in the SBL compared to the daytime boundary layer. These processes include radiation divergence, gravity waves, surface interactions, and moist processes. The interactions between all these processes are not fully understood. This is what makes modeling of the SBL still a challenge (e.g. Beljaars, 1995; Holtslag, 2006;

Steenefeld, 2007; Brown et al., 2008; Chapter 1.4). This subsection briefly describes relevant processes and phenomena that play a role in the SBL.

1.2.1 Turbulence

Turbulence is a key process in the ABL. Turbulent flow consists of chaotic motions of eddies of different sizes superimposed on each other. The formation of the largest eddies extracts energy from the mean flow. These large eddies are unstable and break up into smaller eddies. In this way, turbulent energy ‘cascades’ to smaller and smaller scales. Finally, the smallest eddies ($O \sim 1$ mm, Kolmogorov scale) are dissipated by molecular viscosity to heat.

Turbulent kinetic energy (TKE) is a measure of the intensity of turbulence. Wind shear and buoyancy effects are two important components of the TKE budget. Vertical differences in the wind speed generate turbulent motions. Because at the surface friction forces the wind speed to zero, this mechanical production of turbulence is largest close to the ground. Buoyancy is the tendency of an air parcel to float or rise in a gravitational field due to density differences with the surrounding air. Density differences are directly related to differences in virtual temperature, T_v , which is the temperature dry air would have if its pressure and density were equal to a given sample of moist air. Hence, variations in virtual temperature can be used instead of density differences. Since turbulence involves vertical motion, in practice the virtual potential temperature, θ_v , is used. Buoyancy effects can act both as a source and as a sink for turbulent energy, depending on stability. In the unstable mixed layer, rising thermals generate turbulent motions. Contrary, in stable conditions the turbulent vertical motions are acting against the restoring force of gravity. Thus, buoyancy tends to suppress turbulence. To summarize, during nighttime the amount of TKE results from a *competition* between wind shear, which tends to produce turbulence, and buoyancy, which tends to suppress turbulence. During daytime both processes *cooperate* in producing turbulence.

The ratio between shear production and the buoyancy destruction of turbulence is a measure of the stability. This ratio is called the flux Richardson number, Ri_f . In practice the gradient Richardson number, Ri_g is much more commonly used, for example, in many atmospheric models. It assumes that turbulent fluxes are proportional to the local mean vertical gradients (cf. Chapter 1.3):

$$Ri_g = \frac{\frac{g}{\theta_v} \frac{\partial \theta_v}{\partial z}}{\left(\frac{\partial U}{\partial z} \right)^2}, \quad (1.1)$$

where U denotes the wind speed and g the acceleration due to gravity.

In the literature, much discussion exists on whether there is a critical, maximal value of Ri_g above which no turbulent motions can persist. This threshold value is called the critical Richardson number, Ri_c . Many studies show a dramatic decrease of turbulent activity around $Ri_g = 0.25$ (e.g. Mahrt et al., 1998; Mauritsen et al., 2007; Zilitinkevich et al., 2007). This is close to the traditional value of Ri_c (Miles, 1961). It appears that beyond $Ri_g = 0.25$ no continuous, stationary turbulence can be maintained. However numerous studies show that for values of Ri_g much larger than 0.25 turbulent activities are present.

In literature, often a distinction is made between weakly stable and very stable conditions (e.g. Mahrt et al. 1998, Van de Wiel et al., 2003; Steeneveld et al., 2006). The weakly stable regime is characterized by strong winds and cloudy conditions. Shear generation of turbulence is large and radiative cooling of the surface is small. Turbulence is continuous and the structure of the SBL is dominated by turbulent processes. On the other hand, the very stable regime is characterized by clear skies and light wind conditions. Since in these conditions turbulence is very weak, the SBL structure is mainly determined by radiative flux divergence and the soil heat flux. Most studies separate the weakly stable and the very stable regimes by a transition regime. In this regime turbulent activity shows a rapid decrease with stability. Periods of turbulent activity alternate with periods of weak or immeasurably small fluctuations (Mahrt, 1999). The SBL is called intermittently turbulent (Van de Wiel, 2002).

The different character of the weakly stable and the very stable regime can be illustrated by considering the feedbacks between the temperature gradient and the heat flux (Van de Wiel et al., 2007). In case of a weakly stable stratification a sudden increase in the vertical temperature gradient will generally be followed by an increase in the vertical heat flux. The increased flux tends to restore the original weaker stratification. Hence, there is a *negative* feedback between the stratification and the heat flux. However, for stronger stabilities vertical motions are gradually more suppressed. At some point the stratification may be so large that in response to an additional increase the heat flux will become smaller. The lower heat flux causes a further strengthening of the stratification, and so on. In this very stable regime a *positive* feedback exists between the stratification and the heat flux. The stratification is so strong that turbulence cannot support anymore the heat flux demanded by the surface net radiative cooling. It is said that the SBL is decoupled from the surface. The above reasoning implies that there exists a maximum value of the heat flux (see e.g. Van Ulden and Holtslag, 1985; Derbyshire, 1990; Basu et al., 2008).

1.2.2 Other processes

The temperature profile in the SBL is not only determined by turbulent processes. Especially in weak-wind conditions, also **long-wave radiative flux divergence** plays a role (Garratt and Brost, 1981; Edwards, 2009). The net longwave radiation at a certain level is determined by the upward radiation from the surface and from the underlying air and the downward radiation received from the overlying air (Garratt and Brost, 1981). The first hours after the evening transition radiation divergence dominates the evolution of the near-surface air temperature (Edwards, 2009; Steeneveld et al, 2008c). Atmospheric constituents like water vapor and CO₂ play an important role in the radiation budget. In the residual layer radiation divergence causes a weakly stable stratification (André and Mahrt, 1982).

Stably stratified flows can support **buoyancy or gravity waves** (Chimonas and Nappo, 1989). Especially when turbulence is weak, the SBL is filled with gravity waves. Since gravity waves cannot propagate through a neutral stratification they are damped in the residual layer or reflected back to the surface. Thus the waves are trapped between neutral layers aloft and the surface, resulting in horizontally propagating waves. Breaking of gravity waves may generate additional drag. Over complex terrain, this gravity wave drag may be larger than the conventional drag associated with turbulence (Steeneveld et al., 2008b).

As the temperature decreases after sunset, the relative **humidity** in the SBL increases. When the air is dry and the surface wet, evaporation can continue during the night. On many nights, the surface cools to saturation and moisture from the air condensates to the surface as **dew**. For a grassland area in the center of The Netherlands, Jacobs et al. (2006) estimated the annual amount of dew to be 37 mm. When the air close to the ground cools below the dew point temperature, moisture may condensate in the air forming radiation **fog** (Duynderke, 1991; Van de Velde et al., 2009). Initially, the highest concentration of liquid water is close to the surface. When gradually more water condensates the fog layer becomes less transparent for radiation. Then, the level at which the radiative cooling occurs shifts from the surface to the top of the fog layer. This destabilizes the fog layer, which, as a result, becomes well-mixed.

Surface heterogeneity complicates the development of the SBL. Surface roughness determines the amount of drag experienced by the flow. When the flow experiences a sudden roughness change (e.g. from forest to open fields) an internal boundary layer develops. In this case wind profiles often show a discontinuity at some level above the surface (Verkaik and Holtslag, 2007). For stably stratified conditions the disturbing effects of roughness elements are felt over longer distances than in daytime conditions. Thermal heterogeneity of the surface can cause additional turbulence in the SBL. When cold or warm patches are present,

mesoscale circulations may develop. Sometimes, this is visualized when patches of fog rise from relatively warm ditches over the cooler neighboring meadows.

The characteristics of the underlying **soil** influence the cooling rate of the surface layer. At night heat is transported upwards in the soil, (partly) compensating for the radiative loss at the surface. In light wind conditions, when turbulence in the SBL has diminished, this soil heat flux balances the negative net radiation. The soil heat flux depends on the thermal conductivity and the temperature gradient in the soil. A low conductivity means a lower soil heat flux, which results in faster decrease of the surface temperature. Dry soils have a lower conductivity than wet soil. Snow layers and vegetation isolate the air from the soil, resulting in lower temperatures at the surface.

1.2.3 Low-level jet

The vertical profile of wind speed often shows a supergeostrophic maximum at the top of the nocturnal SBL, called the low-level jet (LLJ). The term was introduced by Means (1952) to describe a strong narrow air stream at low levels in the south-central part of the United States. The LLJ is one of the main topics of this thesis. The term ‘low-level *jet*’ might suggest that this phenomenon is not only confined in the vertical, but also in the horizontal plane. However, this is not the case: LLJs can extend over large areas. In fact, it is more like a low-level sheet of high wind velocities. One could argue that terms like ‘boundary layer wind maximum’ (Blackadar, 1957) or ‘inversion wind maximum’ should be preferred (e.g. Stensrud, 1996), but this terminology has never been widely used in literature.

Nocturnal LLJs originate from the diurnal cycle of turbulence in the ABL (Blackadar, 1957). In the ABL, during daytime the pressure gradient force, F_p , is balanced by the Coriolis force, $F_{c,0}$, and friction, F_f (Figure 1.3a). Friction causes the wind vector in the CBL, indicated in Figure 1.3 by V_0 , to be directed towards low pressure. The wind speed is subgeostrophic. Around sunset the large eddies in the CBL dissipate quickly. Figure 1.3b illustrates what happens during the night. Above the developing turbulent SBL friction has disappeared. The air in this layer is decoupled from the surface. As a result, the balance of forces is not in equilibrium anymore and the wind in the residual layer starts to accelerate. Because the Coriolis force is proportional to the wind speed and directed towards the right (northern hemisphere), the wind vector will start to rotate clockwise around the geostrophic wind vector (indicated by \mathbf{V}_g). Figure 1.3b presents the situation a time t after the moment of decoupling: the wind vector has moved from V_0 to V_t , the Coriolis force from $F_{c,0}$ to $F_{c,t}$. The amplitude of the oscillation equals the magnitude of the ageostrophic wind component at the moment of decoupling, which is determined by the amount of friction in the preceding CBL. The period of oscillation is given by $2\pi/f$, which amounts to 15.2 hours for The Netherlands or

52° N. Here $f = 2\Omega \sin\phi$ denotes the Coriolis parameter, where $\Omega = 7.29\text{E-}5 \text{ rad s}^{-1}$ is the angular velocity of the Earth and ϕ is the latitude. The characteristics of the LLJ depend on the structure of the SBL below. On the other hand, enhanced shear below the jet may affect the turbulent properties of the SBL (Banta et al., 2006).

Inertial oscillations are not the only mechanism that can generate LLJs. They can also be formed by baroclinicity, when the geostrophic wind speed decreases with height due to horizontal temperature differences. Baroclinicity may result from land-sea contrasts, from sloping terrain or from frontal systems.

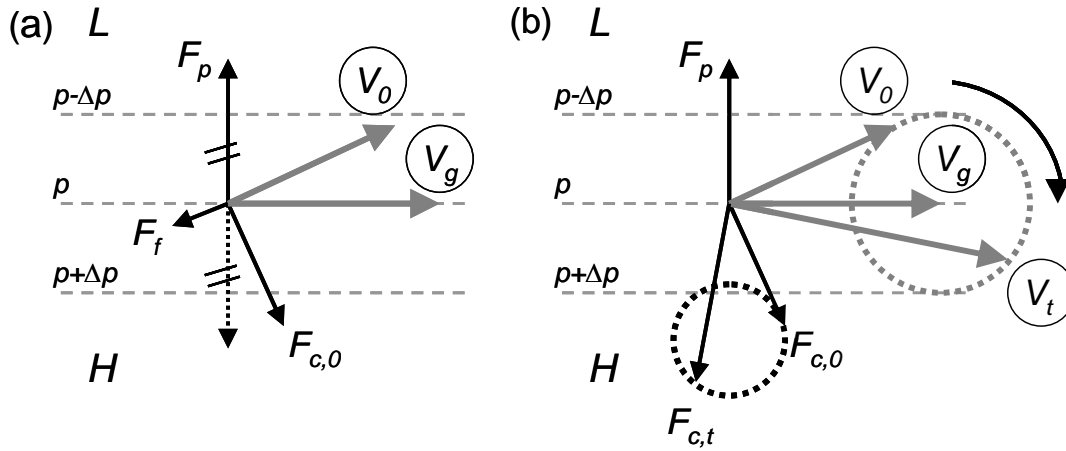


Figure 1.3: Development of the nocturnal LLJ over land. (a) Balance of forces during daytime conditions. (b) Inertial oscillation produces supergeostrophic winds during the night. Symbols are explained in the text.

1.2.4 SBL and society

Since most human activity takes place in the ABL, a reliable forecast of near-surface weather is of vital importance. This paragraph gives examples how SBL phenomena impact on society.

Decreased visibility during fog episodes leads to potentially dangerous situation in (air)traffic. When the temperature cools below the freezing point in combination with precipitation (snow, freezing rain) roads become slippery, causing traffic jams and lots of accidents. Frost damage in orchard can devastate fruit harvests. The large shear below the LLJ influences the lift of aircrafts and flights of hot air balloons. LLJs may be very beneficial for the energy output of wind turbines (Storm et al., 2009). On the other hand, the enhanced vertical shear may have detrimental effects on the turbine rotors. The supergeostrophic winds in LLJs can transport pollutants over large distances (Beyrich, 1994).

Air pollution is trapped below the nocturnal inversion (Salmond and McKendry, 2005). Consequently, concentrations of trace gases build up during the night. At morning rush hour high peaks in concentrations of pollutants are

observed. For modeling the spread and concentration of pollutants a reliable prediction of the height of the SBL is important (e.g. Steeneveld et al., 2007)

These examples underline the importance of an accurate prediction of the SBL. To enable such a forecast, the relevant processes and their interactions must be well understood. This is also true for climate models, in which the representation of SBL processes is rather poor.

1.3 Modeling SBL turbulence

1.3.1 Turbulent transport

Time-series of, e.g., wind and temperature show fast fluctuations in time. These are characteristic for turbulence processes. Reynolds (1895) decomposed the flow into a mean and a fluctuating turbulent part. For example, the vertical velocity, w , and the potential temperature, θ , can be written as

$$\begin{aligned} w &= \bar{w} + w' \\ \theta &= \bar{\theta} + \theta' \end{aligned} \quad (1.2)$$

Here the overbars represent time-average values, the primes indicate fluctuations from the mean. The covariance between w and θ is defined as the averaged product of the fluctuations: $\overline{w'\theta'}$. This quantity can be interpreted as the vertical turbulent transport of temperature (heat) through a horizontal plane and is called a turbulent flux. It is the divergence of the flux that provides the time tendency for the mean profile due to turbulence.

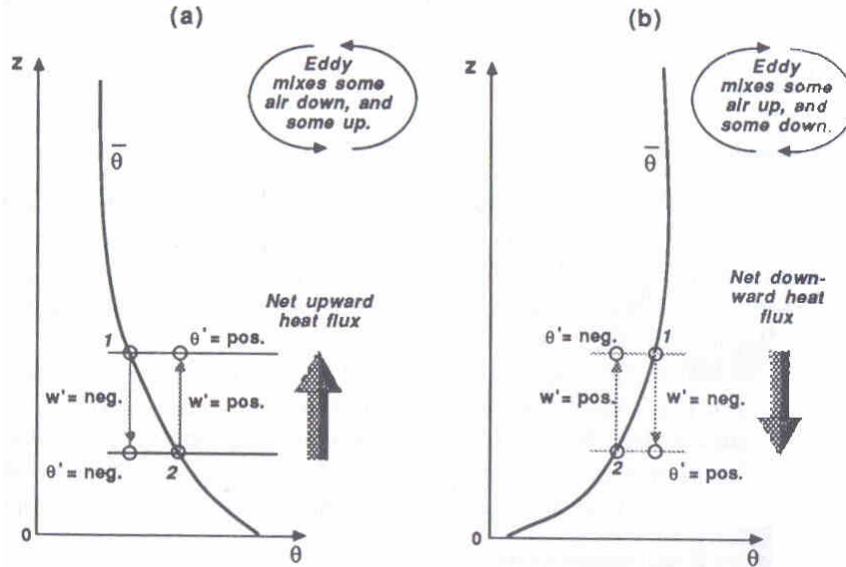


Figure 1.4: Idealization of the mixing process. (a) A net upward turbulent heat flux in an unstable environment. (b) A net downward turbulent heat flux in a stable environment. (From Stull, 1988.)

Figure 1.4 illustrates the concept of a turbulent flux and explains the role of stability. When an air parcel is moved vertically, its potential temperature stays constant. When the stratification of the ambient air is unstable (left panel), the perturbations w' and θ' have equal sign, resulting in net positive values for the turbulent heat flux. In this case heat is transported upwards. In the right panel the ABL is stably stratified. Now the perturbations have opposite sign and the heat flux is directed downwards.

1.3.2 The closure problem

When Reynolds' averaging is applied to the governing equations for a turbulent flow, the resulting equations contain *additional terms* representing the effect of turbulence on the mean flow. Unfortunately, the set of averaged equations contains now more unknown variables than equations. Deriving expressions for the unknown turbulent fluxes does not solve the problem. Instead, this approach results in even more unknowns. The inability to close the system of equations is known as the closure problem.

The closure problem prevents a solution of the atmospheric equations. To close the set of equations, the unknown variables have to be expressed in terms of the knowns. In literature, numerous examples of closure approximations and parameterizations for the unknown variables can be found.

1.3.3 Parameterization of turbulence

Analogous to molecular diffusion, in 1877 Boussinesq suggested that the magnitude of turbulent transport of a quantity, ψ , is proportional to the local mean gradient of this variable (e.g. wind, temperature, moisture, CO₂, etc):

$$\overline{w'\psi'} = -K_\psi \frac{\partial \psi}{\partial z}. \quad (1.3)$$

The constant of proportionality, K , is called eddy diffusivity. Prandtl (1925) refined this model by making K a function of a mixing length, l , and the wind shear:

$$K_\psi = l_\psi^2 \frac{\partial U}{\partial z}, \quad (1.4)$$

The length scale, l can be interpreted as the typical distance an air parcel moves before mixing with its environment (Stull, 1988). Note that in reality mixing occurs over a spectrum of distances. Close to the surface, the length scale is typically parameterized as

$$l_\psi = kz. \quad (1.5)$$

The constant k denotes the Von Kármán constant, mostly taken as 0.4 (Högström, 1996) and z indicates the height above the surface.

Obukhov (1946) realized that the dynamics of a horizontally homogeneous and stationary turbulent flow is fully characterized by its surface friction velocity, u_{*0} , and its surface buoyancy flux, $\overline{w'\theta'_{v0}}$. From this he derived a typical length scale, L , which became later known as the Obukhov length:

$$L = -\frac{u_{*0}^3}{k \frac{g}{\theta_v} \overline{w'\theta'_{v0}}}, \quad (1.6)$$

The subscript 0 refers to surface values of the fluxes. The magnitude of L indicates the height above the surface at which the buoyancy production of turbulence first dominates the mechanical (shear) production of turbulence. The dimensionless height z/L is a measure of stability. Monin and Obukhov (1954) analyzed turbulent mixing in the surface layer, where apart from the distance to the surface no other length scales (like the boundary layer height or the vegetation height) play a role. By systematically applying similarity theory, they showed that all dimensionless turbulent variables are a function of the stability parameter z/L . Monin-Obukhov Similarity Theory (MOST) is well-established for the surface layer, where the fluxes can be considered constant with height.

Nieuwstadt (1984) extended the surface layer based MOST by demonstrating that above the surface layer the *local* Obukhov length, Λ , is the relevant scaling parameter. It is equal to the ordinary Obukhov length, except that local fluxes are used instead of surface fluxes. Now, dimensionless parameters are a function of z/Λ . The dimensionless wind gradient can be written as

$$\frac{kz}{u_*} \frac{\partial U}{\partial z} = \phi_m = f\left(\frac{z}{\Lambda}\right). \quad (1.7)$$

Similar relations can be formulated for temperature, humidity and trace gases. These so-called flux-gradient relations or ϕ -functions must be determined from field experiments. For weakly stable stratification ($z/\Lambda < \sim 1$) a clear linear dependence is found. Both ϕ_m and ϕ_h are reasonably represented by the relation $\phi_{m,h} = 1 + 5z/\Lambda$ (cf. Dyer, 1974). Recent results obtained by direct numerical simulation suggest that these functions are also valid for continuous, stationary turbulence for stronger stabilities (Van de Wiel et al., 2008). However, for increasing stability, continuous and stationary turbulence is rarely observed in observational records. For this reason, the flux-gradient relations tend to level-off for stronger stabilities (Mahrt, 2007). In this regime problems arise with flux measurements, time averaging (Vickers and Mahrt, 2003) and contamination by non-turbulent processes like radiative flux divergence and gravity waves. Not surprisingly, for this very stable conditions proposed formulations for the flux-gradient relations diverge widely in the literature. Moreover, Chapter 3 of this

thesis demonstrates that the flux-gradient relations are seriously affected by self-correlation.

Once a functional relation for the flux-gradient relations is known, it can be used to correct K for stratification:

$$K_\psi = \frac{l_\psi^2}{\phi_m \phi_\psi} \frac{\partial U}{\partial z}. \quad (1.8)$$

Mostly, the ϕ -functions are written in terms of Ri_g , making use of the relation

$$Ri_g = \frac{z}{\Lambda} \frac{\phi_h}{\phi_m^2}. \quad (1.9)$$

This type of turbulence closure is called first-order closure because only the mean variables are resolved in the model, while all turbulent fluctuations are parameterized.

In a more advanced approach, K is made a function of turbulent kinetic energy (TKE or E):

$$K_\psi = l_\psi \sqrt{E}. \quad (1.10)$$

In this approach, the TKE is resolved by the prognostic TKE equation (Cuxart et al. 2000). The premise is that introducing more advanced physics results in a better parameterization of K . Since only a part of the second order moments is resolved, this type of closure is called one-and-a-half order closure. For TKE-closure schemes, the formulation of the length scale plays a crucial role (Weng and Taylor, 2003). Many proposals are made in literature, especially for unstable conditions (e.g. Bougeault and Lacarrère, 1989; Lenderink and Holtslag, 2004). For stable conditions the length scale proposed by Deardorff (1980) is frequently used:

$$l_s = c_{m,h} \frac{\sqrt{E}}{\sqrt{\frac{g}{\theta_v} \frac{\partial \theta_v}{\partial z}}}, \quad (1.11)$$

where, $c_{m,h}$ are free model parameters. Compared to first-order schemes, TKE closure schemes allow for a more natural representation of entrainment (Lenderink et al., 1999). Furthermore they obey automatically the constraint imposed by the TKE budget. For stably stratified conditions, when vertical transport of TKE is small (e.g. Derbyshire, 1999b), TKE-closure is fully consistent with first-order closure as, for example, shown by Duynkerke and De Roode, 2001 (see also Chapter 4).

Second-order closure schemes add even more complexity. This approach is widely used in engineering, where complex geometries may justify this increase of complexity (Derbyshire, 1999b). Mellor and Yamada (1974, 1982) systematically derived a hierarchy of turbulent closure models. They conclude that for many geophysical flows the differences are generally small, since mixing events are

generally dominated by the shear and buoyancy terms in the TKE equation. The main interest of higher-order schemes is to provide realistic simulations of turbulent statistics, which cannot be ignored in pollution dispersion studies (Kastner-Klein et al., 2003), in mesoscale studies over complex terrain (Martín et al., 2001), nor in studies on turbulent transport in the vegetation (Raupach et al., 1996).

It should be noted that the validity of the local closure assumption (i.e. that fluxes are proportional to local gradients) is limited above the surface layer. This is particularly true for convective conditions, where turbulent fluxes can even be directed opposite to the local gradient. For these conditions most atmospheric models apply non-local mixing approximations (Holtlag and Boville, 1993) or mass flux approaches (Siebesma et al., 2007). For stably stratified conditions the local closure assumption is generally acceptable (Derbyshire, 1990; 1999b). However, when looking into more detail, nonlocal transport may play a role in stable conditions as well, for example internal-wave transport of second order moments (Cuxart et al., 2002; Zilitinkevich, 2002).

1.4 The SBL and large-scale models

1.4.1 The role of the ABL on the synoptic scale

In the ABL, drag or friction slows the wind down to subgeostrophic values. As a result, the flow in the ABL obtains a cross-isobaric component from high to low pressure (Figure 1.3a). For flow around high and low pressure areas this causes ABL divergence and convergence, respectively. Continuity of mass requires compensating vertical motions. In high pressure areas, the divergence of ABL air induces descending motions. This subsidence has a drying and warming effect and is responsible for the fair-weather in high pressure systems. Contrary, convergence around low pressure areas, also referred to as cyclone filling, induces rising motions, which are often responsible for cloudy and rainy conditions. The process of inducing vertical motions due to boundary layer friction is called Ekman pumping. For mid-latitude weather systems this Ekman pumping is responsible for the decay of circulation (Holton, 1992).

1.4.2 The SBL in weather and climate models

The previous paragraph illustrates how boundary layer drag impacts on the large-scale synoptic situation. Thus, the parameterization of turbulence is not only important for a correct representation of the vertical wind and temperature profiles, but has also influence on the larger scale (King et al., 2007). For atmospheric models, the latter may be considered as important as the first.

Large-scale models consist of a dynamical core that basically resolves the synoptic patterns and a package of physical parameterizations that takes care of the subgrid processes like turbulence, radiation, convection, precipitation, and the coupling with the land surface (Teixeira et al., 2008). These parameterizations are necessarily simplifications of reality and often involve free parameters. Ideally, these parameters are accurately determined from field experiments or theoretical considerations, but in many cases this is not possible. In practice, model parameters are often tuned to model performance. This tuning process may result in compensating errors, which make it difficult to trace back the source of modeling problems.

Note that numerical weather predication (NWP) models may set different priorities than climate models. For NWP models an accurate prediction of the weather patterns a few days ahead has a higher priority than an accurate representation of all physical processes. For example, the interactions between the atmosphere and the soil water are generally not relevant on these short timescales. On the other hand, climate modelers need to take this type of processes into account in order to prevent their models from drifting away to unrealistic states. As such, NWP can be considered an *initial value problem*, while climate modeling is more of a *boundary condition problem*.

Most large-scale models use first-order turbulence closure for stably stratified conditions. Turbulent transfer rates are corrected for stability by functions which depend on the local Ri_g :

$$K_\psi = l^2 \left| \frac{\partial U}{\partial z} \right| f(Ri_g) . \quad (1.12)$$

This formulation is fully consistent with Eq. (1.7). The stability functions $f(Ri_g)$ can be derived from the flux-profile relations. Slight changes in the stability functions may have significant effect on the representation of the temperature at screen level (Viterbo et al., 1999; King, 2001) especially in polar areas (e.g. Northern Scandinavia, Siberia, Antarctica). Figure 1.5 presents two different forms of the stability functions for momentum and heat. The BH91 functions are based on observations from Cabauw (Beljaars and Holtslag, 1991). The revised Louis-Tiedtke-Geleyn (rLTG) functions (Louis et al, 1982; Viterbo et al., 1999) allow for much more turbulent mixing than can be motivated by field experiments (e.g. Cuxart et al., 2006). Nevertheless, they are widely used in NWP model, while this has obvious detrimental effects on the structure of the SBL: temperature inversions are too weak, the LLJ is situated at a too high level and is partially ‘mixed away’, and the SBL is typically too thick (e.g. Brown et al., 2005; Cheinet et al., 2005; Cuxart et al., 2006).

Why do operational models apply much more mixing for stably stratified conditions than can be motivated from observations? It appears that when realistic

stability functions are used, the cyclone filling in the models is too small, which results in a too small Ekman pumping. This has a negative impact on the synoptic model scores for the medium range forecasts (e.g. Beljaars and Viterbo, 1998). To improve model scores, the lack of Ekman pumping is compensated for by artificially increasing the boundary layer drag by enhancing the mixing for stably stratified conditions. It is also argued that realistic mixing efficiencies tend to decouple the SBL from the surface. This results in unrealistically low surface temperatures, the so-called run-away cooling (Van Lipzig et al., 1998; Derbyshire, 1999a). In a way, the stability functions for stable conditions are used as a tuning parameter to optimize model scores. For example, when the soil freezing was introduced in the ECMWF model the stability functions were changed in order not to loose model performance (Viterbo et al., 1999).

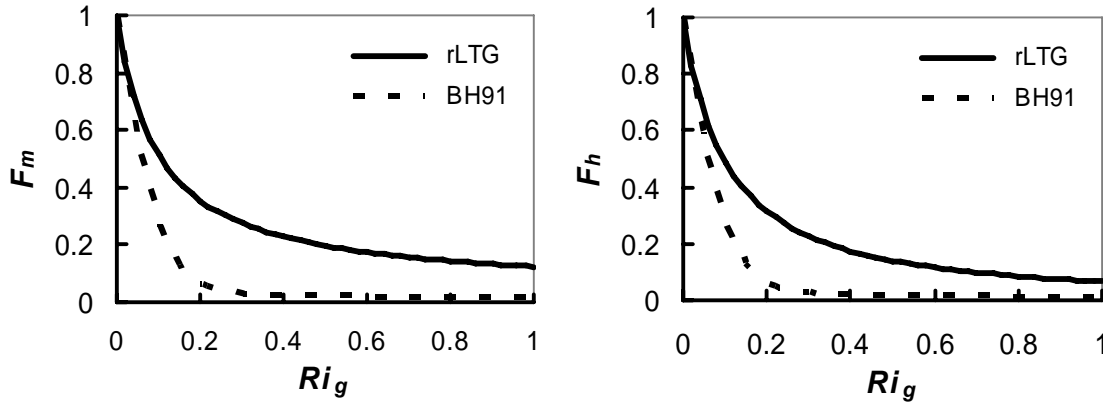


Figure 1.5: Stability functions as proposed by Viterbo et al. (1999) (revised Louis-Tiedtke-Geleyn, rLTG) and by Beljaars and Holtslag (1991).

However, some arguments *can* be made that turbulent transfer rates obtained from local observations are too low. Mahrt (1987) suggested that landscape heterogeneity within a gridbox could result in more mixing on the scale of the gridbox than could be inferred from local measurement sites (see also Ronda and De Bruin, 1999). This aggregation effect was further investigated by McCabe and Brown (2007). They showed that this effect is too small to bridge the gap between observed stability functions and those applied in NWP models. Another possibility is that drag resulting from breaking gravity waves is not correctly represented in NWP models (Chimonas and Nappo, 1989). Small scale topographic variations are neglected in NWPs, but Steeneveld et al. (2008b) showed that gravity wave drag resulting from scales that are generally ignored may contribute significantly to the total stress. In modeling practice, this unresolved gravity wave drag would then be compensated for by the enhancing the turbulent mixing.

Recently, experiments have been performed with NWP models to avoid the enhanced mixing stability functions. Brown et al. (2008) replaced (among others) the enhanced mixing stability functions by more realistic stability functions over sea. The reduced mixing improved the comparison of modeled surface winds over the ocean with wind observations from the QuickSCAT dataset. In the most recent cycles of the ECMWF model excessive mixing *above* the ABL was removed (Bechtold et al., 2008). This measure increased the wind shear in the model both close to the surface and at the level of the jet stream (meant is the polar jet stream at about 7 km height, not to be confused with the nocturnal LLJ), which has a positive effect on the synoptic activity and the representation of stratocumulus decks. These experiments indicate that NWP modelers are well aware of the problems associated with enhanced mixing. At the same time, the caution with which measures are taken demonstrates that the cause and effect relations are still not fully understood.

1.5 Evaluation studies

1.5.1 Observations

High-quality observations are an essential link in the chain of theory development, modeling, and validation. Field campaigns lasting for a couple of weeks mostly focus on particular atmospheric phenomena. For example, the CASES-99 campaign, performed in Kansas, USA, in October 1999, specifically focused on the various processes in the SBL (Poulos, et al. 2002). Observations from this experiment are used in Chapter 4.

Continuous measurement programs are necessary for monitoring long-term trends in the atmosphere. Furthermore, they allow for studying features on a climatological basis. In this thesis we exploit the extensive dataset of the Cabauw measurement site (51.97° N, 4.93° E). Cabauw is situated in the central part of the Netherlands in relatively open terrain. The surroundings consist of meadows, tree lines, and scattered villages. The river Rhine flows 1 km south of the site. Figure 1.6 indicates the location of the various obstacles. The site was founded in 1973, to study the atmosphere and its interactions with the surface (Van Ulden and Wieringa, 1996). The 200 m main tower provides in situ observations of wind, temperature and humidity. Turbulent fluxes are measured at four levels. Besides the tower, numerous radiation, remote sensing, and soil instruments are available.

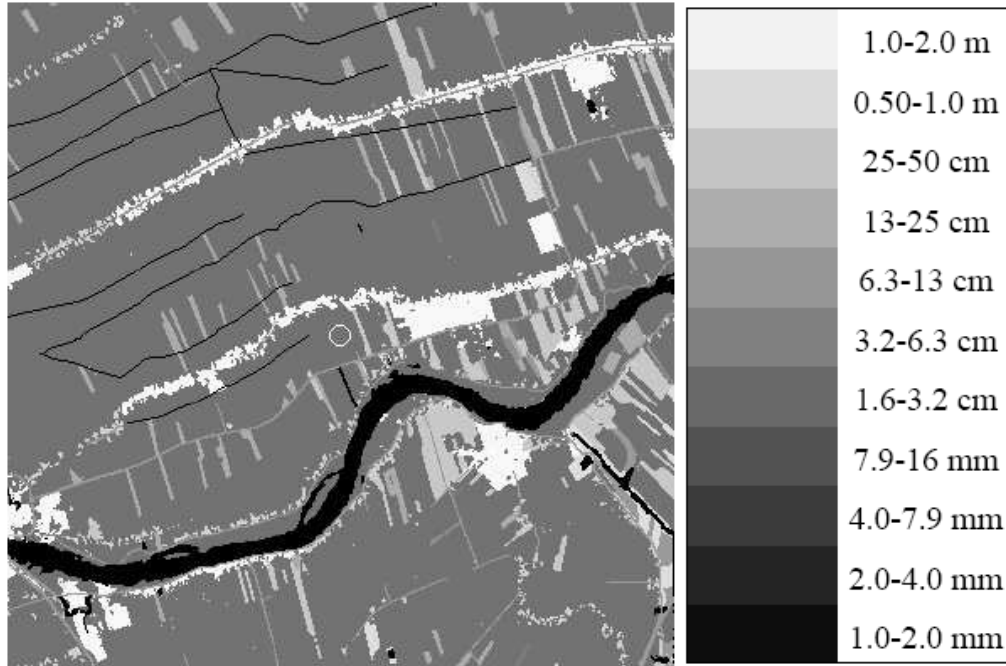


Figure 1.6: Satellite-based map of the roughness length in an area of $(10 \text{ km})^2$ around the Cabauw site, which is indicated by the circle (from: Verkaik and Holtslag, 2007).

1.5.2 The Single-Column-Modeling (SCM) approach

Single-column models (SCMs) have become a widespread and successful tool to evaluate parameterizations (e.g. Lenderink et al., 2004; Cuxart et al., 2006; Steeneveld et al., 2006; Chapter 5). A SCM can be considered as a grid column of a NWP model in which all physical parameterizations are represented. A SCM is driven by large-scale forcings (like the geostrophic wind and advection) that replace the interaction with the neighboring columns. At the top and the bottom, boundary conditions can be specified, for example, the temperature at the surface.

A clear advantage of SCMs is that parameterizations can be tested in isolation from the large-scale circulation, which may facilitate identification of model problems and helps to monitor progress that is made in model development. At the same time, SCM evaluation is one step, always needed is a full 3D evaluation: parameterizations may perform well in SCM mode, but this does not guarantee that they perform equally well in the context of a 3D model. A risk of the SCM approach is that often so-called ‘golden days’ are selected as case-studies. On these days the phenomenon under study is well-developed and disturbances are absent. Consequently, parameterizations may be tuned towards ideal conditions that do not occur frequently in reality. Finally, the prescription of the large-scale forcings is not trivial and may have a considerable influence on the results as will be shown in Chapter 5.

1.5.3 GABLS

The GEWEX Atmospheric Boundary Layer Studies (GABLS) working group was initiated in 2001. Its motivation is to improve the representation of the ABL in NWP models on the basis of a proper understanding of the relevant physical processes. Within GABLS, three SCM intercomparison studies have been performed so far (parallel intercomparison studies with large-eddy simulation (LES) models were performed). All comparison studies focused on the SBL. This thesis uses GABLS cases as a reference in several chapters. In fact, the last chapter was even motivated by problems encountered in designing the third intercomparison case.

Results of the first intercomparison study indicated that operational models apply too high mixing efficiencies which results in a deterioration of the SBL structure. The second case, which is used in Chapter 4, showed large differences between the various SCMs in all parameters with substantial deviations from the observations on which the case was based. The latter was, at least partly, attributed to the high degree of idealization of the forcings.

Recently, a third intercomparison case for SCMs and LES has been set-up, based on observations from the Cabauw measurement site in The Netherlands (Baas et al., 2008b). The focus of this case is on the representation of the decoupling around sunset, the subsequent development of the (LLJ) and the morning transition. Contrary to previous GABLS cases, no surface temperature is prescribed, but the models are run in full coupling with the land-surface scheme. An accurate prescription of the large-scale atmospheric forcings should enable a direct evaluation of the SCM results against observational data (Bosveld et al., 2008). How to design SCM experiments in a proper way is extensively discussed in Chapter 5.

1.6 Goals and set-up of thesis

The previous pages presented an overview of SBL processes, turbulence modeling and the role of the SBL in large-scale atmospheric models. Although much progress has been made in the last decennia, the different processes and their interactions are complex and not fully understood. In many large-scale atmospheric models the SBL is not represented in a satisfactory way. This thesis aims to contribute to the understanding of processes in the SBL and their representation in atmospheric models. To this end, observations from the Cabauw database are analyzed and parameterizations of SBL turbulence are tested in a state-of-the-art SCM.

Specifically, the objectives of this thesis are:

1. To make a climatology and classification of SBL observations suitable to compare with model climatology;
2. To improve the understanding and description of turbulent mixing in stably stratified conditions;
3. To test various mixing assumptions from literature in a SCM in comparison with selected tower and land surface data.

The set-up of this thesis is as follows. Chapter 2 presents a climatology of the SBL in Cabauw, in particular of the nocturnal LLJ. The structure of the SBL is determined by its external forcings, which are the geostrophic wind and the nocturnal cooling. Therefore, different classes of SBLs are distinguished, varying from clear skies and calm to windy and overcast conditions. For each class characteristics of the LLJ are derived like frequency of occurrence, height above the surface, and the wind turning with respect to the 10 m wind.

In modeling the diurnal cycle of the ABL, the representation of turbulent fluxes is crucial. Turbulent processes cannot be resolved directly, but must be parameterized. Chapter 3 critically discusses one of the widely applied tools to model atmospheric turbulence, the flux-profile relations. It will be demonstrated that in testing these relations with field data self-correlation is a serious issue. Flux-gradient relations are applied in so-called first-order closure models. In Chapter 4 an alternative way of turbulence modeling is discussed, the so-called 1.5-order or TKE closure model. It investigates how this TKE-closure scheme relates to the flux-gradient relations discussed in Chapter 3.

Chapter 5 brings the preceding chapters together. It discusses how the representation of LLJs depends on the type of turbulence closure. A state-of-the-art SCM is used to map these dependencies. However, to drive a SCM, it is necessary to prescribe large-scale forcings. The question is whether it is possible to discriminate between different turbulence parameterizations in a comparison with observations given the uncertainties in the forcings. This chapter discusses the question how to compare single-column model results to observations. Finally, Chapter 6 presents a summary of the thesis, and discusses some directions for further research. The thesis ends with a preliminary analysis of the impact of the turbulence formulation in two climate runs.

2 A Climatology of Nocturnal Low-level Jets at Cabauw*

Abstract. *A climatology of nocturnal low-level jets (LLJs) is presented for the topographically flat measurement site at Cabauw, The Netherlands. LLJ characteristics are derived from a seven year half-hourly database of wind speed profiles, obtained from the 200 m mast and a wind profiler. Many LLJs at Cabauw originate from an inertial oscillation, which develops after sunset in a layer decoupled from the surface by stable stratification. The data are classified to different types of stable boundary layers by using the geostrophic wind speed and the isothermal net radiative cooling as classification parameters. For each of these classes LLJ characteristics like frequency of occurrence, height above ground level, and the turning of the wind vector across the boundary layer are determined. It is found that LLJs occur in about 20% of the nights, that they are typically situated at 140 to 260 m above ground level, and have a speed of 6 to 10 m s⁻¹. Development of a substantial LLJ is most likely to occur for moderate geostrophic forcing and a high radiative cooling. A comparison with model reanalysis (ERA40) is added to illustrate how the results can be used to evaluate the performance of atmospheric models.*

2.1 Introduction

Low-level jets (LLJs) are frequently observed phenomena in the nocturnal atmosphere in many parts of the world. They are characterized by a maximum in the wind speed profile, which is typically situated 100 to 500 m above the earth's surface. In literature, many studies can be found on the development and the characteristics of LLJs, e.g. Bonner (1968), Garratt (1985), Kraus et al. (1985), Whiteman et al. (1997), Andreas et al. (2000), Banta et al. (2002), and Song et al. (2005).

Knowledge of the characteristics of the LLJ is relevant for aviation, wind energy applications (Storm et al., 2009), the transport of pollutants (Beyrich, 1994), and other atmospheric constituents like ozone (Banta et al., 1998) and CO₂ (Mathieu et al., 2005; Karipot et al. 2006). Furthermore, the strong shear below the jet can influence the turbulent exchange between the surface and the atmosphere (Banta et al., 2006; Conangla and Cuxart, 2006). Recent wind tunnel experiments showed that LLJ-generated shear may cause intermittent bursts of turbulence in

* This Chapter has been published as: Baas, P., F.C. Bosveld, H. Klein Baltink, and A.A.M. Holtslag, 2009: A climatology of nocturnal low-level jets at Cabauw. *J. Appl. Meteor. Climatol.*, **48**, 1627-1642.

the lower part of the stable boundary layer (SBL) (Ohya et al., 2008). Over the Great Plains in the United States, LLJs are related to large amounts of moisture transport (Cheinet et al., 2005), which plays an important role in the formation of deep convective systems (Maddox, 1983).

Modeling of the SBL is still a challenge (e.g. Holtslag, 2006). In addition to breaking gravity waves, radiative flux divergence and sensitivity to surface heterogeneity, also LLJs complicate an accurate prediction of the SBL (e.g. Mahrt et al., 1998). Stensrud (1996) suggests that the structure of the SBL is closely linked to characteristics of the LLJ. Banta et al. (2003) state that bulk properties of the LLJ must be represented correctly in atmospheric models to obtain realistic vertical turbulent mixing characteristics. At the same time, the parameterization of turbulent diffusion for stable stratification is important for simulating the LLJ.

Currently, general circulation models (GCM's) are not able to reproduce properties of the LLJ in a satisfactory way (Cheinet et al., 2005). This is especially true for LLJs that form below 200 m above the surface (Banta et al., 2002). LLJs at higher levels have been successfully simulated as shown by e.g. Anderson and Arritt (2000) and Castro (2007). For the Great Plains area they find that, compared to long-term observations from the NOAA Wind Profiler Network (lowest level of detection at 500 m above ground level), the representation of LLJs in the NCEP-NCAR reanalysis is generally realistic. Ghan et al. (1996) find similar results for a comparison of two GCM's with Bonner's (1968) climatology. Apart from climatological studies as mentioned above, many studies investigate one or more individual LLJ cases, for example, to learn about its forcings or to test different parameterization schemes (e.g. Parish et al., 1988; Zhong et al., 1996; Zhang et al., 2001; Todd et al., 2008; Storm et al., 2009).

This study presents a climatology of the nocturnal LLJ at Cabauw. Having such a climatology available, an assessment of the quality of atmospheric models and climate runs can be made with respect to the frequency of occurrence and the characteristics of LLJs. When a model simulates the climatology of the nocturnal LLJ in a proper way, it is likely that its representation of the SBL structure is realistic as well. Often model evaluation is based on 'ideal' case studies which does not assess the model performance in operational practice. The availability of long term observations makes the Cabauw site well suitable for deriving climatological information (Van Ulden and Wieringa, 1996). Other studies that provide LLJ climatologies are Kurzeja et al. (1991), Whiteman (1997), and Song et al. (2005).

To get insight in the LLJ characteristics at Cabauw, we analyze seven years of half-hourly tower and wind profiler observations. Given our extended dataset, we are able to refine our statistics by defining classes which characterize different SBL regimes. This gives valuable insights in how LLJ characteristics depend on

different forcing conditions. The development of the LLJ is closely related to the structure of the SBL. For example, according to Blackadar (1957) LLJs often form on top of the nocturnal inversion. Banta et al. (2006) show that the shape of the wind profile depends on stability. The structure of the SBL is determined by a number of factors. In general, the two dominating forcing parameters are radiative cooling and the geostrophic wind speed. The former is mainly determined by the cloudiness and the surface characteristics (soil type and vegetation), while the latter is determined by the horizontal pressure gradient. We classify our data to radiative cooling and geostrophic wind speed. As such, we obtain classes of varying stability, ranging from high wind speed and clouds (deep SBL, weakly stable) to clear sky and calm conditions (shallow SBL, very stable) (c.f. Mahrt et al., 1998). It will be shown that this classification spans a wide range of SBL wind and temperature structures. For each combination of nocturnal cooling and geostrophic wind, LLJ characteristics are presented. Other parameters which play a role in determining the structure of the SBL are the stability of the residual layer, (shallow) baroclinicity, and large-scale advection. In coastal areas differential heating may play a role. The turbulent structure of the preceding daytime convective boundary layer is of influence, as well. The effect of some of these factors on our results will be discussed. To illustrate how our results can be applied for model evaluation, we perform a similar analysis to ERA40 data and then compare to the observed climatology.

Section 2.2 discusses various forcing mechanism of the LLJ. In Section 2.3 the Cabauw site is introduced and we will discuss the observations, while in Section 2.4 we explain how we define a LLJ. Section 2.5 explains the classification to different types of SBLs into more detail. Next, in Section 2.6 the results are presented. In Section 2.7 a comparison is made with LLJ characteristics in the ERA40 reanalysis. Finally, the conclusions are summarized in Section 2.8.

2.2 Mechanisms

LLJs can be formed by a variety of mechanisms (e.g. Stull, 1988; Stensrud, 1996). Blackadar (1957) suggested that the diurnal variation in the eddy viscosity leads to nocturnal LLJ formation. When around sunset stable stratification develops, turbulence dies out and the upper part of the former mixed layer becomes decoupled from the surface. In this layer, where friction does not play a role anymore, the daytime balance of forces is disturbed. As a consequence, the Coriolis force induces an oscillation in the wind vector around the geostrophic wind producing a super-geostrophic LLJ later during the night. In fact, it is the ageostrophic component of the wind vector at the moment of decoupling that rotates around the geostrophic wind. Figure 2.1 presents three hodographs of the

200 m winds for selected LLJ cases at Cabauw, in which a clear inertial oscillation is seen. At Cabauw the inertial period amounts to 15.2 hours. Note that of course not all LLJs show such a nice development. When, for example, the decoupling is not complete (e.g. for cases with weaker stratification, as shown by Wippermann, 1973) or when mesoscale phenomena (e.g. waves) play a role, this idealized picture will be disturbed.

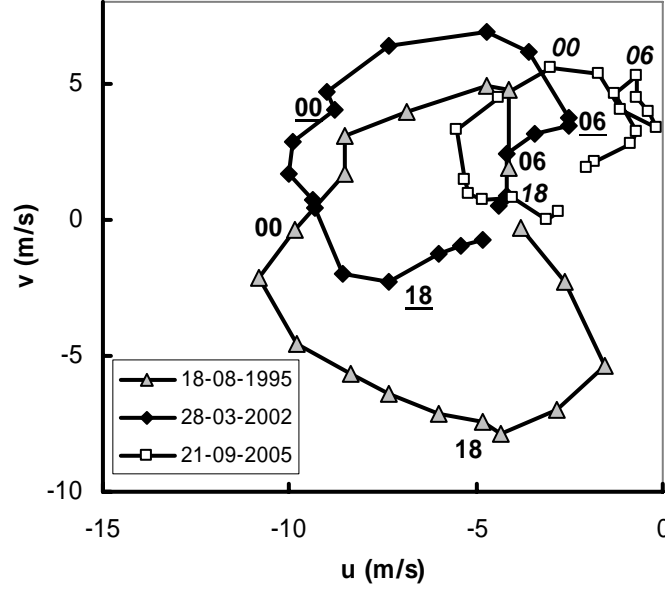


Figure 2.1: Hodographs for three nights in which a typical inertial oscillation LLJ occurred. Hourly observations from Cabauw (200 m). The numbers indicate time in UTC.

Thorpe and Guymer (1977) quantify Blackader's hypothesis by presenting a simple two-layer bulk model. In this model, the upper layer is frictionless and exhibits an inertial oscillation, while the lower layer is coupled to the surface by momentum exchange. By using this model, Andreas et al. (2000) can explain jet properties as observed above the Antarctic Weddell Sea.

Lundquist (2003) questions the evening-transition hypothesis by stating that the predicted inertial oscillations are rarely observed with satisfying agreement. Chimonas (2005) argues that the period of the observed oscillation is shorter than the true inertial period through the influence of the secondary circulation (i.e. the exchange of air between the boundary layer and the free atmosphere). Beside the collapse of turbulent mixing during the evening transition, frictional decoupling of the flow may also occur when relatively warm air flows out over much colder water (Smedman et al., 1993).

Another mechanism for LLJ formation is large-scale baroclinicity, which may occur for instance near extra-tropical cyclones (Kotroni and Lagouvardos,

1993). When the geostrophic wind speed decreases strongly with height, a low-level wind maximum is likely to occur since close to the ground the wind is retarded by frictional forces. In this case, nocturnal LLJs will show a sharper wind maximum than in barotropic conditions (Blackadar, 1957; Wippermann, 1973). In regions where significant changes in surface characteristics occur, for example in coastal areas, differential heating may cause shallow baroclinicity, which may produce strong LLJs. Above slightly sloping terrain a diurnal cycle in the horizontal temperature gradient can occur, which may also cause LLJs to develop (Holton, 1967).

In their study on the Great Plains LLJ in the United States, Whiteman et al. (1997) distinguish between northerly jets related to the passage of cold fronts on the one hand and southerly jets related to an inertial oscillation and the diurnal cycle in horizontal pressure gradient due to sloping terrain on the other hand. This shows that often multiple processes contribute to jet formation (for more examples see Garratt, 1985; Banta et al., 2002).

Since the Cabauw site is on flat terrain, we anticipate that frictional decoupling during the evening transition with a subsequent inertial oscillation and baroclinicity due to synoptic systems are the main LLJ forcing mechanisms. Inevitably, the proximity of the North Sea (50 km to the WNW) plays a role, as well. During the summer months the average horizontal pressure gradient (or geostrophic wind) near the surface shows a clear diurnal cycle: after 10 UTC the dominating geostrophic wind direction starts to veer from WSW to NE directions (see Van Delden, 1993). This corresponds to relatively high pressure above the sea and low pressure above land, which is caused by differential heating. After 19 UTC, which is around sunset, the average geostrophic wind direction becomes WSW again. Therefore, LLJs related to the passage of a sea-breeze front, will weaken after sunset. Since we are mostly interested in LLJs at six hours after sunset we expect that the influence of sea-breeze induced LLJs on our results is relatively small. Nevertheless, it is likely that the diurnal variation in the horizontal pressure gradient influences the ageostrophic wind component in the afternoon and therefore determines how the inertial oscillation develops. We note that no sea-breeze circulation develops when the opposing (i.e. easterly) flow is stronger than 5 m s^{-1} (Tijm et al., 1999).

2.3 Site characteristics and observations

The Cabauw measuring site is situated in the western part of The Netherlands (51.971°N, 4.927°E), in topographically flat terrain. The distance to North Sea is about 50 km in WNW direction. The climate is maritime with rainfall in every season. Southwesterly winds predominate, especially during winter. In the summer

half year the winds are more equally distributed over the compass rose. The majority of geostrophic winds of more than 20 m s^{-1} occur for southwesterly flow in winter. The area around the site consists of meadows, fields and scattered villages. The roughness length varies with wind direction (see Verkaik and Holtslag, 2007). The terrain around the 200 m main tower is free from obstacles up to a few hundred meters in all directions. More details and site characteristics can be found in Van Ulden and Wieringa (1996) and Beljaars and Bosveld (1997).

In this study we use seven years of half-hourly wind observations (1995, 1996, and 2001-2005) from the 200 m mast and a 1290 MHz wind profiler/RASS. (The wind profiler became operational in 1994, and between 1996 and 2001 no regular tower observations are available.) On the mast, wind speed and wind direction are measured at 10, 20, 40, 80, 140 and 200 m with propeller vanes (1995, 1996) and cup anemometers (2001-2005). The accuracy of the propeller vanes and the cup-anemometers is better than 0.5 m s^{-1} . For different heights, both instruments show a similar probability density function of the wind speed. Availability of the mast measurements is close to 100%.

The wind profiler is situated 300 m south of the main tower. For this instrument, wind speed and direction are retrieved with a vertical sampling interval of 60 m. The retrieved values consist of range-weighted averages over layers of approximately 100 m. For this study we use data from 200 m up to 1420 m. Specifications of the profiler can be found in Klein Baltink (1998). Unfortunately, the radar reflections from the rotating cup anemometers in the mast contaminated the signal of the wind profiler in the range of 300 – 430 m above ground level for extended periods of time from 2001 onwards. By applying a more advanced post-processing technique, the so-called Multiple Peak Processing algorithm (see e.g. Gaffard et al., 2006) we strongly reduced this problem. For the wind profiler, data availability depends, amongst others, on the atmospheric conditions. For weakly stable conditions the availability decreases steadily with height from about 80% at 200 m to about 50 % at 1400 m. With increasing stability, the availability decreases to 30 % at 1400 m for very stable conditions. The availability 200 m does not depend on stability. (Here ‘weakly stable’ and ‘very stable’ refer to the two extreme classes in our classification described in Section 2.5 with the highest/lowest geostrophic forcing and lowest/highest nocturnal cooling, respectively.) Missing values were filled in by linear interpolation, but only if not more than two consecutive observations were lacking.

Extra attention has to be paid to the transition between the mast and the wind profiler. An intercomparison of two years of wind observations at 140 and 200 m above ground level showed good agreement between the two systems (Klein Baltink, 1998). However, the detection of LLJs is based on gradients in the

wind profile and is therefore sensitive to small differences between the mast and the wind profiler. For this reason, we discarded profiles for which at 200 m this discrepancy is more than 2 m s^{-1} . If the difference is less than 2 m s^{-1} , the complete profile of the wind profiler is shifted to the mast 200 m winds to eliminate the remaining difference. In this way the shape of the profiles of both the tower and the wind-profiler remain intact. These procedures guarantee a smooth transition between the mast and the profiler data.

Besides the wind observations described above, auxiliary data from other instruments are used. Geostrophic winds are derived from a planar fit of pressure observations from eight synoptic weather stations in a radius of 75 km around Cabauw. Profiles of virtual temperature, T_v , which are used to estimate the inversion height, are derived from the wind profiler/RASS system. Below 200 m, this quantity is derived from observations of air temperature, T_a , and relative humidity, RH , measured by Pt500-elements and Vaisala HMP243 heated relative humidity sensors, respectively (at similar levels as the wind observations). T_v is calculated by

$$T_v = T_a(1 + 0.61r), \quad (2.1)$$

where r is the mixing ratio. Note that the RASS-system detects the acoustic virtual temperature, which differs slightly from the buoyancy virtual temperature, as defined by Eq. 2.1 (Kaimal and Gaynor, 1991). For our purpose this difference can be neglected. The incoming longwave radiation, L^\downarrow , used to calculate the isothermal net radiation (see Section 2.5), is measured with an Eppley pyrgeometer. If data from this instrument is missing, data from a Schulze radiometer is used instead (only nocturnal observations are utilized).

2.4 Criteria for LLJ detection

In the literature many different criteria for LLJs are applied. Following Stull (1988), Andreas et al. (2000) define a LLJ as a maximum in the vertical profile of the wind speed that is at least 2 m s^{-1} faster than wind speeds above and below it within the lowest 1500 m of the atmosphere. Banta et al. (2002) apply a comparable criterion, but with a threshold value of (in specific cases) only 0.5 m s^{-1} . Instead of a fixed threshold value, a relative value can be used by, for example, requiring a falloff of 20% compared to the wind-maximum. Bonner (1968) introduces classes of different types of LLJs by defining threshold values for both the speed of the LLJ and the required falloff above the jet. This classification was adopted by Whiteman (1997).

In this study we define a LLJ as the lowest maximum of the wind speed profile in the lowest 500 m of the atmosphere that is at least both 2 m s^{-1} and 25% faster (equivalent to a 20% falloff) than the next minimum above (Figure 2.2a).

The absolute criterion prevents that in very calm conditions small variations in the wind profile (in the order of measuring errors) are classified as a low-level jet. The relative criterion does the same in cases of high wind speed, where the 2 m s^{-1} criterion may be accidentally satisfied. A minimum is neglected if the wind speed above that minimum increases less than 1 m s^{-1} before decreasing again to values lower than the wind speed of that minimum. Instead, a minimum higher-up is chosen (Figure 2.2b). When no minimum is present (so the wind speed decreases constantly above the maximum) the lowest value of the wind speed profile above the jet is taken as a minimum (Figure 2.2c).

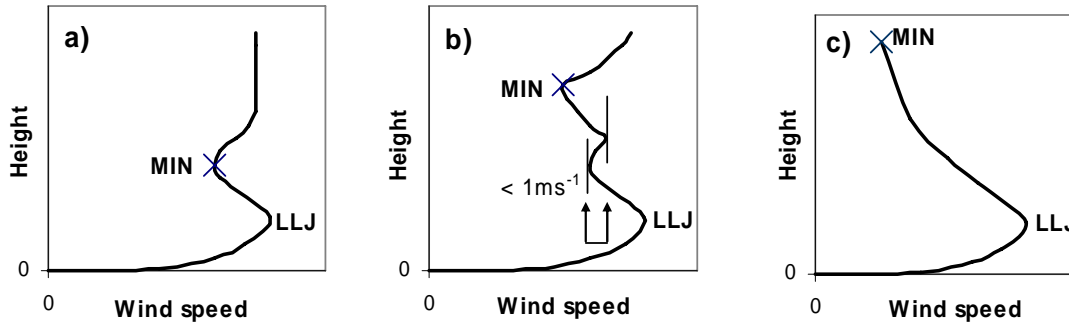


Figure 2.2: Illustration on the detection of LLJs. A LLJ is defined as a maximum in the wind speed profile that is 2 m s^{-1} and 25% faster than the next minimum above (a). A minimum is neglected if the wind speed above increases less than 1 m s^{-1} before decreasing again below the minimum (b). If no minimum is present the lowest wind speed in the profile is taken as a minimum (c).

A wind profile is only classified as a LLJ if the two neighboring half-hour records satisfy the criteria for a LLJ as well. This is done to guarantee that the detected jets show some persistence in time. We acknowledge that these criteria – as any others – are subjective. To assess the influence of the required falloff, for some cases we compare our results with definitions applied in other studies.

For each night, we analyze the wind profile at six hours after sunset (see Section 2.5). To be not too dependent on the availability and quality of this particular profile, the (half-hourly) wind speed profiles from five to seven hours after sunset are analyzed. When multiple profiles contain a LLJ, the one closest to six hours after sunset is included in the statistics. If no LLJ is detected, the night is classified as a non-LLJ night.

Because, in principle, LLJs caused by large scale baroclinicity are not related to the boundary layer structure, we experimented with criteria to exclude cases for which the geostrophic wind decreased substantially with height. The geostrophic wind speed at the surface was estimated from surface pressure

observations from a network of synoptic stations around Cabauw. At 1500 m we used the ordinary wind from the ERA40 database (operational ECMWF output was used after August 2002 when ERA40 ended) as a proxy for the geostrophic wind, since the latter is not available in the ERA40/ECMWF output. If this estimate is more than 5 m s^{-1} lower than the geostrophic wind at the surface, the wind profile is considered baroclinic and occurring jets are not included in the statistics.

To test whether the assumption that the ordinary wind can be used instead of the geostrophic wind is realistic, we made use of a two-year run (2002 and 2003) of the Regional Atmospheric Climate Model (RACMO) in operation at the Royal Netherlands Meteorological Institute (KNMI). For this run the geostrophic winds were archived. Every day the model is run from the ECMWF analysis. Comparison of the ordinary and geostrophic winds within RACMO at about 1500 m showed a bias of only 0.1 m s^{-1} and a standard deviation of 1.6 m s^{-1} . These small deviations justify our assumption to use the ordinary wind as a proxy for the geostrophic wind.

2.5 Classifying SBL observations

Section 2.6.2 presents a classification of LLJ characteristics for different types of SBLs. The classification, which was also applied by Bosveld and Beyrich (2004), is based on two external forcing parameters, which in general determine the development of the SBL. These are the surface geostrophic wind speed and the nocturnal radiative cooling. (Note that Bosveld and Beyrich (2004) used the 200 m wind as a proxy for the geostrophic wind.) The advantage of using external parameters is that these do not depend on the development of the SBL itself (Van de Wiel et al., 2002). For example, as a measure of the cooling the net radiation at the surface could be used. However, this quantity is influenced by local thermal characteristics of the surface and depends on the structure of the SBL. Instead, we prefer to use the so-called isothermal net radiation at the top of the SBL (Monteith, 1981; Holtslag and De Bruin, 1988). Since the temperature at the top of the SBL is not readily available, we use the temperature at 200 m height as a proxy. Thus, we define the isothermal net radiation, Q^*_i , as

$$Q^*_i = L^\downarrow - \varepsilon_s \sigma (Ta_{200})^4, \quad (2.2)$$

where L^\downarrow is the incoming longwave radiation (surface observations were used), Ta_{200} is the air temperature at 200 m, σ is the Stefan-Boltzmann constant, and ε_s is the emissivity of the surface. For grass a good approximation of ε_s is 1 (Holtslag and De Bruin, 1988), a value which is adopted in this study.

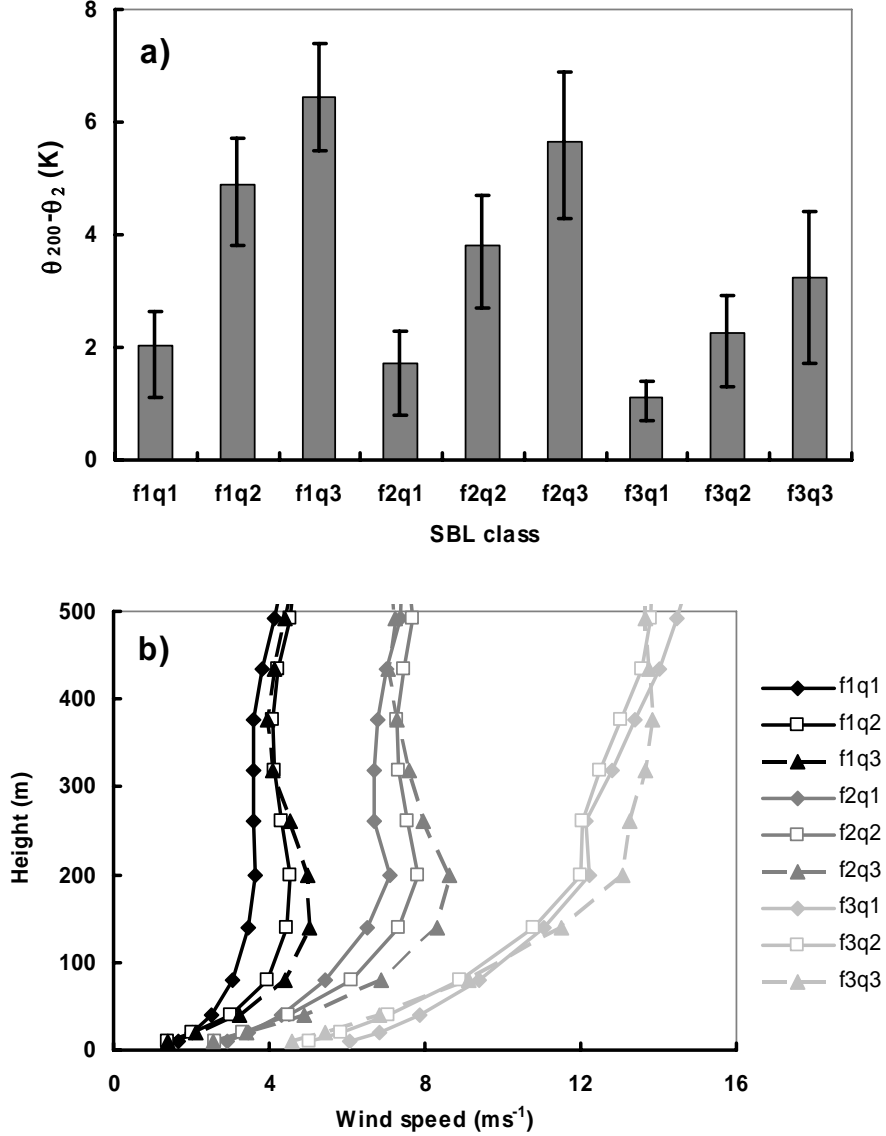


Figure 2.3: Average inversion strength, expressed as the potential temperature difference between 200 and 2 m, $\theta_{200} - \theta_2$, for different classes of SBLs (a). Error bars indicate the 25th and the 75th percentile. Panel (b) presents average wind profiles for the nine SBL classes. Only data six hours after sunset are used. The labels f1, f2 and f3 correspond to $|\mathbf{V}_g| \leq 5 \text{ m s}^{-1}$, $5 < |\mathbf{V}_g| \leq 10 \text{ m s}^{-1}$ and $|\mathbf{V}_g| > 10 \text{ m s}^{-1}$. The labels q1, q2 and q3 correspond to $\Delta T_{iso} \leq 3 \text{ K}$, $3 < \Delta T_{iso} \leq 6 \text{ K}$ and $\Delta T_{iso} > 6 \text{ K}$.

We focus on the SBL development in the first six hours after sunset. Although the inertial oscillation period amounts to 15.2 h, nocturnal LLJs should reach their maximum speed around 6 h after sunset. Firstly, the wind vector at the moment of decoupling is already veered compared to the geostrophic wind. Secondly, the transition to stable stratification occurs often well before sunset. We

define three classes for the average geostrophic wind speed, $|\mathbf{V}_g|$, over the first six hours of the night: $|\mathbf{V}_g| \leq 5 \text{ m s}^{-1}$, $5 < |\mathbf{V}_g| \leq 10 \text{ m s}^{-1}$ and $|\mathbf{V}_g| > 10 \text{ m s}^{-1}$. For the isothermal long wave radiative cooling three classes are defined, as well: $\Delta T_{iso} \leq 3 \text{ K}$, $3 < \Delta T_{iso} \leq 6 \text{ K}$ and $\Delta T_{iso} > 6 \text{ K}$. Here ΔT_{iso} is the temperature drop that the net isothermal long wave cooling, integrated over the first six hours after sunset, would cause in a 200 m high column of air:

$$\Delta T_{iso} = -\frac{1}{200} \sum_{t=0}^{6h} \frac{Q^*_i(t)}{\rho c_p}, \quad (2.3)$$

where ρ is the density of air (taken as 1.2 kg m^{-3}), and c_p is the heat capacity of air at constant pressure. Note that each 1 K temperature drop corresponds to a radiative cooling of 12 W m^{-2} .

Combining the classes of geostrophic wind speed and isothermal cooling yields nine classes in total. Each of them represents a different SBL structure. This is illustrated in Figure 2.3. Figure 2.3a shows the average inversion strength, expressed as the potential temperature difference between 200 and 2 m, $\theta_{200} - \theta_2$, for each class. The average values vary from about 1 to 6 K and the variation within each class (indicated by the 25th and the 75th percentiles) is small. The average wind profiles are given in Figure 2.3b. When $|\mathbf{V}_g| < 10 \text{ m s}^{-1}$, the wind speed increases for increasing nocturnal cooling. Except for the class with strongest $|\mathbf{V}_g|$, even the average wind speed profiles show a low-level maximum. Figure 2.3 demonstrates that our classification covers a wide range of SBLs in both wind and temperature structures.

Table 2.1: Distribution of nights over SBL classes using $|\mathbf{V}_g|$ (m s^{-1}) and ΔT_{iso} (K) as classification parameters. The upper numbers indicate the total number of nights for each class. The lower numbers, in italics, indicate the percentage of occurrence for each class in winter (October – March) and summer (April – September). For example, 154 nights are classified in the class with high geostrophic forcing and intermediate nocturnal cooling. In winter 16% of the nights fall in this class, in summer 8%.

	$ \mathbf{V}_g \leq 5$	$5 < \mathbf{V}_g \leq 10$	$ \mathbf{V}_g > 10$	Total
$\Delta T_{iso} \leq 3$	70	191	232	493
	6 5	15 14	26 11	
$3 < \Delta T_{iso} \leq 6$	121	180	154	455
	2 14	11 15	16 8	
$\Delta T_{iso} > 6$	109	174	106	389
	3 12	10 15	11 6	
Total	300	545	492	1337

Of the total of 2553 nights considered, 2270 could successfully be classified into one of the defined classes. After we rejected all profiles for which the difference in wind speed at 200 m between the mast and the wind profiler exceeded 2 m s^{-1} and for which more than two consecutive observations in the lowest 500 m were missing, 1337 nights remained. The number of nights in each class combination is listed in Table 2.1, together with the frequency of occurrence of each class in both summer and winter.

2.6 Climatology of LLJs

In Section 2.6.1 some general characteristics of LLJs at Cabauw are discussed. Except for the analysis of the diurnal cycle, for each night only the profile around six hours after sunset is analyzed as explained in Section 2.4. Section 2.6.1 presents the results for the classification to different SBL types. A comparison with model output is made in Section 2.7.

2.6.1 General characteristics

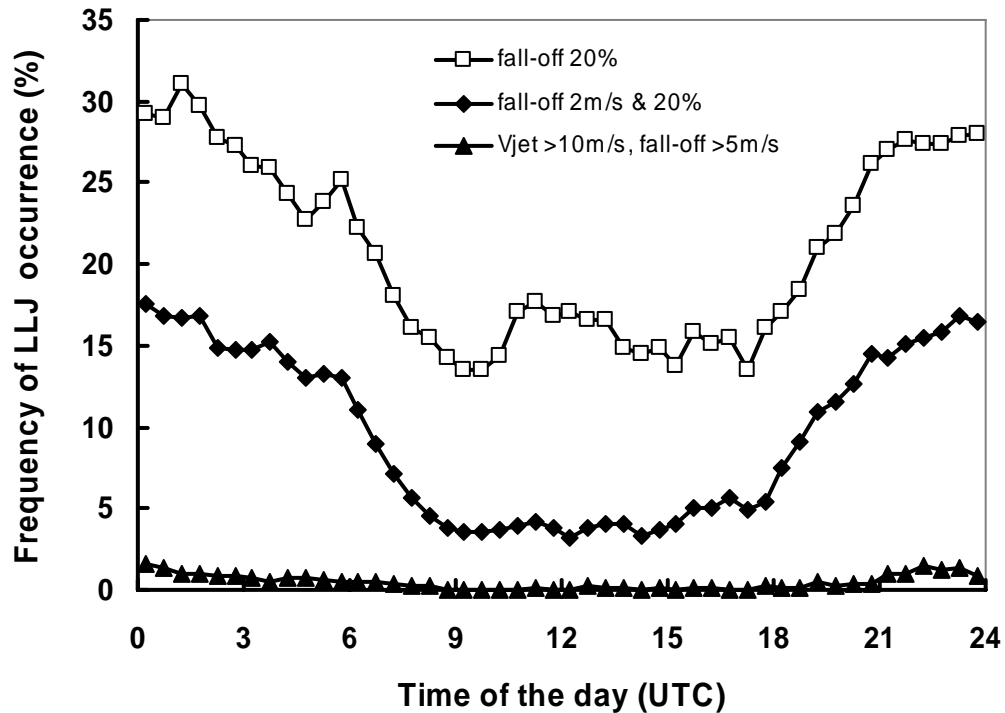


Figure 2.4: Diurnal variation of LLJ occurrence for different definitions of the LLJ.

Van Ulden and Wieringa (1996) mention that at Cabauw nocturnal LLJs are a frequently occurring phenomenon. This is confirmed by Figure 2.4, which shows a clear diurnal cycle in LLJ occurrence. At night, the wind speed profile satisfies our criteria (the thick solid line with diamonds) for a LLJ in almost 20% of the nights. During daytime the frequency of occurrence is much lower, in the order of 3 – 4%.

For comparison the results for some other definitions are added. It appears that the results depend considerably on the choice of the definition. When only a 20% falloff is required, much more LLJs are detected. However, most of the extra jets are very weak, so that it is questionable whether they can be considered as LLJs. Moreover, the difference between the speed of the jet and the minimum above becomes about 1 m s^{-1} , which is in the order of the accuracy of the instruments (i.e. the wind profiler). For wind energy applications, aviation or SBL dynamics, these minor ‘jets’ are probably not important. Figure 2.4 also shows the occurrence of LLJs of more than 10 m s^{-1} , with a decrease of at least 5 m s^{-1} aloft. This criterion was used by Bonner (1968) and more recently by Whiteman (1997) and Song et al. (2005) for the Great Plains Jet. Apparently, this type of jet is much rarer at Cabauw. For example, compare Figure 2.4 with Whiteman’s (1997) Figure 3.

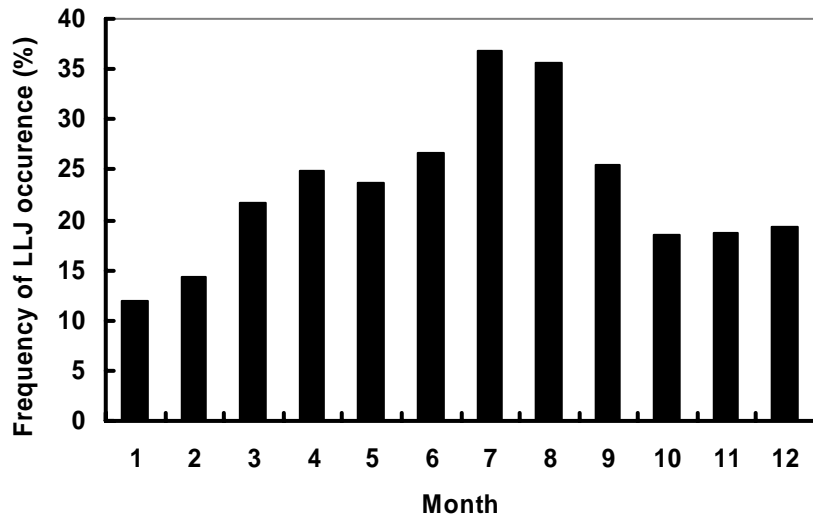


Figure 2.5: Frequency of occurrence of LLJ nights per month.

Many studies highlight the role of the large-scale sloping terrain, which would enhance the Great Plains LLJ (e.g. Holton, 1967; McNider and Pielke, 1981). This could be used as an argument to explain differences between the LLJs of the Great Plains and of Cabauw, as was suggested by Van Ulden and Wieringa (1996). However, other studies show that the effect of the sloping terrain is of much less importance than the inertial oscillation (Parish et al., 1988), while the

study of Jiang et al. (2007) concludes that both mechanisms are of equal importance.

Apart from possible effects of sloping terrain on the Great Plains LLJ strength, we suggest that the discrepancy between LLJs at Cabauw and the Great Plains can also be explained by differences in the turbulent structure of the daytime convective boundary layer (CBL). In the Great Plains turbulence is probably much more vigorous, for example, because the Bowen-ratio is much higher than the 0.25, which is typically observed in Cabauw. More intensive turbulence results in larger ageostrophic wind components. As a result, stronger LLJs will occur. This agrees with the findings of Zhong et al. (1996), who conclude that drier soils enhance the amplitude of the diurnal oscillation in the wind. Note that also differences in study objectives and therefore in the definition of the LLJ, as well as the use of different instrumentation can cause differences in LLJ statistics (Banta et al., 2002).

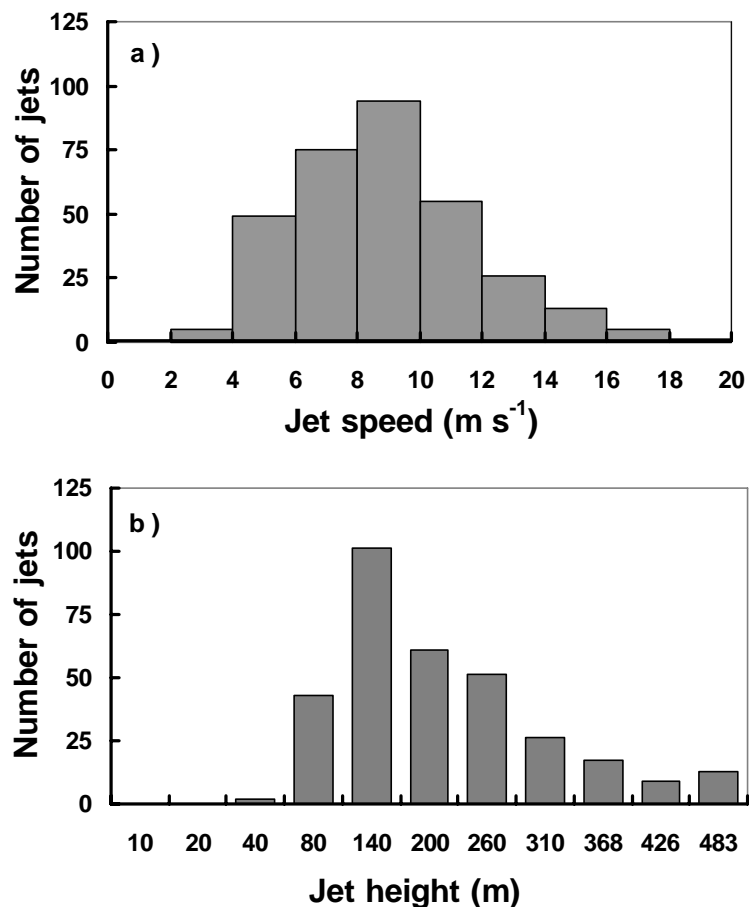


Figure 2.6: Frequency distribution of LLJ speed (a) and LLJ height (b). The Figure is based on LLJs six hours after sunset.

Figure 2.5 presents the seasonal cycle of LLJs. Clearly, LLJs occur most often in the summer months. This can be explained by two reasons. Firstly, in summer the daytime boundary layer is much more convective than in winter. More vigorous turbulence is associated with larger ageostrophic wind components. As a result, nocturnal inertial oscillations will show larger amplitude than in winter. Thus, in summer it is the stronger coupling between the boundary layer and the Earth's surface that stimulates the formation of nocturnal LLJs (e.g. Wilczak et al., 1997). Secondly, in winter the frequency of cloudy nights with strong geostrophic forcing is much higher than in summer (see table 2.1). In Section 2.6.2 it will be shown that for these conditions LLJ occurrence is low.

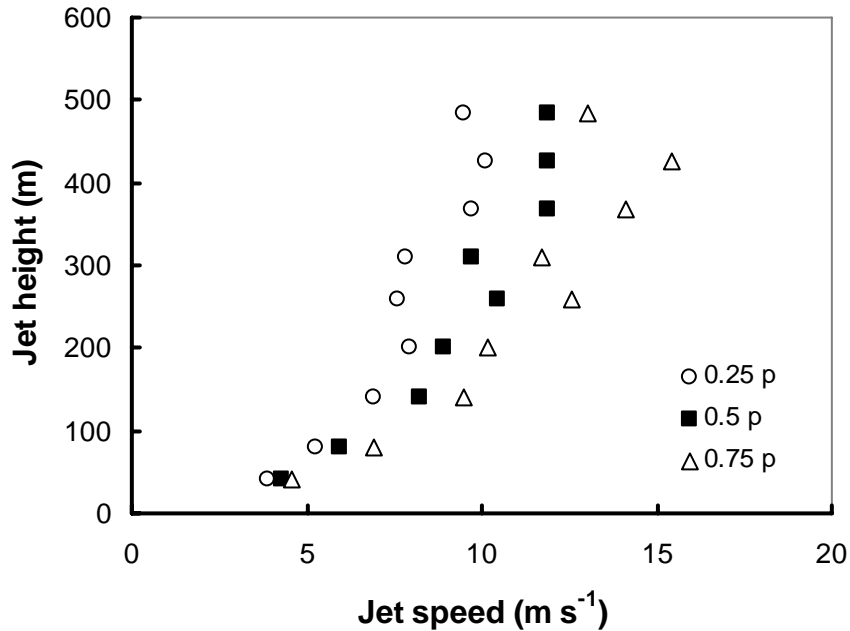


Figure 2.7: Relation between LLJ height and LLJ speed. The black squares indicate the medians. As a measure for the spread, the 25th and the 75th percentiles are given. The Figure is based on LLJs six hours after sunset.

The distribution of LLJ speeds is given in Figure 2.6a, while Figure 2.6b presents the distribution of LLJ heights (based on one observation per night, six hours after sunset). It appears that at Cabauw LLJs typically have a moderate speed of $6 - 10 \text{ m s}^{-1}$ and are located 140 to 260 m above the surface. These numbers compare well to values presented by Banta et al. (2002) and Andreas et al. (2000), for the Cooperative Atmospheric-Surface Exchange Study 1999 (CASES99) and the Ice Station Weddell (Antarctica) dataset, respectively. The same is true for the Stable Atmospheric Boundary-Layer Experiment in Spain (SABLES) (Conangla and Cuxart, 2006). Plotting the LLJ height versus the speed of the LLJ (Figure 2.7), shows a tendency for stronger LLJs to occur at higher

levels. Banta et al. (2002) found similar results for the CASES99 dataset (their Figure 6).

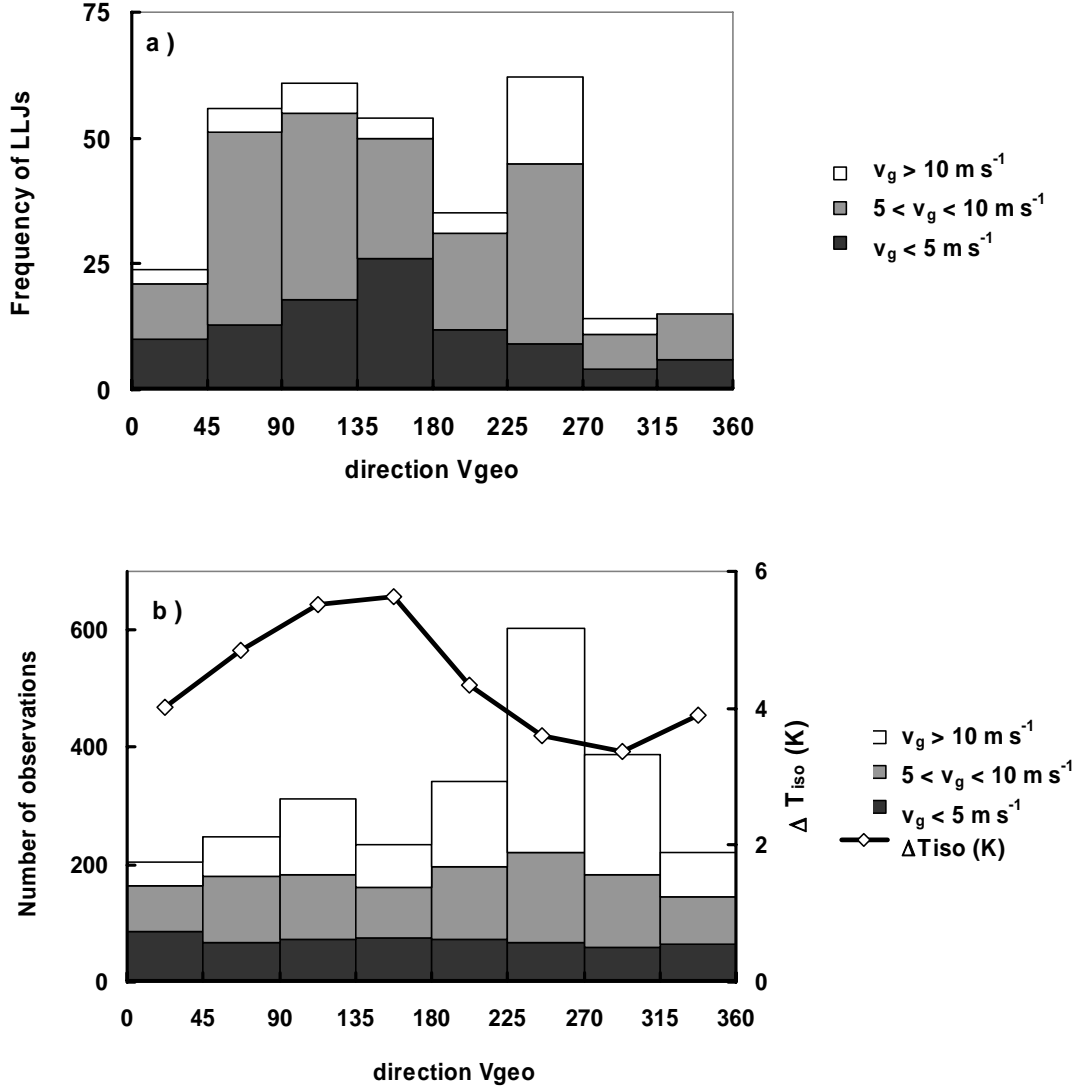


Figure 2.8: Distribution of LLJ occurrence for classes of the geostrophic wind direction (a). The climatological distribution of the geostrophic wind direction is given in (b). The solid line in (b) indicates the average value of the isothermal net radiative cooling for each class of geostrophic wind direction.

To investigate whether any preferred directions of the large-scale flow exist for LLJ formation, figure 2.8a shows how the nocturnal jets at Cabauw are distributed over classes of geostrophic wind direction (45° increments). The different areas represent different classes of geostrophic wind speed. The distribution shows a broad peak for easterly directions (45 – 180°). Another peak in the LLJ occurrence occurs for WSW directions (225 – 270°) of the large-scale flow. Figure 2.8b explains this distribution. It shows the climatological

distribution of the direction of V_g . The average value of ΔT_{iso} for each class of geostrophic wind direction is also presented. Probably, the peak in LLJ occurrence for WSW directions is associated with the dominance of this direction in the total wind distribution. The peak in LLJ occurrence for easterly directions, as observed in Figure 2.8a, can be related to a maximum in the radiative cooling, which is given in Figure 2.8b. The low number of LLJs for northerly directions is likely to be related to the relatively low cooling values. The minimum in the ΔT_{iso} is associated with the presence of the North Sea. For westerly winds (from the coast), on average cloud cover is higher, which leads to lower nocturnal cooling rates than for easterly, more continental air masses. LLJs associated with strong geostrophic forcing are most frequent for WSW direction. The division into classes of V_g shows that for strong geostrophic forcing LLJ occurrence is less likely than for low or moderate geostrophic forcing.

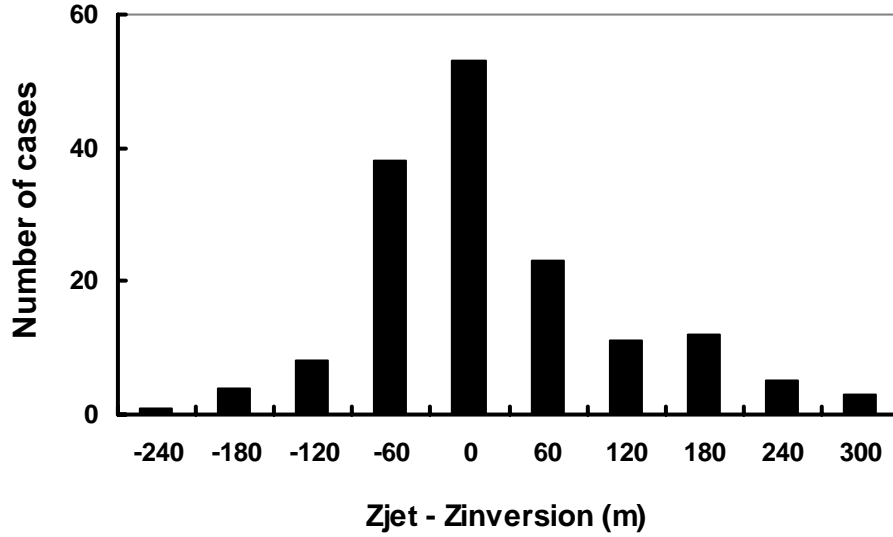


Figure 2.9: Difference in height between the LLJ and the top of the virtual temperature inversion.

We also investigated the relation between the height of the LLJ and the height of the nocturnal temperature inversion. The inversion top is defined as the height of the lowest (virtual) temperature maximum above the surface. Figure 2.9 shows that in most cases the LLJ is situated close to the top of the inversion layer, which is consistent with the inertial oscillation hypothesis of Blackadar (1957). For southerly LLJs in the Great Plains region, Bonner (1968) and Whiteman et al. (1997) find that the jet heights are generally above the tops of the nocturnal inversions (with large variability from case to case). Andreas et al. (2000) find that most LLJs above the Antarctic Weddell Sea, most likely caused by inertial oscillations, are embedded in the inversion layer.

2.6.2 Classification to SBL types

Figure 2.10 gives LLJ characteristics for the nine classes of SBLs defined in Section 2.5. The labels f1, f2, and f3 in Figure 2.9 indicate increasing V_g , while q1, q2 and q3 indicate increasing long wave cooling. The frequency of occurrence of LLJs is shown in Figure 2.10a. Apparently, strong nocturnal cooling facilitates LLJ formation. This is the case for all three classes of geostrophic wind. For strong geostrophic forcing, the occurrence of LLJs is strongly decreased compared to moderate and weak geostrophic forcing. These results suggest that frictional decoupling after sunset is an important forcing mechanism of the Cabauw LLJ. At low cooling rates (for instance caused by the presence of clouds), the stable stratification is weak (see e.g. Figure 2.3a). It is likely to assume that in this case decoupling of the SBL will not occur or only to some degree. As a result, acceleration of the flow through inertial forces is strongly reduced or inhibited and no LLJ will be formed. Comparably, for high geostrophic forcing turbulent mixing maintains the coupling between the surface and the layers aloft, explaining the low frequency of nocturnal LLJ occurrence in these classes. Contrary to what is observed, one would expect the highest frequency of occurrence for the lowest wind class, because then the stable stratification is maximized (see Figure 2.3a). However, for these calm conditions the wind maxima are often so weak that they do not pass the 2 m s^{-1} falloff criterion. We suppose that in this case the ageostrophic wind component is too small to produce a significant inertial oscillation (see also Rama Krishna et al., 2003). If we would apply only the 20% falloff criterion, the lowest wind class *would* show the highest frequency of occurrence.

In Figure 2.10b the average height of the LLJs is shown for each class. For decreasing geostrophic forcing the LLJs are located at a lower altitude. This was also found by Rama Krishna et al. (2003). The LLJ height increases with decreasing radiative cooling. The height varies from about 130 m for the most stable class, to about 300 m for the class with the weakest stability. This tendency agrees with the theoretical concept that the jets form at the top of the SBL, which is shallower for strong nocturnal cooling rates and low geostrophic forcing.

The turning of the wind vector between the jetnose and the wind measured at 10 m above ground level (Figure 2.10c) increases with increasing cooling, except for the highest wind class. However, the dependency on the geostrophic forcing seems to be small. On average, the turning angle between the jet nose and the surface is close to 35° , a value which was earlier reported for clear sky nocturnal boundary layers at Cabauw by Van Ulden and Holtslag (1985). Assuming that the LLJ height is closely related to the nocturnal boundary layer height, Figure 2.10b and 2.10c also support the conclusion of Svensson and Holtslag (2009), that deeper (shallower) boundary layers exhibit smaller (larger)

turning of the wind vector with height: going from q1 to q3 the LLJ is situated at lower altitudes (Figure 2.10b), while (except for the highest wind class) the turning increases (Figure 2.10c).

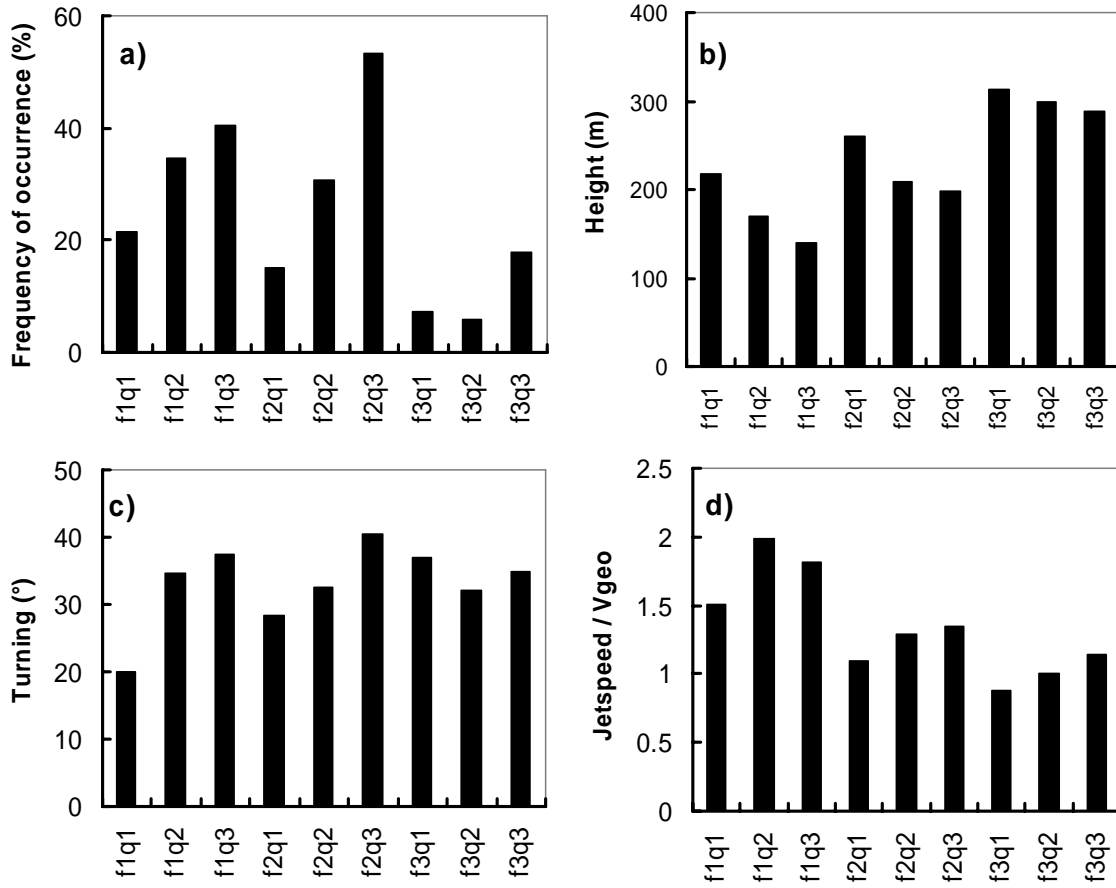


Figure 2.10: LLJ characteristics for 9 classes of SBLs. a) Frequency of LLJ occurrence, b) Jet height, c) Turning of the jet compared to the 10 m wind and d) jet speed relative to the geostrophic wind. The labels f1, f2 and f3 correspond to $|\mathbf{V}_g| \leq 5 \text{ ms}^{-1}$, $5 < |\mathbf{V}_g| \leq 10 \text{ ms}^{-1}$ and $|\mathbf{V}_g| > 10 \text{ ms}^{-1}$. The labels q1, q2 and q3 correspond to $\Delta T_{iso} \leq 3 \text{ K}$, $3 < \Delta T_{iso} \leq 6 \text{ K}$ and $\Delta T_{iso} > 6 \text{ K}$.

Concerning the speed of the LLJs, Figure 2.10d shows that supergeostrophic jets are most common for $|\mathbf{V}_g| \leq 5 \text{ m s}^{-1}$. Except for lowest geostrophic wind class, there is a small tendency that for higher values of the nocturnal cooling the speed of the LLJs increases. It should be noted that contrary to Figure 2.10a, for Figure 2.10b, c, and d the results are not sensitive to the choice of the LLJ definition (not shown).

So far the results can be well interpreted within the context of Blackadar's inertial oscillation theory of LLJ formation. This suggests that frictional decoupling around sunset is the main mechanism for LLJ formation at Cabauw.

However, one might ask whether or not a more detailed selection can be made, which focuses on some conceptual characteristics of the inertial oscillation (see e.g. Beyrich, 1994). As such, we applied additional selection criteria by only selecting LLJs for which the jetspeed is supergeostrophic and for which the wind vector veers from five to seven hours after sunset. Thus, we select only jets which show clear features of an inertial oscillation. About 60% of all LLJ satisfy these criteria. However, the characteristics of these jets (in terms of height and turning compared to the 10 m wind) do not differ from those of the remaining 40% of the LLJs. This suggests that also in the formation of the latter frictional decoupling after sunset plays a role. In summer the fraction of LLJs with clear inertial oscillation characteristics is twice as large as in winter.

2.7 Comparison with ERA40 climatology

Above we presented climatological characteristics of the LLJ with the objective to facilitate the evaluation of atmospheric models. As a proof of principle, we now show how a comparison between our results and an atmospheric model can be performed. We use hourly output from the ERA40 reanalysis of the ECMWF model (Uppala et al., 2005), in particular from the grid point closest to Cabauw. This is the first complete land grid point, next to the North Sea. The resolution is T157 with 60 vertical levels. The lowest model levels are at 10, 30, 70, 120, 190 m. The surface characteristics in the model are representative for the central parts of The Netherlands. Bosveld and Beyrich (2004) show that the model is able to capture the basic structures of the SBL at Cabauw. However, they conclude that the vertical gradients of wind and temperature in the model are too weak and that the turning of the wind vector across the SBL is strongly underestimated.

Although in principal we could take any other representative period, for consistency we decided to analyze the same period as covered by the observations, i.e. the years 1995, 1996 and 2001-2005. Since the ERA40 archive runs only to August 2002, we added operational ECMWF output for the remaining of the period. Some model changes occurred during this period, but no significant adjustments took place in the formulation of the stable boundary layer. Analysis of the period 1986-1995 (only ERA40 data) gave similar results.

Because there are no quality issues involved and model output is much smoother than observations, only the profile at 6 hours after sunset is analyzed. Like the observations, the model wind profiles were classified following the procedure described in Section 2.5. Ideally, the classification parameters V_g and ΔT_{iso} were both taken from model output. Since V_g is not readily available in ERA40 we took the value derived from the pressure observation from the synoptic

stations. Following Eq. 2.2, ΔT_{iso} was calculated using L^\downarrow and T_a from the model level closest to 200 m.

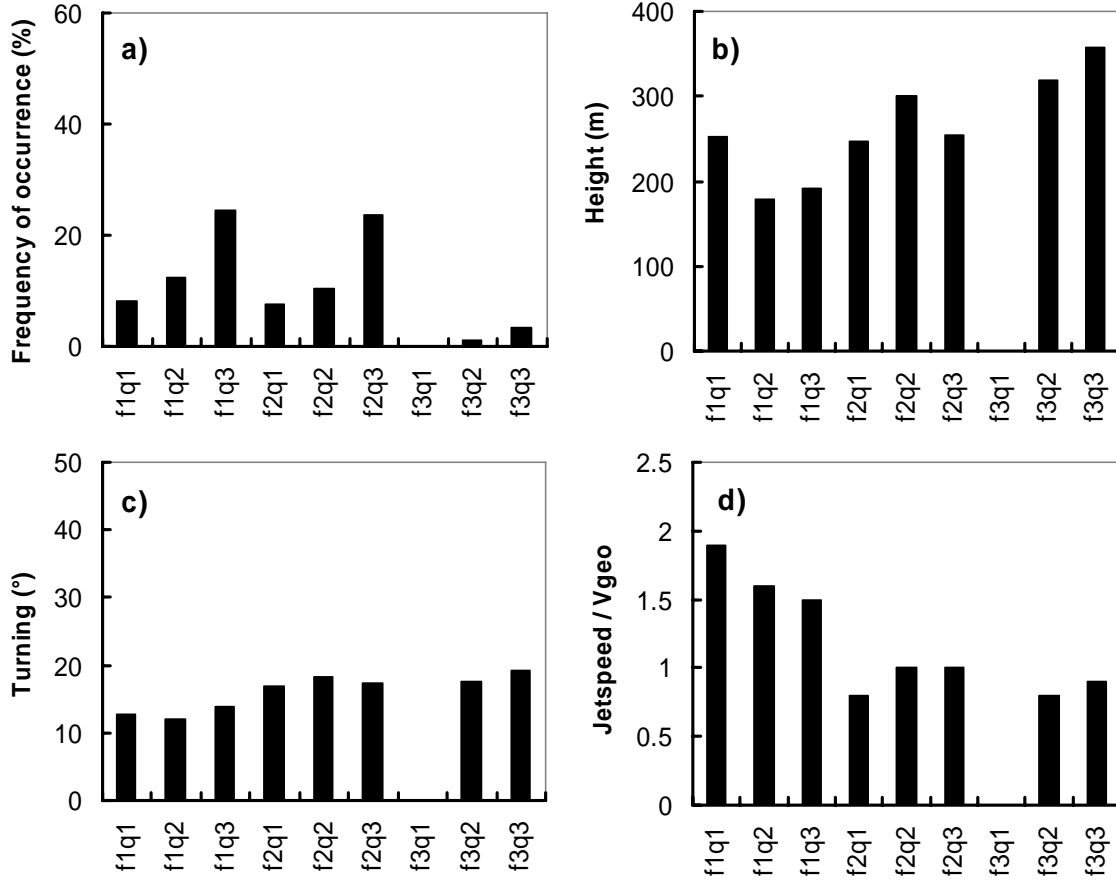


Figure 2.11: As Figure 10, but now for ERA40 (after the ERA40 archive ended (August 2002) operational ECMWF output was used).

The ERA40 LLJ characteristics for Cabauw are given in Figure 2.11. The frequency of occurrence of LLJs (Figure 2.11a) is much lower in the model than in the observations. However, the tendencies as a result of varying V_g and ΔT_{iso} are clearly present: the number of LLJs increases significantly for increasing nocturnal cooling and for the highest class of V_g the frequency of occurrence is very much decreased. The average height of the LLJ (Figure 2.11b) is systematically overestimated by ERA40 by about 50 to 100 m (except for the class f1q1). Moreover, in the model the individual jets are much more spread out in height than in the observations: this is expressed in the much higher level of the wind speed minimum above the LLJ (not shown). The turning of the wind vector between the LLJ height and the lowest model level (~ 10 m) (Figure 2.11c), is too

low compared to the observed values. Also the speed of the LLJs is underestimated in the model (Figure 2.11d).

To summarize, the frequency of LLJs in ERA40 is underestimated at Cabauw. The same is true for the turning across the boundary layer and the speed of the jet, while the jet height is overestimated. This is consistent with the results of Bosveld and Beyrich (2004) and agrees with the findings of Cheinet et al. (2005), who attribute this disability to represent the LLJ in a proper way to deficiencies in the SBL mixing formulation. To obtain optimal model scores on the synoptic scale, the model applies stability functions for vertical diffusion in stable conditions that allow for much more mixing than can be motivated by field experiments. The consequent degradation of the representation of the SBL is taken for granted. Comparable results were found in the first GEWEX Atmospheric Boundary Layer Studies (GABLS1) intercomparison study on a stably stratified case by Cuxart et al. (2006) and by Baas et al. (2008a), who analyzed different parameter settings of a TKE-closure model. Since modeling of the LLJ seems not very sensitive to vertical resolution (Ghan et al., 1996), we expect that the deficiencies in the physical parameterization dominate over possible influences of resolution.

2.8 Concluding remarks

The main objective of this study was to provide a climatology of low-level jets (LLJs) to facilitate the evaluation of atmospheric models. Therefore, 7 years of half-hourly observations of wind speed profiles from the Cabauw measuring site in The Netherlands were analyzed. Data from a 1290 MHz wind profiler were used to extend the measurements of a 200 m high tower to obtain wind and temperature profiles up to 1420 m above ground level. In about 20% of the nights a substantial maximum in the nocturnal wind speed profile occurs. At Cabauw, LLJs typically have a speed of $6 - 10 \text{ m s}^{-1}$ and are situated at 140 – 260 m. Despite predominant south westerly wind directions, most LLJs have a more easterly to southerly directions. Analysis of vertical profiles of virtual temperature showed that the height of the LLJ is often close to the height of the nocturnal inversion.

Moderate geostrophic forcing and high radiative cooling (no clouds) are the most favorable circumstances for the development of a substantial LLJ. For stronger nocturnal cooling and lower geostrophic forcing, the LLJs form at a lower altitude. The difference in wind direction between the LLJ and the 10 m wind increases for increasing nocturnal cooling. These results suggest that frictional decoupling after sunset as a result of stable stratification is the main mechanism for LLJ formation at Cabauw. Indeed, about 60% of the detected LLJs show

features of a well-developed inertial oscillation. However, the characteristics of these jets (in terms of height and turning compared to the 10 m wind) do not differ from those of the remaining 40% of the LLJs.

To illustrate the applicability of the derived climatology for model evaluation, we compared some of our results with output from the ERA40 archive. It appears that LLJs in the model are less frequent and situated at a higher level than in the observations. The turning across the boundary layer is smaller than observed. Also the speed of the LLJ is underestimated.

Acknowledgements

We acknowledge Martin Köhler (ECMWF) for providing operational output from the ECMWF model for the grid-point close to Cabauw. Three anonymous reviewers are acknowledged for their constructive comments. The first author has been supported by the Netherlands Organization for Scientific Research (NWO), in particular through the project “land surface climate and the role of the stable boundary layer.”

3 Exploring Self-Correlation in Flux-Gradient Relationships for Stably Stratified Conditions*

Abstract. *In this paper the degree of scatter in flux-gradient relationships for stably stratified conditions is analyzed. It is generally found that scatter in the dimensionless lapse rate ϕ_h is larger than in the dimensionless shear ϕ_m when plotted versus the stability parameter z/Λ (where Λ is the local Obukhov length). We explain this phenomenon to be a result of self-correlation due to the occurrence of the momentum and the heat flux on both axes, measurement uncertainties and other possibly relevant physical processes left aside. It is shown that the ratio between relative errors in the turbulent fluxes influences the orientation of self-correlation in the flux-gradient relationships. In stable conditions the scatter in ϕ_m is largely suppressed by self-correlation while for ϕ_h this is not the case (vice versa for unstable stratification). An alternative way of plotting is discussed for determining the slope of the linear ϕ_m -function.*

3.1 Introduction

Flux-gradient relationships are used to relate gradients of mean atmospheric profiles to turbulent fluxes. The concept of flux-gradient relationships has proven to be very useful in estimating surface fluxes both in atmospheric models and from observed profiles. The relevant quantities to relate fluxes and gradients are obtained from dimensional analysis. Consequently, the functional form of the flux-gradient relationships must be found by experiment. Some of the current problems in atmospheric boundary layer modeling (e.g. Holtslag, 2006), may be associated with uncertainties in the form of the flux-gradient relationship. In the near neutral regime, different studies on the determination of the flux-gradient relationships show similar results with little scatter. In contrast, the proposed functional forms diverge considerably for stronger stability (Högström, 1988, 1996; Andreas, 2002).

For the stable boundary layer (SBL) a systematic difference in scatter between the dimensionless shear ϕ_m and the dimensionless lapse rate ϕ_h is found when plotted versus the stability parameter z/Λ (where Λ is the local Obukhov length). Typically, scatter in ϕ_h is larger than in ϕ_m for a large majority of field experiments (see e.g. Oncley et al., 1996; Forrer and Rotach, 1997; Duynkerke,

* This Chapter has been published as: Baas, P., G.J. Steeneveld, B.J.H. van de Wiel, and A.A.M. Holtslag, 2006: Exploring self-correlation in stably stratified conditions. *J. Atmos. Sci.*, **63**, 3045-3054.

1999; Howell and Sun, 1999; Yagüe et al., 2001; Cheng and Brutsaert, 2005 and Steeneveld et al., 2006). Figure 3.1 illustrates this point for CASES-99 observations.

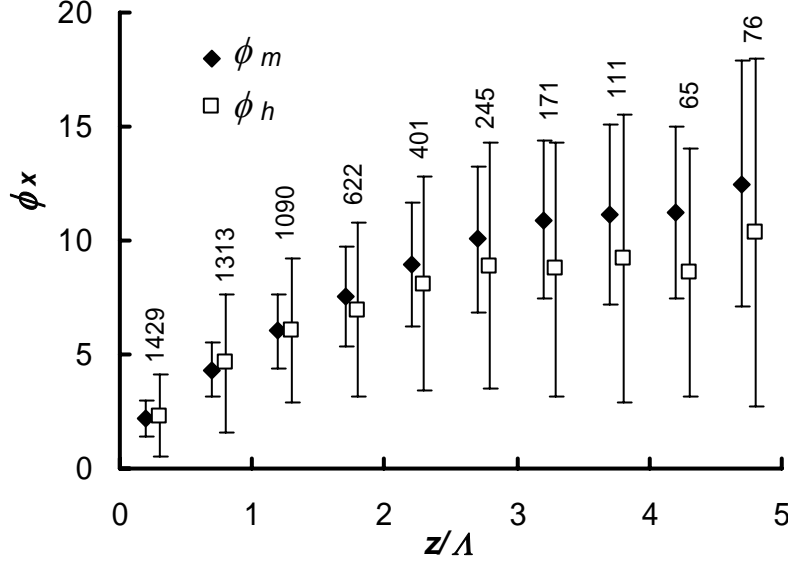


Figure 3.1: Dimensionless shear (ϕ_m) and lapse rate (ϕ_h) versus stability (z/Λ) for CASES-99 observations. Error bars indicate one standard error around the mean. For each class of z/Λ the number of cases is indicated. For each stability class the number of observations is indicated.

In this paper we explain the difference in scatter between ϕ_m and ϕ_h to be a result of self-correlation. Self-correlation is also referred to in literature as ‘spurious correlation’ or the ‘shared variable problem’ and arises when one (dimensionless) group of variables is plotted against another, and the two groups under consideration have one or more common variables (e.g. Hicks, 1978; Kenney, 1982; Aldrich, 1995). In that case, correlation is partly caused by artificial, mathematical reasons, apart from physical and observational aspects. For plots suffering from self-correlation, the amount of scatter is not directly related to the quality of the data or the validity of the physical relationship under consideration.

In general, the influence of self-correlation depends on two factors. Firstly, on the relative variation of the fundamental variables, $V_{x_i} = \sigma_{x_i} / \overline{x_i}$. Here σ_{x_i} denotes the standard error of a certain variable x_i . When V_{x_i} of the common variable is large compared to V_{x_i} of the other variables, the degree of self-correlation is considerable (Kim, 1999; Klipp and Mahrt, 2004). Secondly, the relationship between the orientation of the self-correlation on the one hand and of

the true physical correlation on the other hand is important. Depending on this relationship, the influence of self-correlation can be either negligible or very large.

Dimensional analysis is a widely applied tool in boundary-layer meteorology (e.g. Stull, 1988). However, often not sufficient independent scaling variables are present to construct completely independent dimensionless groups (Andreas and Hicks, 2002). As a consequence, some amount of self-correlation is often inevitable.

The aim of this paper is to explore the influence of self-correlation in ϕ_m and ϕ_h for stable conditions. Furthermore we discuss the influence of self-correlation as a function of atmospheric stability and we discuss an alternative way of plotting for determining the slope of the linear ϕ_m -function independent of self-correlation. While earlier studies mainly examined the effect of the shared momentum flux, here we investigate the combined effect of the momentum flux *and* the heat flux on the influence of self-correlation.

In Section 3.2 the background of Monin-Obukhov similarity theory (MOS) is briefly summarized. Section 3.3 gives a short description of the observational data and Section 3.4 presents a sensitivity analysis on the influence of self-correlation on the flux-gradient relationships. In Section 3.5 the stability dependence of self-correlation will be investigated and in Section 3.6 we will apply an alternative technique to illustrate the influence of self-correlation. In Section 3.7 we suggest some characteristics we think a new scaling approach should meet. Finally in Section 3.8 we draw conclusions.

3.2 Monin-Obukhov similarity theory

Turbulent motions in the atmospheric surface layer can be well described in terms of MOS (e.g. Stull, 1988). This theory states that under homogeneous and stationary conditions every dimensionless group is a universal function of z/L , where z is the height above the surface and

$$L = - \frac{u_{*0}^3}{k \frac{g}{\bar{\theta}} \overline{w' \theta' _0}} \quad (3.1)$$

is the Obukhov length. Here k is the Von Kármán constant (taken as 0.4; Högström, 1996), g the acceleration due to gravity, $\bar{\theta}$ is the mean potential temperature. The surface friction velocity is defined as

$$u_{*0} = \sqrt{\frac{\tau_0}{\rho}} = \left(\overline{u' w'_0}^2 + \overline{v' w'_0}^2 \right)^{1/4}, \quad (3.2)$$

and $\overline{w' \theta' _0}$ is the surface kinematic turbulent heat flux. The momentum flux is denoted by τ_0 and ρ (1.2 kg m^{-3}) is the air density. Overbars indicate mean values; primes indicate deviations from the mean.

The dimensionless shear ϕ_m and the dimensionless lapse rate ϕ_h are defined as:

$$\phi_m\left(\frac{z}{L}\right) = \frac{kz}{u_{*0}} \frac{\partial \bar{U}}{\partial z} \quad (3.3)$$

$$\phi_h\left(\frac{z}{L}\right) = \frac{kz}{\theta_{*0}} \frac{\partial \bar{\theta}}{\partial z} = -\frac{kzu_{*0}}{(\overline{w'\theta'})_0} \frac{\partial \bar{\theta}}{\partial z}. \quad (3.4)$$

Here \bar{U} is the mean wind speed and $\theta_{*0} = -\overline{w'\theta'}_0 / u_{*0}$ is a turbulent temperature scale.

In principle MOS is only valid in the surface layer. Above this layer the magnitude of the fluxes generally decreases with height in the SBL (e.g. Stull, 1988) and Monin-Obukhov scaling is no longer appropriate. Alternatively, Nieuwstadt (1984) used *local fluxes* instead of surface fluxes (local scaling). All dimensionless groups now depend on z/Λ , where

$$\Lambda = -\frac{u_*^3}{k \frac{g}{\theta} \overline{w'\theta'}} \quad (3.5)$$

is the *local* Obukhov length at height z (Nieuwstadt, 1984; Holtslag and Nieuwstadt, 1986). MOS can be considered as a special case of local scaling theory. In the remainder of this paper the local scaling approach will be applied.

3.3 Observational data

To illustrate our results, we use observations from the CASES-99 measurement campaign (Poulos et al., 2002), which was organized in October 1999, 50 km east of Wichita, Kansas, U.S.A (37.65°N, 96.74°W; ~ 440 m a.s.l.), over gently rolling terrain with slopes from 0.1 to 0.8 degrees. The experimental area was covered with prairie-grass with a roughness length of 0.03 m.

A 60-meter tower was equipped with a dense vertical array of 20 Hz Campbell Scientific CSAT or Applied Technologies K-style sonic anemometers at 10, 20, 30, 40, 50 and 55 m. Temperature profiles are obtained at six levels from slow response aspirated temperature/humidity sensors at 5, 15, 25, 35, 45 and 55 m. All the data were obtained from

<http://www.atd.ucar.edu/rtrf/projects/cases99/asciiDownload.jsp>.

Around the main mast a network of flux stations was set-up. Hartogensis and De Bruin (2005) operated a 10 m mast with a CSAT3 sonic anemometer and a KH20 Krypton hygrometer at 2.6 and 10.2 m. To investigate the impact of self-correlation as function of atmospheric stability, we use eddy-correlation data from the 10.2 m level. To calculate turbulent fluxes, the raw data are processed by a software package (Van Dijk and Moene, 2004; see also

<http://www.met.wau.nl/projects/jep/report/ecrump.pdf>). The package provides a statistical error for each flux variable. This error is mainly based on the measurement accuracy and the number of independent samples from which the averaged flux value is composed. For normally distributed samples the statistical error equals two times the standard deviation.

3.4 Influence of self-correlation on flux-gradient relationships

The impact of self-correlation can be investigated by imposing errors on the common variables. When the resulting contaminated points move roughly along the reference curve, self-correlation has significant influence. By ‘reference curve’ we mean a first order guess of the relationship, based on earlier studies. To be more specific, for the flux-gradient relationships in the SBL this is a log-linear relationship in the near-neutral regime. With increasing stability, the functions gradually deviate from log-linear. Of course, in principle, even this first order guess in itself suffers from self-correlation, but this second order effect is discarded.

By imposing a 10% error on u_* , Andreas and Hicks (2002) show that self-correlation indeed causes a difference in scatter between ϕ_m and ϕ_h for unstable conditions. For stable conditions, Klipp and Mahrt (2004) found that self-correlation explains 65% of the variance between ϕ_m and z/Λ , owing to the occurrence of u_* in both quantities.

In this section we will impose errors on both the momentum flux τ and the sensible heat flux H . The erroneous fluxes can be expressed as

$$\begin{aligned}\tau_{error} &= \tau_{true} + \Delta\tau \\ H_{error} &= H_{true} + \Delta H,\end{aligned}\tag{3.6}$$

where, for example, $\Delta\tau$ and ΔH can be considered as random or systematic measurement errors. In this study we ignore uncertainties in the gradients, although these can be considerable (Akima, 1970; Oncley et al., 1996; Frentzen and Vogel, 2001). When we reduce the errors $\Delta\tau$ and ΔH to infinitesimal values, we obtain from Equation (3.6)

$$\begin{aligned}\tau_{error} &= \tau_{true} \left(1 + \frac{\delta\tau}{\tau_{true}} \right) \\ H_{error} &= H_{true} \left(1 + \frac{\delta H}{H_{true}} \right).\end{aligned}\tag{3.7}$$

At first we assume the relative errors in τ and H to be equal, so $\delta\tau/\tau = \delta H/H$. In this case, the direction in which a reference point shifts as a result of the imposed errors reads:

$$\left(\frac{\partial \phi_m}{\partial (z/\Lambda)} \right)_{error} = \left(\frac{\partial \phi_h}{\partial (z/\Lambda)} \right)_{error} = \frac{\phi_m}{z/\Lambda} = \frac{\phi_h}{z/\Lambda}. \quad (3.8)$$

This result is found by differentiating ϕ_m , ϕ_h and z/Λ with respect to both τ and H and using the assumption $\delta\tau/\tau = \delta H/H$ (see Appendix 3A). Equation (3.8) states that the effect of an imposed error $\delta\tau/\tau = \delta H/H$ on a reference point in the $(\phi, z/\Lambda)$ -space causes a deviation from the reference point along a line through the reference point and the origin. Equation (3.8) indicates that the response of ϕ_m and ϕ_h on imposed errors is exactly equal. Consequently, when $\delta\tau/\tau = \delta H/H$, any difference in observed scatter between ϕ_m and ϕ_h *cannot* be explained as an effect of self-correlation. For the Businger-Dyer relationships ($\phi_m = \phi_h = 1 + 5z/\Lambda$; Dyer, 1974), this result implies that for increasing stability, the deviation becomes more aligned with the slope of the ϕ -function, β (Figure 3.2).

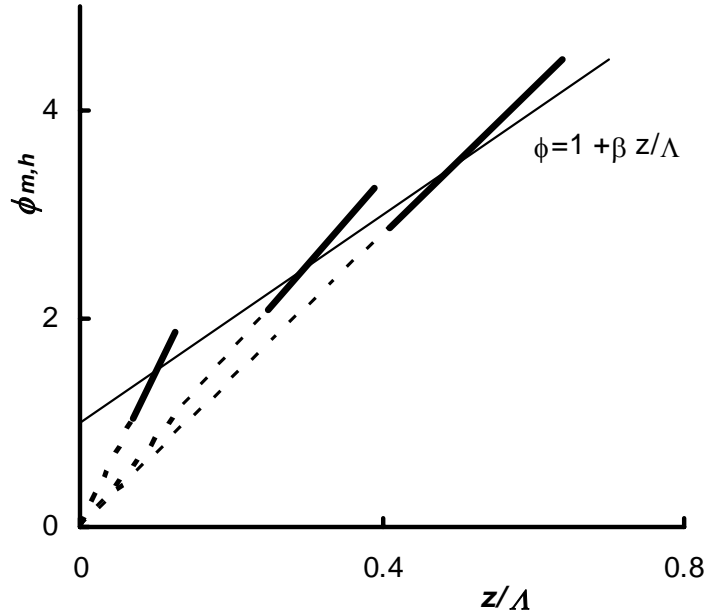


Figure 3.2: Effect of errors in the momentum flux and the heat flux ($\delta H/H = \delta\tau/\tau$) on the position of a reference point in the $(\phi, z/\Lambda)$ -space. Application to the Businger-Dyer relations ($\beta = 5$).

In reality the assumption $\delta\tau/\tau = \delta H/H$ is not generally valid (see Section 3.5). Because often the exact correlation between $\delta\tau/\tau$ and $\delta H/H$ is unknown, we examine four limit situations of the error ratio parameter $\alpha = \frac{\delta H/H}{\delta\tau/\tau}$:

- a) $\delta\tau/\tau = \delta H/H$ ($\alpha = 1$; as above)
- b) $\delta\tau/\tau = 0$ and $|\delta H/H| > 0$ ($\alpha \rightarrow |\infty|$)
- c) $|\delta\tau/\tau| > 0$ and $\delta H/H = 0$ ($\alpha = 0$)
- d) $\delta\tau/\tau \neq \delta H/H$ ($-\infty < \alpha < \infty$)

The magnitude of the imposed relative errors is randomly taken from a uniform distribution and is between -20% and +20%. Starting from a reference point, for each of the four limit situations 100 artificial data points are generated. Figure 3.3 shows the results of this numerical simulation. The solid lines correspond to the reference curve, in this case the Beljaars-Holtslag 1991 formulation for momentum. The results of the current study do not depend on the choice of this specific function. Other realistic functions lead to similar conclusions.

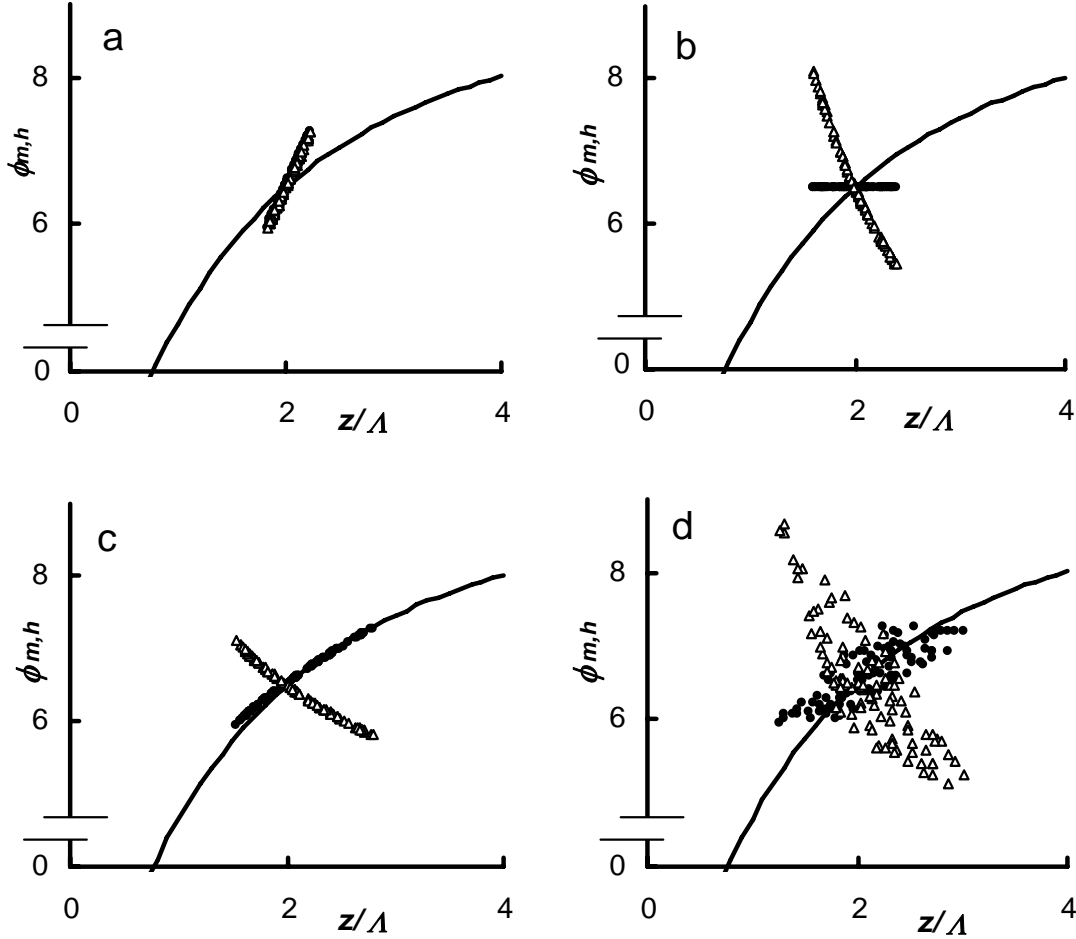


Figure 3.3: The impact of errors in the momentum flux and the heat flux on plots of ϕ_h and ϕ_m versus z/Λ . Open triangles (Δ) indicate ϕ_h , solid circles (\bullet) indicate ϕ_m . The solid line represents the BH91 function for momentum. The cases a), b), c) and d) refer to different values of the ratio between $\delta\tau/\tau$ and $\delta H/H$ as defined in the text. The maximum error margin amounts $|20\%|$.

Figure 3.3a confirms our analytical approach of Equation (3.8): ϕ_m and ϕ_h behave similarly and all points are on a straight line through the reference point and the origin. When the relative errors in τ and the H are *not equal* as in the cases

b), c) and d), the flux-gradient functions indeed scatter differently. In these cases the random ϕ_m -data scatters approximately along the reference curve, while for ϕ_h the data scatters roughly perpendicular to this curve. For case c) this leads to the interesting paradoxal result that when τ contains an error and H is perfect, $\phi_m(z/\Lambda)$ shows little scatter while $\phi_h(z/\Lambda)$ shows large scatter. Except for Figure 3.3d all points are on straight or slightly bended lines. Figure 3.3d shows much more scatter, because contrary to the cases a), b) and c), there is no fixed correlation between $\delta\tau/\tau$ and $\delta H/H$ in this case ($-\infty < \alpha < \infty$). In fact, in case d) the three other cases are enclosed. Figure 3.3 also infers that the *magnitude* of the deviations depends on α . For example, the maximum deviation in case a) is much smaller than in case d) for both ϕ_m and ϕ_h .

In general, when $\delta\tau/\tau \neq \delta H/H$, ϕ_h will always have more scatter around the reference curve than ϕ_m for a given dataset in stable conditions. This is a non-physical effect that rises from the mathematical expressions for ϕ_m , ϕ_h and z/Λ . For ϕ_m the shift along the reference curve demonstrates that self-correlation has substantial influence, while for ϕ_h self-correlation only is important when $\delta\tau/\tau = \delta H/H$. The different behavior of ϕ_m and ϕ_h illustrates the fact that just common variables on both axes does not automatically imply that self-correlation is important. Only when the mathematical relationship of the common variables is roughly in line with the physical relationship (like in ϕ_m), scatter remains hidden and self-correlation will have significant influence.

For a given α the direction in which a certain reference point will shift due to errors in the fluxes reads for $\phi_m(z/\Lambda)$

$$\left(\frac{\partial \phi_m}{\partial (z/\Lambda)} \right)_{\text{error}} = \left(\frac{-0.5}{\alpha - 1.5} \right) \frac{\phi_m}{z/\Lambda}, \quad (3.9)$$

and for $\phi_h(z/\Lambda)$

$$\left(\frac{\partial \phi_h}{\partial (z/\Lambda)} \right)_{\text{error}} = \left(\frac{0.5 - \alpha}{\alpha - 1.5} \right) \frac{\phi_h}{z/\Lambda}. \quad (3.10)$$

These expressions are derived in Appendix 3A and agree with the limit situations of Figure 3.3. For example, when $\alpha = 1$ as in Figure 3.3a, Equations (3.9) and (3.10) both reduce to Equation (3.8). In fact, these equations predict the orientation of self-correlation for a given value of α in a certain point $(z/\Lambda, \phi_{m,h})$.

The above analysis can also be applied to the unstable regime. As such, it can be shown that the effect on scatter in ϕ_m and ϕ_h is then mostly opposite: in the unstable regime ϕ_m exhibits more scatter than ϕ_h (see also Andreas and Hicks, 2002 and Johansson et al., 2001).

3.5 Stability dependence of self-correlation

In Section 3.4 we found that α influences the orientation of scatter in flux-gradient plots. In practice however, it is hard to estimate the actual value of α . In this section we show how α may be influenced by atmospheric stability.

For our analysis we use eddy-correlation data from CASES-99, but similar results were obtained with routine flux observations from the Wageningen University weather field (Jacobs et al., 2003). With the statistical error described in Section 3.3, relative errors of τ and H can be obtained according to

$$\frac{\Delta x}{x} = \frac{se(x)}{x_{ref}}, \quad (3.11)$$

where x is τ or H and $se(x)$ is the corresponding statistical error. Note that the statistical error is not equal to the actual measurement error and does also not provide information about the sign of it. Therefore, it is impossible to determine unambiguously the effect on the orientation of scatter in the flux-gradient plots. However, it is still possible to indicate that a stability dependence is present. For example, when $se(\tau) \ll se(H)$, it is reasonable to assume that most of the true errors in τ will also be much smaller than those in H .

We analyse α as a function of stability and anticipate which of the four cases from Figure 3.3 is more likely to occur. Figure 3.4a shows that in the near neutral situation, the value of $\delta H/H$ is likely to be larger than the value of $\delta \tau/\tau$. This is caused by the fact that in these conditions τ has much larger values than H . In general, smaller values of a certain variable are accompanied by larger relative errors. In the weakly stable regime (Figures 3.4b, c) the relative errors are slightly related, especially for small error values. To quantify the spread, we made a linear fit to the data (using perpendicular offsets) and calculated for each data point the absolute deviation from the fit. The 75th percentile of these deviations is used as an indication for the spread. In the very stable regime (Figure 3.4d), this measure is increased compared to the weakly stable regime demonstrating that the relationship between the relative errors in the fluxes disappears. The difference in behavior between the stability regimes demonstrates that α depends on stability. With respect to our analysis on self-correlation this implies that, in a certain flux-gradient plot, the orientation of scatter due to errors in the turbulent fluxes also depends on z/Λ .

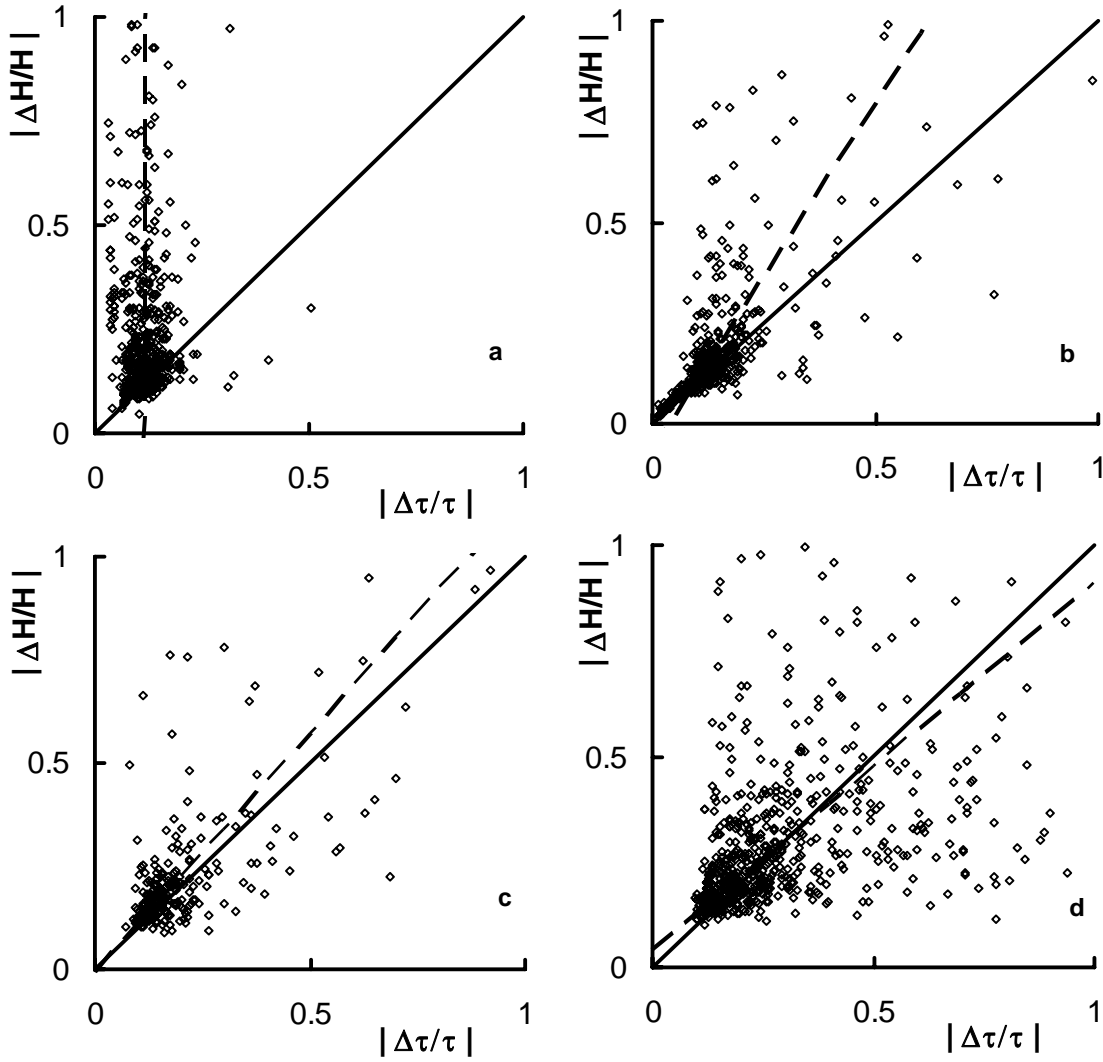


Figure 3.4: Observed stability dependence of the ratio $\alpha = (\delta H/H)/(\delta \tau/\tau)$ for CASES-99. a) $0 < z/L < 0.1$, b) $0.1 < z/L < 0.5$, c) $0.5 < z/L < 1$, d) $z/L > 1$. The solid lines indicate the 1:1 line ($\alpha = 1$), the dashed lines indicate the least square fit based on perpendicular offsets for each stability regime. As a measure of scatter we use the 75th percentile of the deviations from the fit. For the panels a), b), c) and d) the respective values are 0.036, 0.029, 0.060 and 0.109.

To summarize, the near neutral situation of Figure 3.4a compares to Figure 3.3b, the weakly stable situation of Figures 3.4b and 3.4c roughly compares to Figure 3.3a and the very stable situation of Figure 3.4d compares to Figure 3.3d.

3.6 Randomizing real observations

In this section we illustrate our earlier findings by applying an alternative method to examine self-correlation. We randomize the original dataset, by mixing all available values for each of the different variables (τ , H , dU/dz , etc.) at random. In this way the characteristic statistical distributions of the variables are conserved, which is important because only then a good comparison with the real data is possible. From the randomized data we recompute z/Λ , ϕ_m and ϕ_h . It is clear that the new ‘data points’ do not have any physical meaning at all (Hicks, 1981; Andreas and Hicks, 2002; Klipp and Mahrt, 2004; Mahrt and Vickers, 2003).

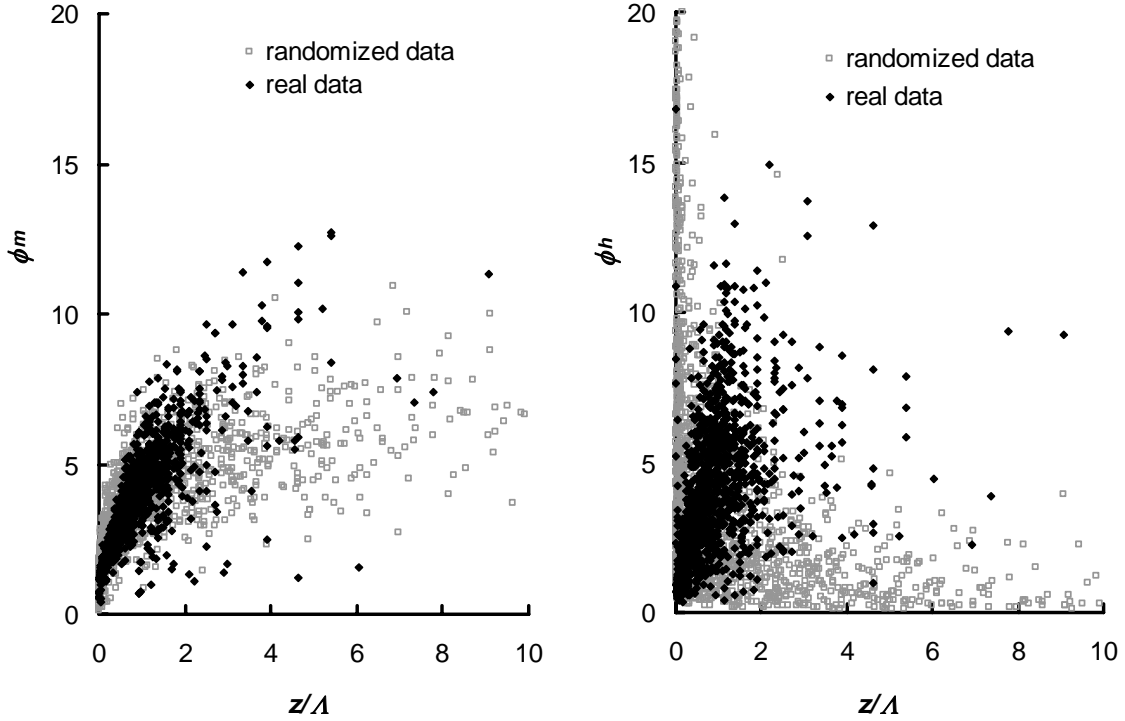


Figure 3.5: Flux-gradient relationships for real and randomized data for ϕ_m and ϕ_h versus z/Λ . Black dots represent real data, grey squares randomized data.

Figure 3.5 shows the result of our analysis. For ϕ_m , the unphysical randomized points are close to the original data. This occurs because the common variable u_* appears in the *denominator* in both ϕ_m and z/Λ , combined with the fact that the physical relationship between ϕ_m and z/Λ has a positive slope from itself. This result corresponds to the ‘parallel shift’ we found in Section 3.4 and demonstrates again that $\phi_m(z/\Lambda)$ is heavily influenced by self-correlation.

Contrary to ϕ_m , plots of ϕ_h versus z/Λ are not affected by self-correlation in the sense that erroneous or even randomized data can still give misleadingly good results. However, the randomized data do not look completely chaotic for ϕ_h . Just as in the case of ϕ_m , the statistics of the common variables are reflected. The

difference is that in $\phi_h u_*$ appears in the *nominator*, which causes the randomized ϕ_h data to show some hyperbolic relationship. This behavior corresponds to the ‘normal shift’ of a reference point relative to the reference curve that we found in Section 3.4.

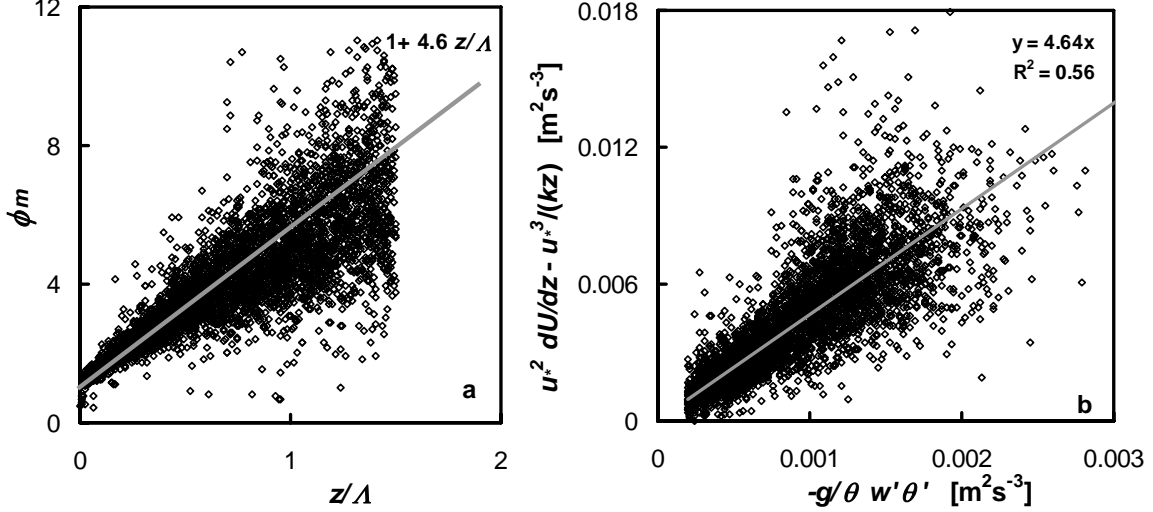


Figure 3.6: Standard plot of ϕ_m vs. z/Λ (a) and an alternative plot (b) from which the slope of the ϕ_m vs. z/Λ can be estimated independent of self-correlation. The grey line in panel b) is a least square fit to the data. The slope of this fit is passed on to panel a) to illustrate that this slope gives indeed a reasonable fit for the $\phi_m(z/\Lambda)$ -data.

The result of Figure 3.5a raises the question if there is *any* information in a plot of ϕ_m versus z/Λ . The small differences between the randomized data and the real data cannot result from limited data ranges: Table 3.1 shows that for each variable the range amounts at least a factor of 10, which is considerable. Fortunately, as is also known from practice, ϕ_m indeed contains useful information. We can determine the slope of ϕ_m versus z/Λ independent of self-correlation by anticipating a linear relationship of the type $\phi_m = 1 + \beta z/\Lambda$. Noting the definitions of ϕ_m and z/Λ and multiplying both sides with $u_*^3/(kz)$, we can plot $u_*^2 dU/dz - u_*^3/(kz)$ versus $-g/\theta \overline{w'\theta'}$ (Figure 3.6b). The slope of this plot provides an independent estimate for the slope β of the standard ϕ_m plot as given in Figure 3.6a. We limit our analysis to data for which $z/\Lambda < 1.5$, since only then a linear relationship can be assumed (e.g. Holtslag and De Bruin 1988; Beljaars and Holtslag, 1991). Comparing Figures 3.6a and 3.6b shows that the slopes of both figures agree well. This indicates that, contrary to the scatter, the *shape* of ϕ_m is *not* very sensitive to self-correlation. Note that scatter in Figure 3.6b is small, despite the fact that we plot a difference term on the y-axis.

3.7 Discussion and future research

Scatter can be misleadingly small in plots where self-correlation is important. Consequently, there is need for an alternative way to relate fluxes and profiles. One way to deal with this problem is to search for alternative scaling approaches which are less vulnerable to self-correlation (e.g. Klipp and Mahrt, 2004).

The Buckingham-Pi theorem does not prescribe how to compose the different dimensionless groups. When information on relative errors of the different variables (u_* , H , $\partial U/\partial z$, $\partial \theta/\partial z$, etc.) is available, it would be possible to construct the dimensionless groups in the most advantageous way. In practice this means that the most uncertain variables (here: the turbulent fluxes) are raised to the lowest power in order to minimize the influence of their high relative error. Because in *stable* conditions fluxes are much smaller than gradients, fluxes should be raised to the lowest possible powers. In the *unstable* regime the situation is opposite: fluxes are large and gradients are small. Consequently, higher powers for the fluxes (e.g. u_*^3) combined with lower powers for the gradients are preferable. Based on this arguments, it can be stated that MOS is much more suitable for unstable than for stable conditions. MOS can be regarded as a ‘flux-based’ scaling approach, while for the SBL a ‘gradient-based’ scaling might be more suitable.

For the SBL, in many cases the above reasoning leads to a scaling based on the gradient Richardson number, which is given by

$$Ri = \frac{g}{\theta} \frac{\partial \bar{\theta}}{\partial z} \bigg/ \left(\frac{\partial \bar{U}}{\partial z} \right)^2. \quad (3.12)$$

By using a Ri-based scaling for the stable regime, Klipp and Mahrt (2004) also largely circumvent the problem of self-correlation (see also Sorbjan, 2006).

3.8 Conclusions

Flux-gradient relationships are traditionally used to relate turbulent fluxes and atmospheric mean profiles in the atmospheric boundary layer. However, self-correlation significantly influences the relationships between the dimensionless shear ϕ_m and the dimensionless lapse rate ϕ_h versus the stability parameter z/Λ . In general, self-correlation arises when two parameters share some common variable. For $\phi_h(z/\Lambda)$ and $\phi_m(z/\Lambda)$, the common variables are the momentum flux τ and the heat flux H . The former appears in ϕ_m , ϕ_h and z/Λ , the latter in ϕ_h and z/Λ . Here we consider stable stratification only.

The impact of self-correlation on the flux-gradient relationships depends highly on the ratio of relative errors in the momentum flux and the heat flux. This ratio governs both the orientation and the magnitude of the scatter. In general, scatter in ϕ_m remains unrealistically small, because the data is scattered roughly *along* the physical curve. Contrary, for ϕ_h scatter is much larger, because the data

is scattered roughly *perpendicular* to the physical curve. ϕ_h will therefore always show more scatter than ϕ_m . This holds only for the stable regime. In the unstable regime the effect of self-correlation is mostly reversed. In this analysis, errors associated with possible violations of Monin-Obukhov similarity theory and errors in $\partial\theta/\partial z$ and $\partial U/\partial z$ are not taken into account, although in reality these are also important.

When imposed relative errors on the fluxes are *equal*, the difference in behavior between ϕ_h and ϕ_m disappears: in both cases a reference point shifts along a straight line through this reference point and the origin. Therefore no difference in scatter between ϕ_m and ϕ_h arises in this special case. However, it is not realistic to assume the ratio between the relative errors of the fluxes to be a constant within a single dataset, because this ratio depends strongly on stability. In practice this means that in a certain flux-gradient plot, the influence of self-correlation on the orientation of the scatter also varies with stability. While self-correlation occurs in both ϕ_m and ϕ_h , only in case of ϕ_m the influence is significant. Self-correlation only becomes important when the mathematical relationship of the common variables is roughly *in line* with the physical relationship of the parameters that include them.

Overall, current practice of evaluating ϕ_m and ϕ_h functions from field data is troublesome. The large influence of self-correlation may lead to false confidence in the found relationship, in particular for ϕ_m . By plotting quantities in an alternative way, we are able to determine the slope of ϕ_m independent of self-correlation. It seems that, contrary to the scatter, the *slope* of ϕ_m is *not* very sensitive to self-correlation. The evaluation of ϕ_h does not suffer from artificially enhanced correlation. However, due to the factor u_*^3 , small deviations in u_* may lead to large scatter, which can hamper an accurate estimation of ϕ_h .

Acknowledgements

We thank our colleagues Oscar Hartogensis and Henk de Bruin for providing their eddy-correlation data, as well as all other researchers and technicians who contributed to CASES-99. We also thank two unknown reviewers for their constructive comments and suggestions. The first author has been supported by the Netherlands Organization for Scientific Research (NWO), in particular through the project “land surface climate and the role of the stable boundary layer”.

Appendix 3A: Sensitivity of flux-gradient relationships to changes in the momentum and the heat flux

The dimensionless wind shear, ϕ_m , and the dimensionless lapse rate, ϕ_h , are given by

$$\phi_m = \frac{kz}{\sqrt{\tau/\rho}} \frac{\partial U}{\partial z} \text{ and } \phi_h = -\frac{kz\rho c_p \sqrt{\tau/\rho}}{H} \frac{\partial \theta}{\partial z}. \quad (\text{A3.1})$$

According to local scaling theory these dimensionless groups are universal function of

$$\frac{z}{\Lambda} = \zeta = -\frac{zgk}{T} \frac{H}{\rho c_p} \left(\frac{\tau}{\rho} \right)^{-3/2}. \quad (\text{A3.2})$$

We are interested in $\frac{\partial \phi_{m,h}}{\partial \zeta}$ as a result of imposed errors on the common variables, the momentum flux τ and the sensible heat flux H .

We assume the relative errors in the fluxes to be related: $\alpha \frac{\delta \tau}{\tau} = \frac{\delta H}{H}$. (A3.3)

First we calculate $\delta \phi_m$, $\delta \phi_h$ and $\delta \zeta$ separately, after which we perform the division. Using formal differentiation rules and Equation (A3.3) we obtain

$$\delta \phi_m = kz\rho^{1/2} \frac{\partial U}{\partial z} \delta \left(\frac{1}{\tau^{1/2}} \right) \equiv C_1 \delta \left(\frac{1}{\tau^{1/2}} \right) = -\frac{1}{2} \frac{\delta \tau}{\tau^{3/2}} C_1 \quad (\text{A3.4})$$

$$\delta \phi_h = -\frac{kz\rho c_p}{\rho^{1/2}} \frac{\partial \theta}{\partial z} \delta \left(\frac{\tau^{1/2}}{H} \right) \equiv C_2 \delta \left(\frac{\tau^{1/2}}{H} \right) = \frac{1/2 H \delta \tau - \tau \delta H}{\tau^{1/2} H^2} C_2 = \frac{(1/2 - \alpha) \delta \tau}{\tau^{1/2} H} C_2 \quad (\text{A3.5})$$

$$\delta \zeta = -\frac{zgk}{T} \frac{\rho^{3/2}}{\rho c_p} \delta \left(\frac{H}{\tau^{3/2}} \right) \equiv C_3 \delta \left(\frac{H}{\tau^{3/2}} \right) = \left(\frac{\delta H}{\tau^{3/2}} - \frac{3}{2} \frac{H \delta \tau}{\tau^{5/2}} \right) C_3. \quad (\text{A3.6})$$

Using Equations (A3.4), (A3.6) and (A3.3) we can now calculate $\frac{\partial \phi_m}{\partial \zeta}$:

$$\frac{\partial \phi_m}{\partial \zeta} = \frac{-\frac{1}{2} \frac{\delta \tau}{\tau^{3/2}} C_1}{\left(\frac{dH}{\tau^{3/2}} - \frac{3}{2} \frac{H \delta \tau}{\tau^{5/2}} \right) C_3} = \frac{-\frac{1}{2} \frac{\delta \tau}{H} C_1}{\left(\frac{\partial H}{H} - \frac{3}{2} \frac{\partial \tau}{\tau} \right) C_3} = \frac{-\frac{1}{2} \frac{\delta \tau}{H} C_1}{\left(\alpha - \frac{3}{2} \right) \frac{\delta \tau}{\tau} C_3} = \frac{-\frac{1}{2}}{\left(\alpha - \frac{3}{2} \right)} \frac{\phi_m}{\zeta}. \quad (\text{A3.7})$$

The same exercise can be done for $\frac{\partial \phi_h}{\partial \zeta}$. Using Equation (A3.5), (A3.6) and (A3.3)

we obtain:

$$\frac{\partial \phi_h}{\partial \zeta} = \frac{\left(\frac{1}{2} - \alpha \right) \frac{\delta \tau}{\tau^{1/2} H} C_2}{\left(\frac{dH}{\tau^{3/2}} - \frac{3}{2} \frac{H \delta \tau}{\tau^{5/2}} \right) C_3} = \frac{\left(\frac{1}{2} - \alpha \right) \frac{\delta \tau}{H^2} C_2}{\left(\frac{\partial H}{H} - \frac{3}{2} \frac{\partial \tau}{\tau} \right) C_3} = \frac{\left(\frac{1}{2} - \alpha \right) \frac{\delta \tau}{H^2} C_2}{\left(\alpha - \frac{3}{2} \right) \frac{\delta \tau}{\tau} C_3} = \frac{\left(\frac{1}{2} - \alpha \right)}{\left(\alpha - \frac{3}{2} \right)} \frac{\phi_h}{\zeta}. \quad (\text{A3.10})$$

4 The Scaling Behaviour of a Turbulent Kinetic Energy Closure Model for Stably Stratified Conditions*

Abstract. *We investigate the scaling behaviour of a turbulent kinetic energy (TKE) closure model for stably stratified conditions. The mixing length scale for stable stratification is proportional to the ratio of the square root of the TKE and the local Brunt-Väisälä frequency, which is a commonly applied formulation. We analyze the scaling behaviour of our model in terms of traditional Monin-Obukov Similarity Theory and local scaling. From the model equations, we derive expressions for the stable limit behaviour of the flux-gradient relations and other scaling quantities. It turns out that the scaling behaviour depends on only a few model parameters and that the results obey local scaling theory. The analytical findings are illustrated with model simulations for the second GABLS intercomparison study. We also investigate solutions for the case in which an empirical correction function is used to express the eddy-diffusivity for momentum as a function of the Richardson number (i.e. an increasing turbulent Prandtl number with stability). In this case, it seems that for certain parameter combinations the model cannot generate a steady-state solution. At the same time, its scaling behaviour becomes unrealistic. This shows that the inclusion of empirical correction functions may have large and undesired consequences for the model behaviour.*

4.1 Introduction

Turbulent motions transport momentum, heat and trace gases through the boundary layer, which forms the connection between the earth's surface and the free atmosphere. A proper modelling of these exchange processes is of vital importance for accurate Numerical Weather Prediction and climate modelling (Weng and Taylor, 2003). Despite decennia of research, modelling turbulent motions in a satisfactory way is still challenging, especially in the stable boundary layer (Holtslag, 2006). Here mechanisms like radiation divergence, slope flows, gravity waves and an increased sensitivity to surface heterogeneity generate extra complications (Mahrt et al., 1998). To account for turbulent motions, in many atmospheric models Reynolds-decomposition is applied, which involves separation of the flow into a mean part and a turbulent or subgrid part. As a result, every prognostic equation for a mean variable contains at least one unknown

* This Chapter has been published as: Baas, P., S.R. de Roode, and G. Lenderink, 2008: The scaling behaviour of a turbulent kinetic energy closure model for stably stratified conditions. *Bound.-Layer Meteor.*, **127**, 17-36.

turbulence flux term. This problem is known as the closure problem (e.g. Stull, 1988).

A commonly applied method to close the system is the eddy-diffusivity approach, where the vertical turbulent flux $\overline{w'\psi'}$ is taken proportionally to an eddy-diffusivity, K_ψ and the vertical gradient of the mean value of the variable ψ :

$$\overline{w'\psi'} = -K_\psi \frac{\partial \overline{\psi}}{\partial z}. \quad (4.1)$$

Often K_ψ is expressed as a function of stability by applying semi-empirical stability functions (e.g. Holtslag, 1998). Because only the equations for the mean variables are solved, this method is called first-order closure.

In a more advanced approach, K_ψ can be made a function of the turbulence itself. This turbulent kinetic energy (TKE) closure accounts better for the turbulent character of the flow (e.g. Basu et al., 1998) and is called 1.5-order closure. Besides prognostic equations for the mean quantities, TKE-closure models also contain a prognostic equation for TKE. In TKE- l models the eddy diffusivities depend on TKE (or E) and a diagnostic length scale, l_ψ :

$$K_\psi = l_\psi \sqrt{E}. \quad (4.2)$$

The closure problem now consists of finding appropriate expressions for the length scale. Yet, to date no consensus exists on how to model this quantity. Many different forms are proposed in literature, often based on simple physical concepts and/or ad-hoc matching arguments (Bougeault and Lacarrère, 1989; Brinkop and Roeckner, 1995; Cuxart et al., 2000; Lenderink and Holtslag, 2004, henceforth LH04).

In principle, much more complex closure models can be derived (see for an overview Weng and Taylor, 2003; Umlauf and Burchard, 2005). Relatively simple 1.5- and second-order closure models based on the work of Mellor and Yamada (1974) are frequently applied. By comparing model output with large eddy simulation data, Canuto et al. (2001) and Cheng et al. (2002) point to deficiencies of this type of models. They propose improved closure schemes by adding more advanced physics. However, even the implementation of 1.5-order or ordinary second-order closure models in NWP models is often rather complex. Practical difficulties involve the numerics (instability), constraints due to the computational costs (complexity, time step and resolution), and the requirement to have robust behaviour over the full range of atmospheric conditions (see e.g. Lenderink et al. 2004). It is therefore questionable whether more advanced physics outweighs the potentially less robustness of such complex models (Weng and Taylor, 2003).

In this study we make use of the single column version of the Regional Atmospheric Climate Model (RACMO2), in operation at KNMI (Lenderink et al., 2003). A TKE-scheme was implemented in this model, in particular to improve

the representation of cloudy boundary layers. Here we study consequences for the stable boundary layer. Recent intercomparison studies have shown that in stable conditions TKE models perform well comparable to first-order closure research models (Cuxart et al., 2006; Steeneveld et al., 2008a). However, the scaling behaviour of TKE models has received little attention in literature. For example, it is not clear to what extent such models obey well established Monin-Obukhov Similarity Theory (MOST), especially on a relatively coarse vertical grid resolution.

This study investigates the stable boundary layer scaling behaviour of a TKE- l scheme with a commonly used length-scale in terms of traditional MOST and local scaling. In particular, it is questioned whether this behaviour is realistic and to what extent it can be controlled. To put it differently, we want to establish how TKE-closure relates to the more simple first order closure. Section 4.2 provides some background on MOST and model closure. In Section 4.3 the TKE-scheme is described. Starting from the model equations, in Section 4.4 we derive expressions for the stable limit of the flux-gradient relations. Section 4.5 illustrates the analytical findings with model integrations for the second GEWEX Atmospheric Boundary Layer Studies (GABLS; Holtslag (2006)) intercomparison case. The results are compared with scaling relations obtained from observations. It will be argued that our model can be considered as a reduced version of the full second-order Nieuwstadt (1984) model. To see how the simplifications affect the model's scaling behaviour we compare some of our results with those of Nieuwstadt (1984). After discussing the results in Section 4.6, the conclusions are summarized in Section 4.7.

4.2 Background

In first order closure models, K is often expressed as (e.g. Duynkerke, 1991; Holtslag, 1998):

$$K_\psi = l^2 \left| \frac{\partial \vec{V}}{\partial z} \right| F_\psi(Ri_g). \quad (4.3)$$

Here l is a mixing length, which for example in near neutral conditions is expressed as κz . F_ψ is a correction function that accounts for effects of stratification, depending on the gradient Richardson number, Ri_g ,

$$Ri_g = \frac{\frac{g}{\theta_v} \frac{\partial \bar{\theta}_v}{\partial z}}{\left(\frac{\partial \bar{u}}{\partial z} \right)^2 + \left(\frac{\partial \bar{v}}{\partial z} \right)^2}. \quad (4.4)$$

The shape of F_ψ can be obtained by using similarity theory. We focus on the local scaling theory of Nieuwstadt (1984), which can be considered as a generalization of the surface-based MOST with local fluxes replacing surface fluxes. According to the local scaling approach, each dimensionless group is only a function of the stability parameter z/Λ ,

$$\frac{z}{\Lambda} = \zeta = \frac{-\kappa z \frac{g}{\theta_v} \overline{w' \theta'_v}}{u_*^3}, \quad (4.5)$$

where Λ is the local Obukhov-length, u_* is the friction velocity and $\overline{w' \theta'_v}$ is the virtual potential temperature flux. The dimensionless shear, ϕ_m (Eq. 4.6) and the dimensionless virtual potential temperature gradient, ϕ_h (Eq. 4.7) are defined by

$$\phi_m(\zeta) = \frac{\kappa z}{u_*} \left[\left(\partial \bar{u} / \partial z \right)^2 + \left(\partial \bar{v} / \partial z \right)^2 \right]^{1/2} \quad \text{and} \quad (4.6)$$

$$\phi_h(\zeta) = \frac{\kappa z}{\theta_*} \frac{\partial \bar{\theta}_v}{\partial z}, \quad (4.7)$$

where $\theta_* = -\overline{w' \theta'_v} / u_*$ is a turbulent temperature scale and the subscripts m and h refer to momentum and heat, respectively. The shape of these flux-gradient relations or ϕ -functions must be determined by experiment. For very strong stratification it can be argued that the size of the turbulent eddies is not related to the height above the surface anymore. Therefore, z drops as a relevant parameter for large values of z/Λ . In this stable limit of local scaling theory the dimensionless gradients become proportional to z/Λ , yielding linear ϕ -functions. This regime is called z -less scaling (Nieuwstadt, 1984). A linear interpolation between the neutral and the very stable limit gives $\phi_{m,h} = 1 + \beta_{m,h} z/\Lambda$ (Zilitinkevich and Esau, 2007).

Figure 4.1 gives some examples of flux-gradient relations that have been proposed in the literature (Businger et al., 1971; Dyer, 1974; Duynkerke, 1991; Beljaars and Holtslag, 1991 (henceforth BH91); Viterbo et al., 1999). We will compare the scaling behaviour of our model with these proposed flux-gradient functions. As will be discussed below, contrary to the other formulations, the revised Louis-Tiedke-Geleyn (rLTG) functions proposed by Viterbo et al. (1999) are not based on experimental data but on large-scale model performance.

For weakly stable conditions, when turbulence is continuous, most studies agree on the Businger-Dyer functions (Businger et al., 1971; Dyer, 1974), which state that $\phi_m = \phi_h = 1 + 5\zeta$. However, when ζ becomes larger than about one the observations start to level off and the proposed formulations diverge (see Högström, 1988; Andreas, 2002 for a review). In this regime with very strong stratification turbulence becomes patchy and intermittent (Mahrt et al., 1998), thus violating basic assumptions underlying MOST. This may explain the deviation of the ϕ -functions from the linear relation (Cheng et al., 2005). Mahrt (2007) shows

that nonstationarity promotes this levelling off of the flux-gradient relations. Note that the ϕ -functions are seriously affected by self-correlation because the occurrence of u_* in both z/L and ϕ_m and ϕ_h (e.g. Baas et al., 2006).

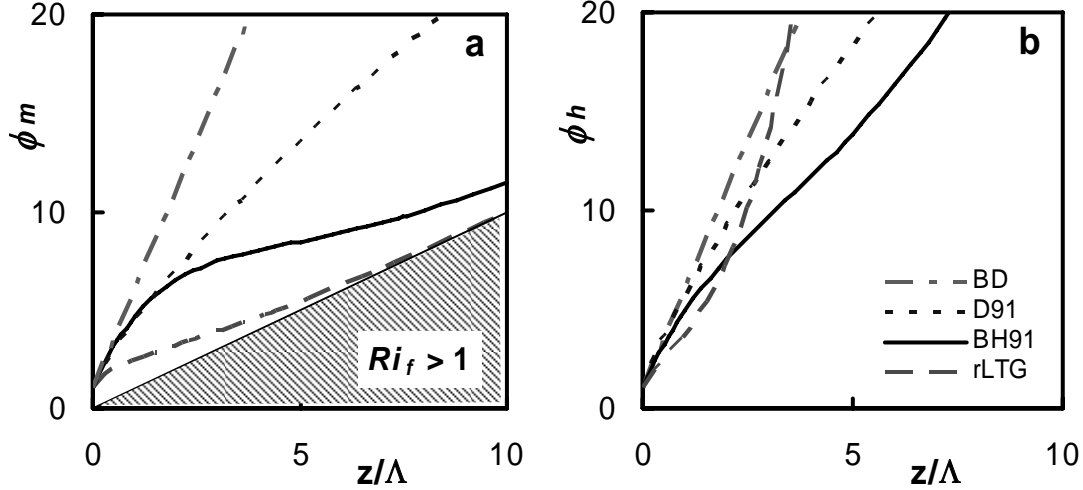


Figure 4.1: Selected flux-gradient relations for momentum (a) and heat (b) from literature. BD: Businger-Dyer; D91: Duynkerke (1991); BH91: Beljaars and Holtslag (1991); rLTG: revised Louis-Tiedtke-Geleyn, taken from Viterbo et al. (1999).

The following equations relate Ri_g and the flux-Richardson number, Ri_f (which is the ratio between the buoyancy destruction and the shear production in the TKE equation) to the flux-gradient relations (see e.g. Duynkerke and de Roode, 2001):

$$Ri_g = \zeta \frac{\phi_h}{\phi_m^2}, \quad (4.8)$$

$$Ri_f = \frac{\zeta}{\phi_m}. \quad (4.9)$$

The maximum value of Ri_f is 1, i.e. the buoyancy destruction can never be larger than the shear production. In Figure 4.1 the dashed area indicates where this theoretical demand is violated. The functions of both BH91 and rLTG approach $Ri_f=1$ in their stable limit. The turbulent Prandtl number, Pr is defined by

$$Pr = \frac{K_m}{K_h} = \frac{\phi_h}{\phi_m} = \frac{Ri_g}{Ri_f}. \quad (4.10)$$

The shape of F_ψ , where ψ indicates a certain variable, e.g. m or h , follows directly from the ϕ -functions:

$$F_\psi = \frac{1}{\phi_m(\zeta)\phi_\psi(\zeta)}. \quad (4.11)$$

By Eq. (4.8) F_ψ becomes a function of Ri_g . However, when observationally based stability functions (e.g. BH91) are applied in operational models, model performance deteriorates (Beljaars and Viterbo, 1998): night time minimum temperatures tend to be too low and mid-latitude cyclones tend to become too deep. To avoid these problems the stability functions are tuned to get optimal model performance: widely used are the rLTG functions proposed by Viterbo et al. (1999), based on work by Louis et al. (1982). It seems that large-scale models need much more mixing than can be motivated by observations from field experiments. Differences between observed mixing characteristics and the mixing which is apparently needed by operational models may be explained by surface heterogeneity (Mahrt, 1987; McCabe and Brown, 2006) and small-scale gravity wave drag (Chimonas and Nappo, 1989). Unfortunately, this so-called ‘enhanced mixing’ severely deteriorates the stable boundary layer structure. Typically the boundary layer becomes too thick and the low-level jet spread out with height (Cheinet et al., 2005; Cuxart et al., 2006). Implementing a TKE-closure scheme does not solve the problem: good operational model performance and a realistic boundary layer structure at the same time are still hard to achieve (Jones et al., 2003).

4.3 Model description

In this section we describe the vertical diffusion scheme of our model for stable stratification. Assuming horizontally homogeneous conditions, the prognostic TKE-equation (e.g. Stull, 1988) is given by:

$$\frac{\partial E}{\partial t} = -\left(\overline{u'w'}\frac{\partial \bar{u}}{\partial z} + \overline{v'w'}\frac{\partial \bar{v}}{\partial z}\right) + \frac{g}{\theta_v}\overline{w'\theta'_v} - \frac{\partial}{\partial z}(\overline{w'E} + \overline{w'p'}/\bar{\rho}) - \varepsilon. \quad (4.12)$$

The different terms on the right-hand side represent the wind shear, the buoyancy, the transport of TKE and the dissipation respectively. These terms are parameterized according to

$$-\left(\overline{u'w'}\frac{\partial \bar{u}}{\partial z} + \overline{v'w'}\frac{\partial \bar{v}}{\partial z}\right) = K_m \left[\left(\frac{\partial \bar{u}}{\partial z}\right)^2 + \left(\frac{\partial \bar{v}}{\partial z}\right)^2 \right] = K_m S^2 \quad (4.13)$$

$$\frac{g}{\theta_v}\overline{w'\theta'_v} = -K_h \frac{g}{\theta_v}\frac{\partial \bar{\theta}_v}{\partial z} = -K_h N^2$$

$$-\left(\overline{w'E} + \overline{w'p'}/\bar{\rho}\right) = 2K_m \frac{\partial E}{\partial z}$$

$$\varepsilon = c_d \frac{E^{3/2}}{l_m}.$$

Note the definitions of the Brunt-Väisälä frequency, N and the vertical wind shear, S . For stably stratified conditions, the length scale in the model is given by

$$\frac{1}{l_{m,h}} = \frac{1}{c_n \kappa z} + \frac{1}{l_s}. \quad (4.14)$$

In the limit of neutral stratification this reduces to $c_n \kappa z$. The surface boundary condition for TKE is given by

$$E_{surf} = c_0 u_*^2 + 0.2 w_*^2, \quad (4.15)$$

where $c_0 = 3.75$ (Wyngaard and Coté, 1971) is an empirical parameter and w_* is the convective velocity scale, which can be neglected in stable conditions. From a surface layer matching procedure, LH04 show that $c_d = c_o^{-2} = 0.0711$. After correcting for differences in the definition of the length scale used (most constant pre-factors), this value is equivalent to those used in for example Cuxart et al. (2000) and Brinkop and Roeckner (1995). In an analogous way Mailhot and Benoit (1982) show that the value of $c_n = 0.516$. We refer to LH04 for more details. The length scale for stable stratification (Deardorff, 1980),

$$l_s = c_{m,h} \frac{\sqrt{E}}{N}, \quad (4.16)$$

dominates in the very stable regime. The mixing efficiencies $c_{m,h}$ are model parameters which are not necessarily the same. LH04 take $c_h=0.2$ as a reference value. The parameter c_h not only regulates the vertical diffusion in the stable boundary layer, it also affects the entrainment rate (Brinkop and Roeckner, 1995; Lenderink and Holtslag, 2000). The optimal value for c_h seems to vary with boundary-layer regime (Lock and Mailhot, 2006).

With increasing stability, it is often argued that momentum is mixed more efficiently than heat, probably due to wave activity (Kondo et al., 1978; Kim and Mahrt, 1992). This process is taken into account by expressing Pr as a function of Ri_g (LH04):

$$c_m = c_h Pr = c_h (1 + c_p Ri_g). \quad (4.17)$$

Data presented by Kim and Mahrt (1992) and Schumann and Gerz (1995) suggest a value of c_p that ranges from 2 to 4. However, other studies as for example Howell and Sun (1999) do not find a clear dependency of Pr on stability. Note that spurious self-correlation stimulates a positive correlation between Pr and Ri_g , preventing examination of the physical significance of this relationship (Mahrt, 2007). In this study we vary c_p between 0 and 2. In NWP practice, the values for constants like c_p are most often based on optimal model performance rather than on sound values from the laboratory or field experiments. By expressing c_m as a function of stability, Jones et al. (2003) obtain a large reduction in the RMS and

the bias of the mean sea level pressure and the geopotential with a comparable diffusion scheme, implemented in a 3D version of the Hirlam model.

4.4 Analytical solution for the stable limit of the TKE model

We analyze the scaling behaviour of the model for very strong stratification by deriving expressions for the slope of the ϕ -functions from the model-equations. For strong stratification, the length scale is determined by l_s (Eq. 4.16). Then the eddy diffusivities can be expressed as

$$K_{m,h} = l_s \sqrt{E} = c_{m,h} \frac{E}{N}. \quad (4.18)$$

Following Eq. (4.13) the parameterized TKE-equation becomes

$$\frac{\partial E}{\partial t} = K_m S^2 - K_h N^2 - c_d \frac{E^{\frac{3}{2}}}{l_m}. \quad (4.19)$$

In this analytical analysis, we neglect the transport term for simplicity. In Section 4.5, we compare the analytical results with numerical simulations of the TKE model using the complete set of equations. The output shows that for stable conditions the transport term is indeed very small in the model, which justifies this assumption in the context of our model. Although in reality the transport term is generally small in the SBL (e.g. Nieuwstadt, 1984), under certain conditions (e.g. intermittency) it can be considerable (Cuxart et al., 2002).

After filling in the eddy-diffusivities (Eq. 4.18), the length scale (Eq. 4.16) and using Eqs. (4.9), (4.10) and (4.17), Eq. (4.19) can be written as

$$\frac{\partial E}{\partial t} = c_h EN \left[\frac{c_m}{c_h} \frac{1}{Ri_g} - \left(1 + \frac{c_d}{c_m c_h} \right) \right] = c_h EN \left[\frac{\phi_m}{\zeta} - \left(1 + \frac{c_d}{c_m c_h} \right) \right]. \quad (4.20)$$

In Section 4.4.1 we consider the situation where Pr is constant. Next we study the consequences of an increasing Pr with stability in Section 4.4.2. Section 4.4.3 discusses some complications that arise with the current stability dependency of Pr .

4.4.1 Pr is constant

Assuming stationary state, Eq. (4.20) leads to a simple expression for the slope of the ϕ -functions which only depends on model parameters. In the case that c_m and c_h are constants it follows that

$$\frac{\phi_m}{\zeta} = 1 + \frac{c_d}{c_m c_h} \quad \text{and} \quad (4.21)$$

$$\frac{\phi_h}{\zeta} = \frac{c_m}{c_h} \frac{\phi_m}{\zeta} = \frac{c_m}{c_h} + \frac{c_d}{c_h^2}. \quad (4.22)$$

Since this equilibrium (stable limit) solution contains just model constants it states that ϕ_m becomes linear with ζ , which agrees with the asymptotic limit of local scaling theory (z -less scaling). Using Eq. (4.8), the corresponding critical Ri_g can be expressed as

$$Ri_{g,cr} = \frac{1}{\frac{c_h}{c_m} + \frac{c_d}{c_m^2}}. \quad (4.23)$$

For example, if we set $c_m = c_h = 0.13$ we obtain $\phi_m = \phi_h = 5\zeta$, which is the stable limit of the Businger-Dyer relations. The corresponding critical $Ri_g = 0.2$.

It should be noted that the concept of a critical Ri_g (which was often assumed to be about 0.25) is debatable. Numerous experimental studies show turbulent activity at values of $Ri_g > 1$ (e.g. Kondo et al., 1978; Kim and Mahrt, 1992; Zilitinkevich et al., 2007). Rather than having a strict critical Ri_g above which a flow is always laminar, a *transition regime* can be identified separating a weakly stable ($Ri_g < O(0.1)$) and a very stable regime ($Ri_g > O(1)$) (Mauritsen and Svensson, 2007). In the former regime turbulence is strong and MOST can be applied, contrary to the latter regime where turbulent motions *do* exist but are weak and non-stationary (Mahrt et al., 1988). Bertin et al. (1997) suggest that Ri_f rather than Ri_g is the relevant parameter for defining the eddy diffusivity.

4.4.2 Pr increases with stability

To allow for an increasing Pr with stability, we take into account Eq. (4.17). By using Eq. (4.10) we can express c_m (which is not a constant anymore now) as

$$c_m = c_h \left(1 + c_p Ri_g\right) = c_h \left(1 + c_p \frac{c_m}{c_h} Ri_f\right). \quad (4.24)$$

Solving for c_m (and using Eq. 4.9) gives this parameter in terms of model constants and ϕ_m/ζ :

$$c_m = \frac{c_h}{\left(1 - c_p \frac{\zeta}{\phi_m}\right)}. \quad (4.25)$$

Combining Eqs. (4.21) and (4.25) leads to a quadratic equation, with solutions

$$\frac{\phi_m}{\zeta} = \frac{1}{2} \left(1 + \frac{c_d}{c_h^2}\right) \pm \frac{1}{2} \sqrt{\left(1 + \frac{c_d}{c_h^2}\right)^2 - 4c_p \frac{c_d}{c_h^2}}. \quad (4.26)$$

Eq. (4.26) gives the slope of $\phi_m(\zeta)$ in the stable limit as only a function of c_h and c_p . For ϕ_h it can be shown that

$$\frac{\phi_h}{\zeta} = \frac{c_m}{c_h} \frac{\phi_m}{\zeta} = \frac{c_d}{c_h^2} + \frac{1}{\left(1 - c_p \frac{\zeta}{\phi_m}\right)}. \quad (4.27)$$

Eqs. (4.26) and (4.27) reduce to Eqs. (4.21) and (4.22) for $c_p = 0$, providing that $c_m = c_h$. The ‘minus-solution’ in Eq. (4.26) is never followed by the model and has no physical meaning since it causes $\phi_h/\zeta < 0$ (in most cases), i.e. it requires an unstable stratification in the considered stable limit. Therefore in the following we focus on the ‘plus-solutions’ of Eqs. (4.26) and (4.27).

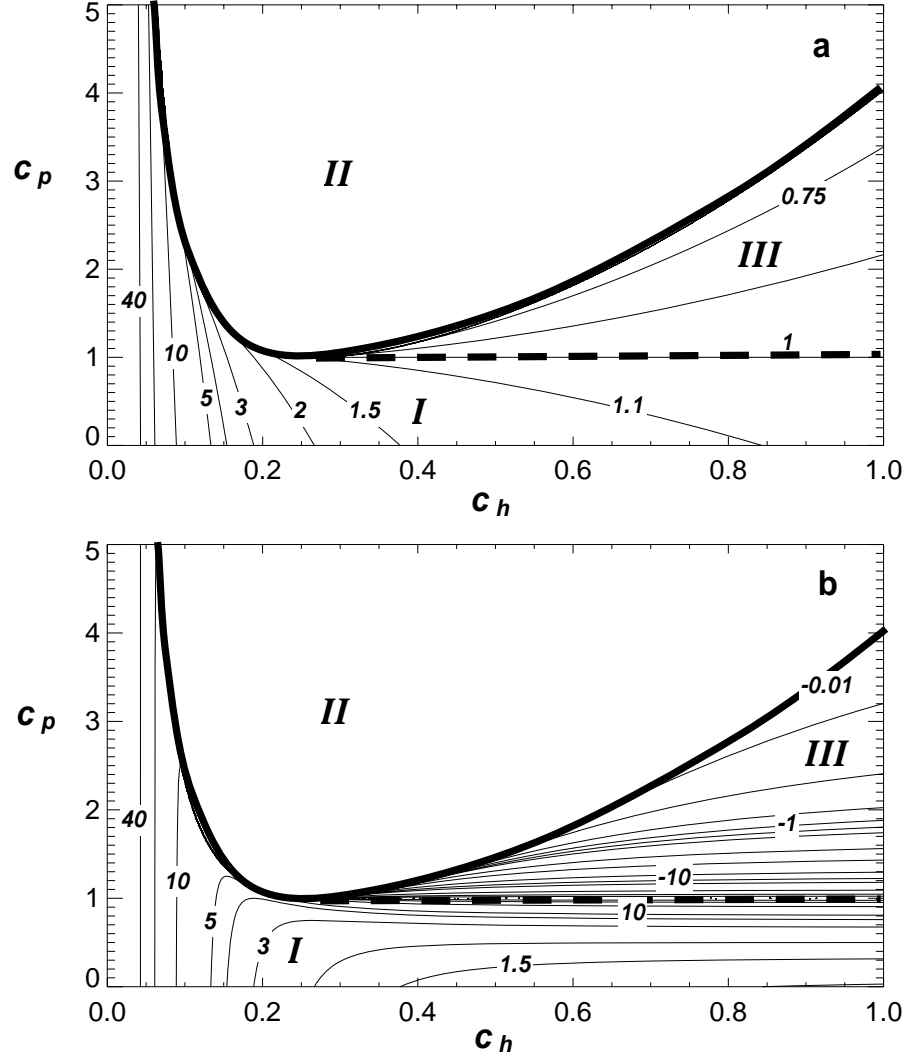


Figure 4.2: Contour plots of ϕ_m/ζ (a) and ϕ_h/ζ (b) as a function of c_h and c_p following the ‘plus-solutions’ of Eqs. (4.26) and (4.27), which indicate the slope of the ϕ -functions in the stable limit. In regime I the model obeys local scaling theory. Regime II indicates parameter combinations where no stable limit solution exists. The solutions in regime III have no physical meaning since values for ϕ_h/ζ are negative and $\phi_m/\zeta < 1$ ($Ri_f > 1$).

Figure 4.2 presents lines of equal ϕ_m/ζ and ϕ_h/ζ as a function of c_h and c_p . Regime *I* indicates the parameter space where the model obeys local scaling theory. In regimes *II* and *III* this is not the case: these situations correspond to parameter combinations for which no steady state solution exists or which do not have a physical meaning. These last two regimes are discussed in the next subsection.

4.4.3 Comments on the current formulation of Pr versus stability

Due to the dependency of c_m on ϕ_m/ζ itself, the equation for ϕ_m/ζ (Eq. 4.26) becomes quadratic. Consequently the solution of this equation contains a square root, which can become negative for certain combinations of c_h and c_p . It turns out that the system only has a real solution for

$$c_p \leq \frac{1}{2} + \frac{c_d}{4c_h^2} + \frac{c_h^2}{4c_d}. \quad (4.28)$$

This is indicated in Figure 4.2, which separates the real and imaginary solutions of Eq. (4.25): apparently, in regime *II* a strictly stable limit solution does not exist.

To get more insight in why a parameter range without real solution exists, we further analyze the stable limit of the TKE-equation. By filling in Eq. (4.18) for the eddy-diffusivities and Eq. (4.17) for c_m , the stationary TKE-equation (4.19) can be written as

$$\left[1 + c_p \frac{N^2}{S^2}\right] c_h S^2 - c_h N^2 - \frac{c_d}{c_h} \frac{N^2}{\left[1 + c_p \frac{N^2}{S^2}\right]} = 0. \quad (4.29)$$

For increasing c_p the buoyancy term is unaffected but the shear term becomes larger and the dissipation becomes smaller. It turns out that when c_p exceeds the threshold value imposed by Eq. (4.28), the shear term becomes *so* large that the buoyancy destruction and the dissipation cannot balance the shear production anymore, indicating that a steady-state solution is no longer possible and $\partial E/\partial t > 0$. Note that the extra shear production scales with the buoyancy destruction. For $c_p = 1$ the buoyancy destruction is fully compensated by the extra shear production and ‘vanishes’.

A second problem, raised by Eq. (4.27), is that the value of ϕ_h/ζ might become negative. This turns out to be the case in regime *III* of Figure 4.2, when $c_h > 0.26$ and $c_p > 1$. Note that $\phi_m/\zeta < 1$ in this regime, corresponding to the unphysical $Ri_f > 1$. Eq. (4.29) can be expressed as a quadratic equation in Ri_g . Solving gives an expression for the critical Ri_g as a function of only c_h and c_p :

$$Ri_g = -\frac{2c_p - 1 - \frac{c_d}{c_h^2}}{2c_p(c_p - 1)} \pm \frac{1}{2c_p(c_p - 1)} \sqrt{\left(1 + \frac{c_d}{c_h^2}\right)^2 - 4c_p \frac{c_d}{c_h^2}}. \quad (4.30)$$

Only the ‘minus-solution’ gives realistic values. In case of $c_p = 0$, Eq. (4.29) simply reduces to Eq. (4.23). Also for $c_p = 1$, Eq. (4.29) reduces to a linear equation. Values for the critical Ri_g can be obtained by taking the limit of $c_p \rightarrow 1$ in Eq. (4.30) as well.

4.5 Comparison of the analytical solutions with model simulations of the TKE model

We compare the analytical solutions for the stable limit (obtained in Section 4.4) with model simulations of the full TKE model (Section 4.3) for the second GABLS intercomparison study (Svensson and Holtslag, 2006). This case is based on observations from the CASES-99 measurement campaign (Poulos et al., 2002), which was organized in October 1999 in Kansas, U.S.A (37.65°N, 96.74°W; ~ 440 m a.s.l.). A constant geostrophic forcing is applied and the surface temperature is prescribed as a function of time. The simulation time is 59 hours, starting at 14:00 local time and we use a high vertical resolution of about 5 m. The time-step is 300 seconds. For our analysis we only use model output from the lowest 40 levels, i.e. below 200 m. Because it is often argued that the results of TKE models depend relatively strongly on vertical resolution we also performed some runs on low resolution. When the number of levels is reduced to 60 (one level about each 40 m close to the surface) exactly the same scaling results are obtained, indication that the conclusions are also applicable for operational resolutions. Also the vertical wind profiles of the low resolution runs give similar results as the ones with high resolution. We stress that we focus on the scaling behaviour of the model and not on simulating the observations. For such a study we refer to Steeneveld et al. (2006) who analyzed almost the same period in great detail.

Table 4.1: Characteristics of the four model runs.

	c_h	c_p	remarks
A	0.13	0	No Pr dependency; $\phi_m = \phi_h = 5\zeta$ in the stable limit
B	0.13	1	$\text{Pr} = 1 + Ri_g$
C	0.2	1	Current operational values
D	0.2	2	No analytical solution

The TKE model is run with four different combinations of c_h and c_p as defined in Table 4.1. For c_h the value of 0.13 was chosen because this predicts $\phi_{m,h} = 5\zeta$ for $c_p = 0$ in the stable limit. The current operational value for c_h is 0.2. For Case D no analytical stable limit solution exists. From the model output we will diagnose flux-gradient relations (and stability functions) and compare the scaling behaviour of our model with the more advanced model of Nieuwstadt (1984). Finally, some quantities related to the boundary layer structure will be investigated. Table 4.2 summarizes the obtained stable limit solutions.

Table 4.2: Stable limit solutions for the model runs A, B and C defined in Table 4.1. Case D has no analytical solution. For comparison values for the N84 models are added.

	A	B	C	N84
ϕ_m/ζ	5.0	4.0	1.8	
ϕ_h/ζ	5.0	5.4	4.1	
Ri_g	0.20	0.33	1.29	0.218
$(2E)^{1/2} / u_*$	2.59	2.54	2.23	2.8
$K_m / (L u_*)$	0.08	0.10	0.22	0.08
$K_h / (L u_*)$	0.08	0.07	0.10	0.08

4.5.1 Flux-gradient relations

Figure 4.3 shows flux-gradient relations for the four different combinations of c_h and c_p defined in Table 4.1. Apart from case D, for which no analytical solution exists, in all cases the ϕ -functions approach to the predicted stable limit (Table 4.2). For increasing c_h the ϕ -functions become less steep, increasing c_p causes ϕ_m and ϕ_h to diverge. Obviously, for a near neutral stratification the ϕ -functions deviate from the stable limit solution and the neutral length scale forces them to be 1. When ζ becomes larger than about 1.5, the influence of the neutral length scale becomes very small.

A comparison with ϕ -functions from the literature (see Figure 4.1) shows that for $\zeta < 1$ the observations correspond best with cases A and B. However, experimentally obtained flux-gradient relations tend to level off for larger stabilities as for example the D91 and the BH91 functions (Figure 4.1). Consequently, for increasing ζ the cases A and B deviate from observed values. When stratification is very strong, case C is closest to the observations.

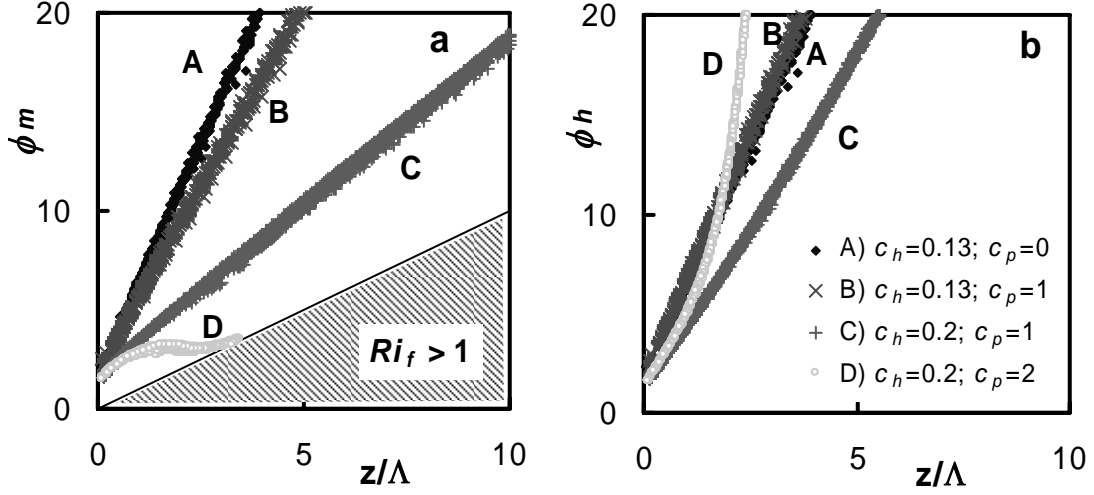


Figure 4.3: Flux-gradient relationships for momentum (a) and heat (b) as diagnosed from model output for four different combinations of c_h and c_p .

For case D no analytical stable limit solution exists. Figure 4.3 shows that in this case ϕ_m increases only very slowly and that the increase in ϕ_h is more than linear with stability, which does not agree with observations. Surprisingly, comparison with Figure 4.1 shows that this behaviour is well comparable to the rLTG functions. In fact, from Eqs. (4.9) and (4.10) it can be shown that a more than linear increase of $\phi_h(\zeta)$ is inevitable when one wants to fulfil $Ri_f < 1$ and at the same time let $Ri_g \rightarrow \infty$ in the stable limit.

4.5.2 Stability functions

Stability functions for momentum and heat are given in Figure 4.4. The model runs with low c_h (0.13) have a low critical Ri_g , above which all turbulence is switched off. They are well comparable with the BH91 functions, in the sense that mixing decreases rapidly with increasing Ri_g . Note that the BH91 functions were formulated in such a way that no critical Ri_g exists. For case C mixing is suppressed more slowly, but still a critical Ri_g exists at about 1.3. The fact that for case D no stable limit solution exists, involves that also a critical Ri_g is lacking. The stability functions for this case are comparable with the rLTG-functions, thus showing characteristics of ‘enhanced mixing’. As such, case D is not expected to give realistic results in terms of stable boundary layer structure.

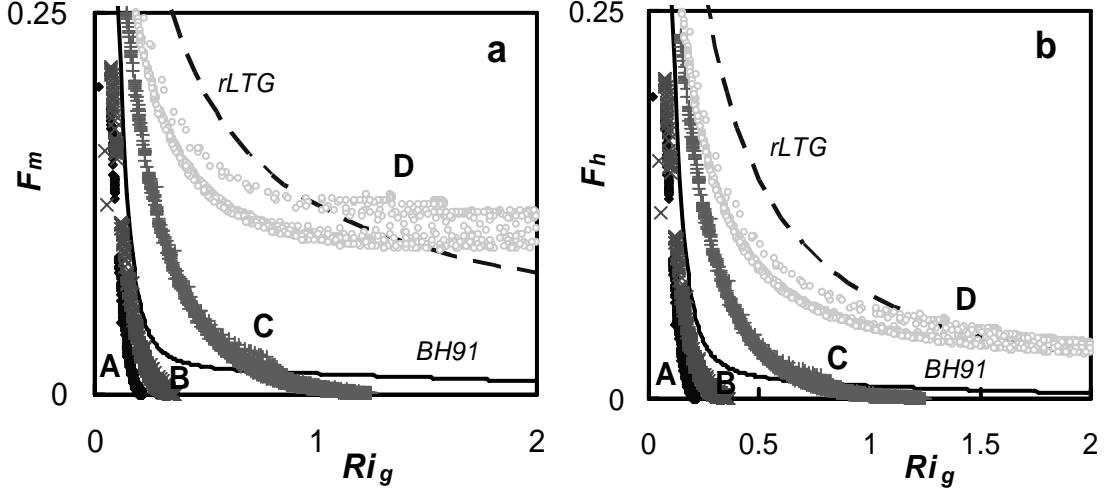


Figure 4.4: Stability functions for momentum (a) and heat (b) for the different model simulations A-D defined in Table 4.1. For comparison two proposals from literature are added: the dashed line represents the revised LTG functions, the solid line the Beljaars-Holtlag (1991) functions.

4.5.3 Comparison with the Nieuwstadt (1984) (N84) model

In this Section we will compare the scaling behaviour of our model with the N84 model, which is a full second-order model. N84 applies a slightly different formulation for the stable length scale; instead of $E^{1/2}$ as in our model the standard deviation of the vertical velocity fluctuation, σ_w is used:

$$l_B = C_B \frac{\sigma_w}{N} \text{ (N84, his Eq. (20))}, \quad (4.31)$$

where $C_B = 1.69$ is a constant. According to his Figures 2 and 3, σ_w and $E^{1/2}$ (both scaled by u_*) are almost constant as a function of ζ . This means that σ_w is a fixed fraction of $E^{1/2}$, which implies that the length scales in the two models are equivalent. In fact, for stable conditions our TKE scheme can be considered a reduced version of the N84 model. By reproducing some figures from N84 we will now compare the scaling behaviour of the two models to see how this behaviour is affected by the simplifications in the TKE-closure approach. The theory of local scaling predicts that dimensionless quantities reach a constant value in the stable limit (N84). In the following figures and in Table 4.2 the limit of the N84 is given together with the model results for the four runs described above.

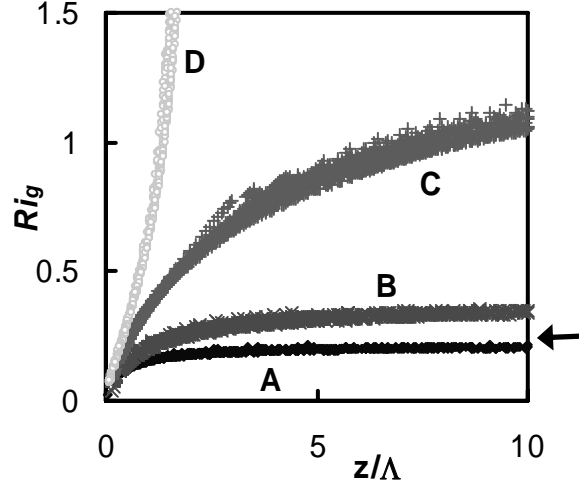


Figure 4.5: Ri_g vs. z/Λ for the different model simulations A-D defined in Table 4.1. The stable limit solutions for each case are given in Table 4.2. The arrow indicates the limit solution of the N84 model.

Figure 4.5 (N84, Figure 9) gives the results for Ri_g versus z/Λ . It illustrates that case D does not have a critical Ri_g , thus violating the theory of local scaling. The other three model runs approach their critical value as predicted by Eq. (4.30). In the stable limit, Case A) is very close to the N84 solution.

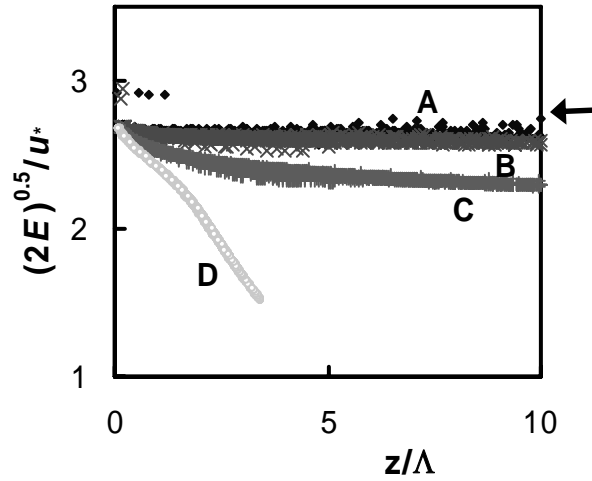


Figure 4.6: TKE, nondimensionalized with u_* for the different model simulations A-D defined in Table 4.1. The stable limit solutions for each case are given in Table 4.2. The arrow indicates the limit solution of the N84 model.

The same pattern can be seen in Figure 4.6, where the TKE, nondimensionalized by u_* , is plotted versus stability. Values are constant over the

whole stable range. This implies that the shear stress is proportional to the TKE everywhere in the stable boundary layer, which is not surprising since in stable conditions shear is the only source of turbulence (N84). The larger c_p , the lower the equilibrium value that is obtained. Case D does not reach equilibrium. Stable limit solutions can be calculated according to

$$\frac{\sqrt{2E}}{u_*} = \frac{\sqrt{2} Ri_g^{0.25}}{\sqrt{c_h(1 + c_p Ri_g)}}, \quad (4.32)$$

which follows directly from $u_*^2 = K_m S = c_h(1 + c_p Ri_g) EN^{-1} S$. For Ri_g Eq. (4.30) can be filled in.

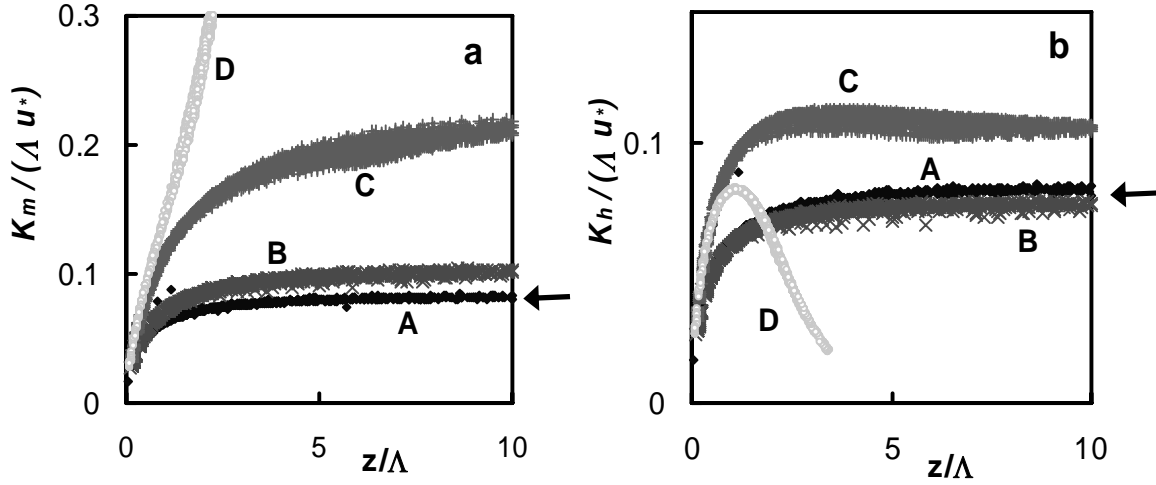


Figure 4.7: K_m (a) and K_h (b), both nondimensionalized with (Λu_*) for the different model simulations A-D defined in Table 4.1. The stable limit solutions for each case are given in Table 4.2. The arrow indicates the limit solution of the N84 model. Note the difference in scale on the y-axis.

The scaled eddy-diffusivities are given in Figure 4.7. Except for Case D, all curves show a gradual increase from zero in neutral conditions to a constant value in the stable limit. The N84 stable limit compares well to our cases A and B. The stable limit solutions can be obtained by

$$\frac{K_m}{Lu_*} = \frac{k Ri_g}{Pr} = k \frac{\zeta}{\phi_m} \quad \text{and} \quad (4.33)$$

$$\frac{K_h}{Lu_*} = \frac{k Ri_g}{Pr^2} = k \frac{\zeta}{\phi_h}, \quad (4.34)$$

and filling in Eqs. (4.26) and (4.27).

Thus the TKE- l model generates a scaling behaviour comparable to the more advanced N84 model. The stable limits of the N84 model show most agreement with our Case A, which has a relatively low value of c_h and has $c_p = 0$.

4.5.4 Boundary layer structure

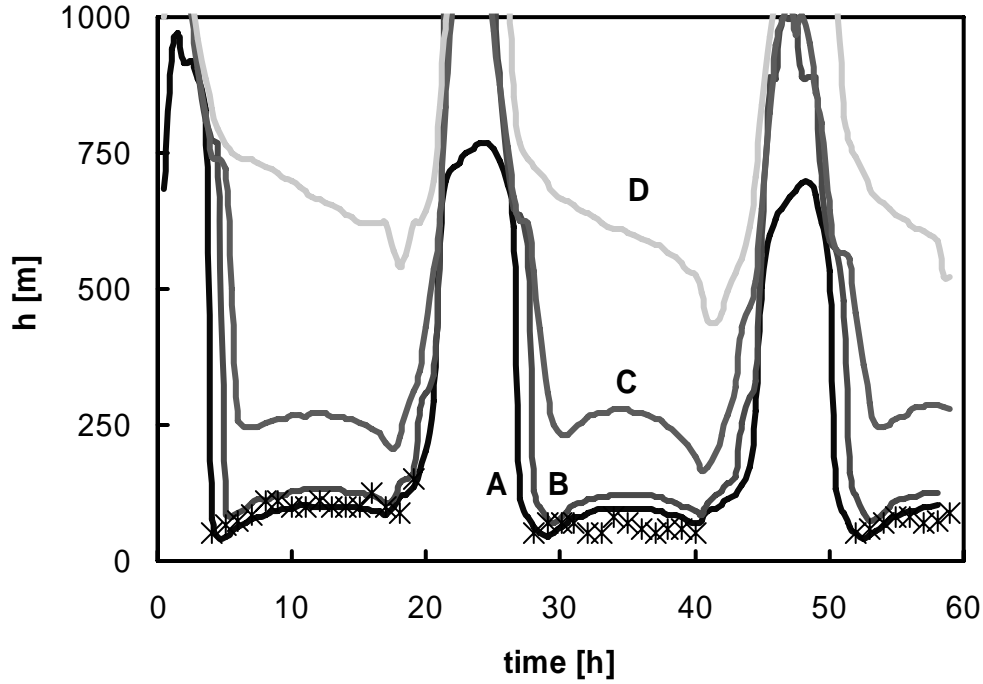


Figure 4.8: Time-series of boundary layer heights, h , for the model runs A-D. Crosses indicate sodar retrievals made during the CASES-99 campaign.

So far we have only discussed the scaling behaviour of the model. To give an impression on how the different model runs represent the boundary layer structure, we will now discuss the boundary layer height (Figure 4.8) and the vertical profiles of the wind speed (Figure 4.9). The boundary layer height, h , is defined as the level where the TKE has dropped to 5% of its surface value, divided by 0.95 (as in Cuxart et al., 2006). Model runs A and B produce very shallow boundary layers of less than 100 m during night time, combined with a distinct low-level jet. This is in good agreement with sodar retrievals obtained during the CASES-99 campaign. The difference between cases B and C demonstrates the impact of increasing c_h from 0.13 to 0.2: h becomes too large compared to observations and the low-level jet becomes much weaker. In case D, h is far too large and the low-level jet has disappeared. These results are consistent with our earlier finding that case D shows Louis type of stability functions. The corresponding deterioration of the boundary layer structure is a logical consequence.

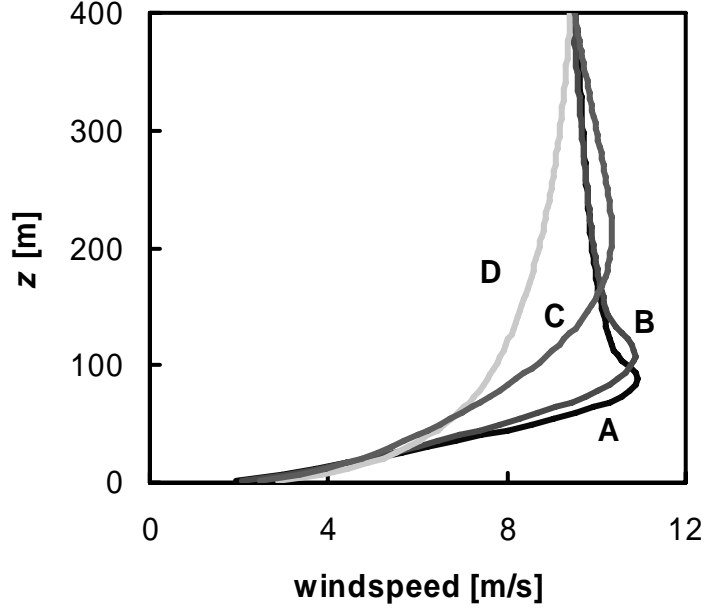


Figure 4.9: Vertical wind profiles at 38 hours of simulation (halfway the second night). Letters indicate the model runs A-D.

4.6 Discussion

Our TKE-scheme follows the local scaling hypotheses: for $z/\Lambda \rightarrow \infty$ dimensionless quantities reach a constant value and the ϕ -functions become linear (z -less scaling). The latter is a direct consequence of Ri_f and Ri_g becoming constant. However, as mentioned in Section 4.2, data from experiments show that the ϕ -functions level-off for large stabilities. In this Section we discuss this discrepancy. We further noticed that the ‘imaginary’ case D shows erratic scaling behaviour. Here we discuss how to interpret these results.

To confirm that our results do not depend on boundary conditions we did some sensitivity runs with half the geostrophic forcing and an unrealistic step-wise surface temperature forcing (one temperature at night (4°C), one during daytime (14°C)). For the different cases we obtained similar results as before (not shown). Apparently, changing the boundary conditions does not influence the scaling behaviour of the scheme, which indicates that this is robust and depends only on model parameters.

4.6.1 The validity of the local scaling hypotheses

For continuous turbulence the critical Ri_f is about 0.2 (Beljaars and Holtslag, 1991; N84), which is consistent with the relation $\phi_m = 1 + 5\zeta$. However, when stability becomes so large that turbulence gets intermittent, Ri_f can be larger (Kondo et al.,

1978). Assuming that $\phi_m = 1 + 5\zeta$ is valid for about $\zeta < 1$, this implies a levelling off of ϕ_m for larger stabilities. In these conditions the local scaling hypothesis is not valid anymore. Basu et al. (2006) confirm this by showing that mesoscale motions and intermittent turbulence can invalidate local scaling. Mahrt et al. (1998) state that local scaling does not work for $\zeta > 1$, which they define as the very stable regime. In fact, this may even explain the difference between the flux-gradient relations found by BH91 and D91 (Figure 4.1). The D91 functions were based on data of N84 who selected only data with a wind speed of more than 5 m s^{-1} to avoid intermittent turbulence as much as possible. Consequently, the D91 functions level off much slower than the BH91 functions that do not make this selection. Since our TKE scheme strictly follows local scaling theory it is not surprising that the model does not reproduce the levelling off of the flux-gradient relations for large ζ . From a practical point of view it may be questioned whether this levelling off effect is important, because for such strongly stable conditions turbulent fluxes are very small anyway and radiative processes may dominate the energy balance (André and Mahrt, 1982). In addition, the results for the GABLS case are good when using parameter setting A and B, whereas they get worse using the enhanced mixing in case C and D. This indicates that a realistic behaviour of the ϕ -functions for $\zeta < 1$ is crucial.

4.6.2 Understanding the output of case D

In Section 4.4 we concluded that for certain combinations of c_h and c_p no stationary solution is possible. By running the model with such a ‘forbidden’ combination we found that the scaling behaviour of the model becomes unrealistic as in case D. Even under these conditions model output shows that the transport of TKE plays a minor role. In this case the equations prohibit the model to reach a steady state. Instead, E grows every time-step and so do l_m , R_{ig} and K_m . This process continues until l_m becomes limited by its neutral part (see Eq. 4.14). Alternatively, c_m can be maximized artificially by e.g. $c_m = c_h[\max(1+2R_{ig}, 4)]$. In this case the stable limits can be easily calculated by filling in c_h and $c_m = 4c_h$ in Eqs. (4.21) and (4.22). Of course other dependencies of c_m on c_h can be tested as was done by Tijn (2004) for example.

As shown in Section 4.5, results for case D seem to represent rLTG type of diffusion. Therefore, it might be tempting to apply comparable parameter settings if implementation of TKE-closure with strong diffusion is desirable. However, we do not recommend this. In our opinion introducing more advanced physics (in this case TKE-closure) should not go together with deliberately keeping the mixing under stably stratified conditions unrealistically high in order to get other aspects of the model right (e.g. the large scale atmospheric dynamics). Instead, implementation of TKE-closure in operational models should lead to a more

realistic SBL structure, suggesting a value for c_h of about 0.13 and a rather small value of c_p . Matching the observed mixing characteristics in the SBL with the highly diffusive boundary layers apparently needed in NWP models needs clearly more research.

4.7 Conclusions

TKE turbulence closure is more and more applied in research models, but most large scale operational models still apply first-order closure. One of the reasons is that uncertainties exist in the scaling behaviour of TKE models and that it is questioned whether this behaviour can be controlled.

We studied the scaling behaviour of a TKE model for stably stratified conditions. The length scale for stable conditions is proportional to the ratio of the square root of the TKE and the local Brunt-Väisälä frequency, which is a commonly used formulation (Deardorff, 1980). The scaling behaviour of the model for stably stratified conditions is controlled by the constants of proportionality preceding this ratio. Motivated by observations and 3D model performance, the turbulent Prandtl number can be expressed as a function of stability. As a prototype we used $Pr = 1 + c_p Ri_g$. From the model equations we analyzed expressions for the stable limit of various scaling quantities like the flux-gradient relations.

Obviously, the generality of our results can be questioned, since we investigate only a single model. However, we note that the Deardorff length scale is a rather common formulation in TKE closures, and that some other proposals (e.g. the parcel method developed by Bougeault and Lacarrère (1989)) reduce to the Deardorff length scale in stable conditions as well. We believe that our results have a general applicability for those models. We also acknowledge that they are not generally valid for all other length scale proposals in literature, but our results may stimulate to perform similar analysis for those schemes. The current function which allows Pr to vary with stability is less frequently applied. Yet, our results show that the inclusion of such an empirical correction function may have large and undesired consequences for the model behaviour (in our case inability to obtain a steady state with the Deardorff length scale, and drift to a state which is dominated by the limiting neutral length scale).

Depending on parameter choice, different regimes can be distinguished in the scaling behaviour of our model. In the first regime the model follows the local scaling theory of Nieuwstadt (1984), which can be considered as an extension of the surface based Monin-Obukhov Similarity Theory: in the stable limit dimensionless parameters become constant and the flux-gradient relations become linear (z -less scaling). However, most observational studies show the flux-gradient

relations to level off for very strong stratification. This is probably due to the fact that under these conditions turbulence loses its continuous character, thereby violating basic assumptions underlying the theory of local scaling.

In the second regime the scaling behaviour of the model becomes unrealistic and violates local scaling theory. This occurs when, depending on the mixing efficiency for heat, c_p is taken larger than a certain threshold value. In this regime, no stationary solution of the TKE-equation is possible: the shear production becomes so large that the buoyancy destruction and the dissipation cannot balance the TKE-equation anymore. Surprisingly, the stability functions now resemble the formulations which are currently used by large scale operational models as e.g. the Louis functions of the ECMWF model. We do not recommend implementing this kind of enhanced mixing in a TKE-closure model. In our opinion the introduction of a TKE-scheme should aim to realistic mixing characteristics leading to a more accurate representation of the SBL structure.

The analytical results were illustrated by four model simulations with different mixing characteristics. Sensitivity runs were done to investigate whether the obtained scaling behaviour was not just an artefact of the selected case-study or the model details. It turned out that changing the boundary conditions and the vertical resolution did not affect the scaling results. The correspondence between our results and those of the full second order model of Nieuwstadt (1984) model is good. This shows that simplifications made in the TKE-closure approach have little impact for the stable boundary layer scaling behaviour.

Acknowledgements

We acknowledge Bert Holtslag and Gert-Jan Steeneveld from Wageningen University as well as three anonymous reviewers for their valuable comments on the manuscript. The first author has been supported by the Netherlands Organization for Scientific Research (NWO), in particular through the project “land surface climate and the role of the stable boundary layer”. In addition part of this research was carried out in the framework of the Dutch National Research Program “climate changes spatial planning” (www.klimaatvoorruimte.nl).

5 How to Design Single-Column Model Experiments for Comparison with Observed Nocturnal Low-Level Jets*

Abstract. *Single-column models (SCMs) are widely employed to evaluate boundary layer parameterizations under well controlled conditions. To compare SCM results to observations, these models must be driven by realistic forcings of the 3D atmospheric state. However, these forcings are inherently uncertain. The central research question is therefore: can observations be used to distinguish between different parameterization schemes in SCM simulations or is the spread due to uncertainties in the forcings too large? This study investigates this question for the nocturnal low-level jet (LLJ) at Cabauw. First, we analyse a single LLJ case that has been used for the third GEWEX Atmospheric Boundary Layer Studies (GABLS3) intercomparison study. To estimate the forcings, for this case a blend of local observations and 3D model output has been used. A sensitivity study to both the forcings and the turbulence formulation is performed by using the SCM version of the ECMWF model. The sensitivity to the turbulence parameterization is largest in the bulk of the stable boundary layer (SBL). The influence of the forcings manifests itself mainly in the upper part of the SBL and above. Second, an ensemble of comparable LLJ cases is considered. Using forcings derived from 3D models, SCM results of the separate cases show significant deviations from the observations. However, the mean of the SCM simulations agrees well with the mean of the observations. Considering multiple cases improves the signal-to-noise ratio, which enables a better judgement of the quality of boundary layer parameterizations in a comparison with the observations.*

5.1 Introduction

Single Column Models (SCMs) are powerful tools to test different parameterization schemes without the interference with the atmospheric three dimensional dynamics. In the last years, many SCM (intercomparison) studies of the stable and unstable boundary layer have been carried out (e.g. Sharan and Gopalakrishnan, 1996; Duynkerke et al., 1999; Duynkerke et al., 2004; Lenderink et al., 2004; Cuxart et al., 2006; Steeneveld et al., 2006; Svensson and Holtslag, 2006; Edwards et al., 2006). This has led to improved parameterizations of the atmospheric boundary layer (e.g. Lenderink and Holtslag, 2004; Mauritsen et al., 2007; Neggers et al., 2008). However, most of these studies are to a large extent

* This Chapter is based on a revised manuscript for *Q. J. Roy. Meteor. Soc.*, with F. C. Bosveld, G. Lenderink, E. van Meijgaard, and A. A. M. Holtslag as co-authors.

idealized using simplified prescriptions of the forcings. This complicates a comparison with the observations. In the last years, there is a trend to built SCM cases with more realistic forcings, which enables a better comparison with the observations (Baas et al., 2008b; Kumar et al., 2009; van Zanten et al., 2009). This improves the ability to assess the quality of the parameterizations.

It is not trivial how to describe the forcings for a SCM. Necessarily, these forcings consist of the geostrophic forcing (i.e. the pressure gradient), the (horizontal) advective tendencies, and the vertical velocity. Depending on the case studied, radiative tendencies or surface boundary conditions (e.g. surface fluxes or surface temperature) may be prescribed additionally. Direct measurements of these forcings do in general not exist. To obtain an independent estimate of the forcings, SCM studies and intercomparison cases often use a blend of observations and 3D model results.

Physical constraints and/or simple conceptual models are often employed to adjust the forcings to obtain a realistic time evolution of the atmospheric variables in SCM runs. For example, the subsidence rate is chosen in such a way that the boundary layer height is represented correctly (Ek and Holtslag, 2004; Lenderink and Siebesma 2004). In the case study presented here, the nocturnal advective tendency of momentum is estimated by assuming that during night time the wind speed at 200 m is not influenced by frictional forces. Consequently, the advection can be estimated by taking the difference between the observed wind and a freely evolving inertial oscillation. Cassa-Torralba et al. (2008) demonstrate how advective tendencies can be estimated during daytime by using turbulent flux observations.

The way the lower boundary conditions should be prescribed is a matter of debate, as well. For example, whether surface fluxes or a surface temperature is prescribed can make a large difference in the evolution of the boundary layer and the sensitivity of SCM results to different turbulence closures (Basu et al., 2008). Recent research shows that in stable conditions coupling of the boundary-layer scheme to the land-surface scheme has a clear impact on the model results. This is due to non-linear feedbacks in which the magnitude of the geostrophic wind and the surface temperature play an important role (Holtslag et al., 2007).

Summarizing, we argue that SCM (intercomparison) studies are mostly inspired by observations, but ‘in the end’ to some extent also adjusted to get a realistic (close to observed) time evolution. The uncertainty or even ambiguity in the forcings hampers a comparison with observational data. A natural question is therefore: to what extent can observational data be used to distinguish between different parameterization schemes given the uncertainties in the large-scale forcings?

This study aims to assess the influence of the large-scale forcings on SCM studies of the nocturnal low-level jet (LLJ). Besides, we explore the potential for setting up a SCM study based on an ensemble of comparable cases. As a case study, we select a fair-weather LLJ case observed at the measurement site of Cabauw, the Netherlands. This case is used for the third GEWEX Atmospheric Boundary Layer Studies (GABLS3) intercomparison study. We focus on the evolution of the wind since this appears often a difficult variable to predict (e.g. Svensson and Holtslag, 2006). A correct representation of the nocturnal LLJ is important for, amongst others, the transport of pollutants, aviation, and wind energy applications. Extra wind shear below the LLJ may influence the turbulent structure of the SBL. We take the GABLS3 case set-up as a reference. First the sensitivity of the GABLS3 case set-up to the turbulent closure is analysed. Then we modify the forcings to get insight in the extent they determine the SCM solution. We discuss how the resulting spread in model results compares to the impact of different parameterization schemes.

Keeping in mind the somewhat ad-hoc way test cases are built, one may ask whether forcings can be used that are derived in a more objective way. Recently, a SCM test bed has been developed, which uses forcings directly derived from 3D simulations (Neggers, 2008). We investigate how these model derived forcings compare to the GABLS3 case specifications, and how these forcings impact on the SCM model results.

Given the uncertainty in the forcings, it is likely insufficient to examine only one case to distinguish between different turbulence closures. A way to move forward is to run an ensemble of comparable cases and average the results in order to improve the signal to noise ratio. This approach is pursued in the last part of this paper. Finally, we explore the possibility to design a single composite case from the ensemble of selected cases.

In section 5.2 the relevant model physics are described. The case-study is introduced in section 5.3. Section 5.4 explores the sensitivity of SCM simulations for differences in the turbulence parameterization and in the large-scale forcings. In section 5.5 we explore the potential to perform SCM studies based on multiple cases, using forcings derived from 3D simulations. Section 5.6 presents the conclusions.

5.2 Model description

We use the SCM version of the ECMWF model. A complete description of the model can be found at

<http://www.ecmwf.int/research/ifsdocs/CY31r1/index.html>. Since this study is on the evolution of the wind field, we only present the prognostic equations for the horizontal wind components (u, v):

$$\begin{aligned}\frac{\partial u}{\partial t} &= -\left(u \frac{\partial u}{\partial x} + v \frac{\partial u}{\partial y}\right) - w \frac{\partial u}{\partial z} + f(v - v_g) - \frac{\partial \overline{u'w'}}{\partial z} \\ \frac{\partial v}{\partial t} &= -\left(u \frac{\partial v}{\partial x} + v \frac{\partial v}{\partial y}\right) - w \frac{\partial v}{\partial z} - f(u - u_g) - \frac{\partial \overline{v'w'}}{\partial z}.\end{aligned}\quad (5.1)$$

Here w denotes the vertical wind velocity, f the Coriolis parameter, and (u_g, v_g) the components of the geostrophic wind. Primes indicate turbulent fluctuations and overbars indicate averages (note that the overbars for the mean variables are omitted). For the present case-study, the vertical advection of momentum is generally small compared to the horizontal advection. All terms of Equation (5.1) are either explicitly resolved in the SCM or provided as external forcings (horizontal advection and vertical velocity), except for the last terms on the right hand side, which represent the turbulent flux divergence. The vertical turbulent flux of any variable, ψ , is parameterized following K -theory:

$$\overline{\psi'w'} = -K_\psi \frac{\partial \psi}{\partial z}. \quad (5.2)$$

Here K_ψ represents the so-called eddy-diffusivity.

We employ different approaches for parameterization of turbulent transport. A popular way to parameterize K is first-order closure. In this case, above the lowest model level

$$K_{m,h} = \frac{l_{m,h}^2}{\phi_m \phi_{m,h}} \left| \frac{\partial U}{\partial z} \right|, \quad (5.3)$$

where ϕ_m and ϕ_h are the well-known flux-profile relations that account for the influence of stability (e.g. Andreas, 2002; Baas et al., 2006) and l is a length scale. The subscripts m and h refer to momentum and heat, respectively.

Recently, a turbulent kinetic energy (TKE) closure scheme was implemented in the SCM, in particular to improve the representation of the convective boundary layer (Lenderink and Holtslag, 2004). The TKE closure scheme parameterizes the eddy diffusivity as

$$K_{m,h} = l_{m,h} \sqrt{E}, \quad (5.4)$$

The turbulent kinetic energy, E , is given by the prognostic TKE equation:

$$\frac{\partial E}{\partial t} = -\left(\overline{u'w'} \frac{\partial u}{\partial z} + \overline{v'w'} \frac{\partial v}{\partial z}\right) + \frac{g}{\theta_v} \overline{w'\theta'_v} - \frac{\partial}{\partial z} (\overline{w'E} + \overline{w'p'}/\rho) - \varepsilon. \quad (5.5)$$

The different terms on the right-hand side represent the effects of wind shear, buoyancy, transport of TKE and dissipation, respectively. The dissipation is proportional to $E^{3/2}/l_m$.

For stably stratified conditions the length scale is given by

$$\frac{1}{l_{m,h}} = \left(\frac{1}{c_n k z} + \frac{1}{l_\infty} \right) + \frac{1}{l_s} \quad (5.6)$$

with $l_\infty = 75$ m. The constant $c_n (= 0.516)$ follows from surface layer matching. In near-neutral conditions l is dominated by the first term on the right-hand side of Equation (5.6). The length scale for stable conditions (Deardorff, 1980),

$$l_s = c_{m,h} \frac{\sqrt{E}}{N}, \quad (5.7)$$

dominates the very stable regime. N denotes the Brunt-Väisälä frequency, given by

$$N = \sqrt{\frac{g}{\theta_v} \frac{\partial \theta_v}{\partial z}}. \quad (5.8)$$

The parameters c_m and c_h in Equation (5.7) are related through

$$c_m = c_h \text{Pr} = c_h (1 + c_p Ri_g), \quad (5.9)$$

where Pr is the turbulent Prandtl number and Ri_g is the gradient Richardson number. In this study, amongst others, we explore the sensitivity of the representation of the wind field in the SBL to the choice of the parameters c_h and c_p , which determine the efficiency of the vertical diffusion. For more details of the length scale formulation we refer to Lenderink and Holtslag (2004). Baas et al. (2008a) related the mixing characteristics of the TKE closure scheme to the stability functions applied in first order schemes.

5.3 Introduction to the case and set-up of simulations

Out of eight years of observations from the Cabauw measuring site, the night of 1-2 July 2006 has been chosen as the third GABLS intercomparison case-study. This particular night was selected because of its well-developed LLJ in a cloud free and relatively stationary synoptic situation. The advection of dry continental air prevents the formation of fog. The geostrophic wind amounts to 8 m s^{-1} . Cabauw is situated in the western part of the Netherlands in topographically flat terrain (51.971°N , 4.927°E). The area around the site consists of meadows, tree lines, and scattered villages (van Ulden and Wieringa, 1996; Beljaars and Bosveld, 1997). The North Sea is situated about 50 km to the WNW.

Figure 5.1 shows the time-height variation of the observed wind speed, obtained from the 200 m tower and a wind profiler. In the convective boundary layer, the winds have a rather constant value with height of about 5 m s^{-1} . After the evening transition, the residual layer becomes decoupled from the surface. During the night, a well-developed inertial oscillation (IO) results in a pronounced LLJ (Blackadar, 1957). The jet reaches its maximum strength ($\sim 13 \text{ m s}^{-1}$) just before midnight. Its core is situated at 200 m above the surface, which coincides with the

height of the surface inversion. These are common characteristics for LLJs above Cabauw (Baas et al., 2009a).

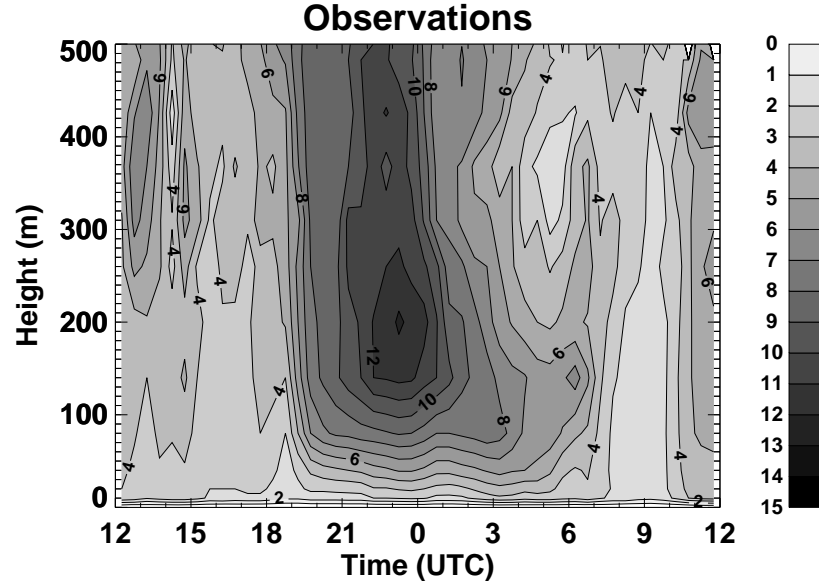


Figure 5.1: Time-height plot of the wind speed as observed by the tower and the wind profiler for the GABLS3 period (1200 UTC 1 July 2006 – 1200 UTC 2 July 2006).

The SCM experiments have been configured as follows. The simulations are initialized at 1200 UTC, 1 July 2006 and the integration time is 24 hours. Local noon is at 1140 UTC. The model consists of 80 vertical levels. The lowest model levels are situated at approximately 10, 30, 60, 90, 125, 170, 210, and 270 m above the surface. The time step is 10 minutes. We use the case set-up of the GABLS3 intercomparison study as a reference (Baas et al., 2008b). A summary of the case specifications follows below.

Initial profiles are based on tower observations and atmospheric soundings. A fully interactive soil-vegetation scheme is applied. Figure 5.2a,b show the evolution of the prescribed surface geostrophic wind components. These values are an interpolation of hourly geostrophic winds derived from a planar fit of pressure observations from eight synoptic weather stations in a radius of 75 km around Cabauw. At each moment in time, the surface value of the geostrophic wind vector, \mathbf{V}_g , is interpolated upward linearly to a value of $(u_g, v_g) = (-2; 2) \text{ m s}^{-1}$ at 2000 m height. The decrease of the magnitude of \mathbf{V}_g with height is motivated by the decrease of the actual wind observed in atmospheric soundings and by the geostrophic wind field as calculated by a 3D model. Above 2000 m \mathbf{V}_g is taken constant.

Figure 5.2c,d present the prescribed advective tendencies for momentum in the layer between 200 and 1000 m. Above 1000 m the values are set to 0, below

200 m the tendencies are interpolated linearly towards 0 at the surface. The tendencies are mainly based on the 200 m wind observed at the tower. It is assumed that during the night the amount of turbulence at 200 m is negligible. This seems justified, since at this height the IO has its largest amplitude. Given the 200 m wind vector at sunset and the prescribed \mathbf{V}_g , the momentum equation (Equation (5.1)) was integrated at this level for the night time hours neglecting the advection terms. The difference between a frictionless evolving IO and the observations at 200 m is attributed to advection. A simple block function is then fitted through the resulting advection terms, providing the forcing terms for the intercomparison study. The layer in which the advection is applied (between 200 to 1000 m) is based on dynamical tendencies as provided by 3D simulations of RACMO2 (see Appendix 5A). Both the veering of \mathbf{V}_g in time and the presence of significant advective tendencies indicate that some mesoscale synoptic feature passes the measurement site during the night. Tendencies for temperature and humidity have been derived in an analogous way. Their influence on the dynamics is small. The prescribed subsidence rate is taken directly from the 3D model output.

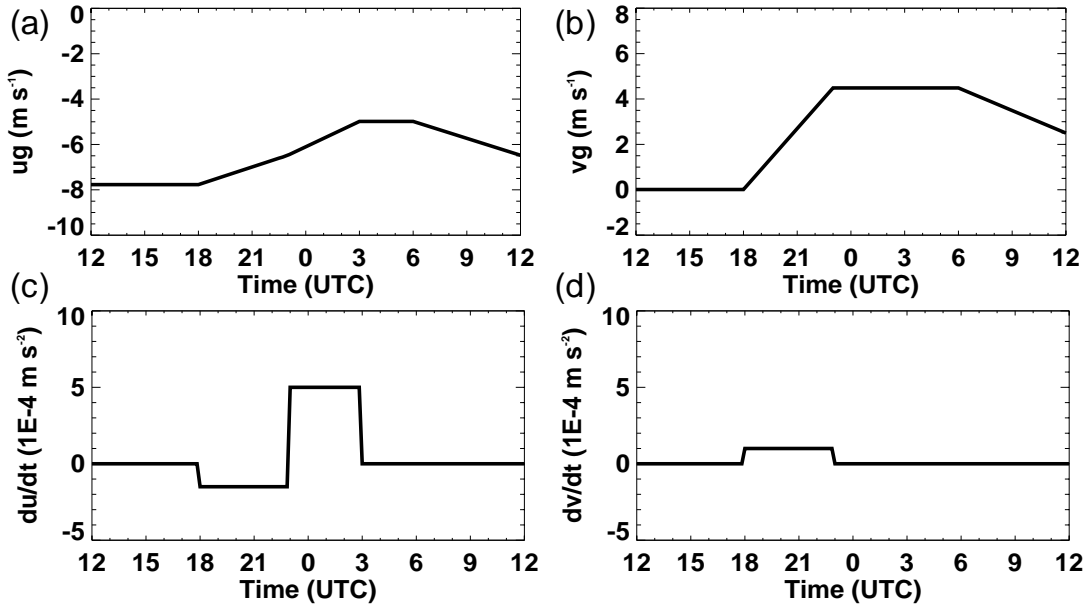


Figure 5.2: Geostrophic wind components at the surface (a and b) and momentum tendencies (c and d) as prescribed in the GABLS3 case set-up.

5.4 Sensitivity analysis using the GABLS3 set-up

To study the dependencies of the SCM results on the turbulence parameterization and the large-scale forcings, different SCM experiments are performed. All sensitivity runs have a unique label and are described in Table 5.1. To get a

qualitative picture of the performance of the different SCM experiments, Figure 5.3 shows time-height plots of the wind speed for a few selected runs. These

Table 5.1: Overview of SCM experiments.

Label	Description
<i>Perturbed physics</i>	
TKE_std	TKE closure; $c_h = 0.15$, $c_p = 1$; reference simulation
TKE_ch01cp1	TKE closure; $c_h = 0.10$, $c_p = 1$
TKE_ch02cp1	TKE closure; $c_h = 0.20$, $c_p = 1$
TKE_ch015cp0	TKE closure; $c_h = 0.15$, $c_p = 0$
TKE_ch001	TKE closure; $c_h = 0.01$, $c_p = 1$
C31_LTG	1 st order closure, C31r1 physics with revised Louis-Tiedtke-Geleyn (LTG) stability functions (Viterbo et al., 1999)
C31_BH91	As previous, but with Beljaars and Holtslag (1991) functions
<i>Perturbed geostrophic forcing</i>	
VGavg	Time dependence of \mathbf{V}_g removed (\mathbf{V}_g averaged over time)
VGbarotr	Height dependence of \mathbf{V}_g removed (surface value taken for whole vertical domain)
VGp1p1	Surface values of u_g and v_g both increased by 1 m s^{-1}
VGp1m1	Surface values of u_g increased by 1 m s^{-1} , of v_g decreased by 1 m s^{-1}
VGm1p1	Surface values of u_g decreased by 1 m s^{-1} , of v_g increased by 1 m s^{-1}
VGm1m1	Surface values of u_g and v_g both decreased by 1 m s^{-1}
<i>Perturbed momentum tendency</i>	
ADVno	Momentum tendencies neglected
ADVt-1	Momentum tendencies shifted one hour backward
ADVt+1	Momentum tendencies shifted one hour forward
ADVhalf	Magnitude of momentum tendencies divided by two
<i>Forcings from 3D model results</i>	
3DTKE	Forcings taken from 3D run with TKE closure ($c_h = 0.15$, $c_p = 1$)
3DC31	Forcings taken from 3D run with 1 st order closure (LTG functions)

figures can be directly compared to Figure 5.1, which presents the observed wind field. The TKE_std (Figure 5.3a) run will serve as a reference throughout this study. In general, this run provides an adequate representation of the LLJ, although at altitudes above 150 m and simulation times after 0400 UTC the correspondence with observations is reduced. The latter is because the forcings chosen for the GABLS3 case become less realistic after 0400 UTC. Changing the model physics (Figure 5.3b and 5.3c) leaves the temporal evolution intact, but affects the strength and the height of the LLJ. As such, the shear below the LLJ is modified considerably. Changing the forcings has impact on the total structure of the wind field: the simulation which neglects the advective tendencies (ADVno, Figure 5.3d) does not reproduce the fast decrease in wind speed observed between 0100 and 0300 UTC. Below, the sensitivity experiments are analysed in more detail. In Section 5.4.4, a quantification of the uncertainties is presented by means of model scores.

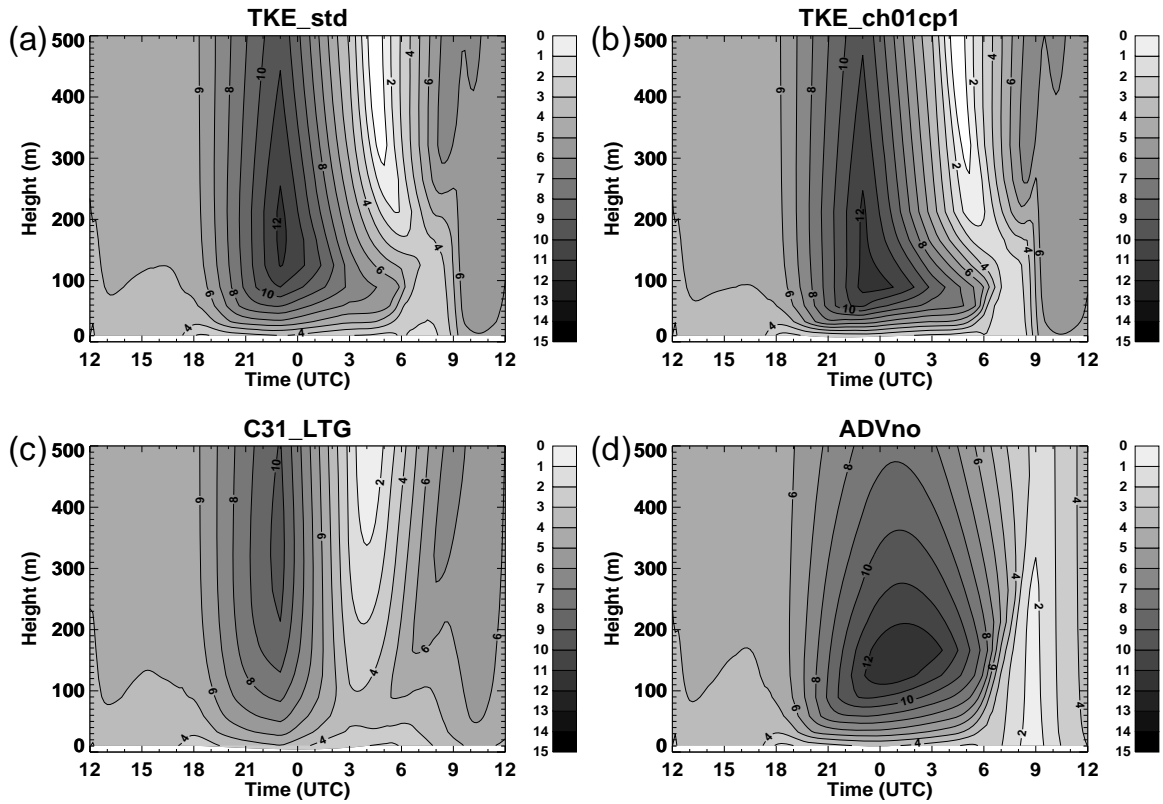


Figure 5.3: Time-height plots of wind speed (in m s^{-1}) for selected SCM simulations.

5.4.1 Sensitivity to model physics

Combining different values for the free parameters c_h and c_p (see Equation (5.6)) results in five runs with the TKE scheme, including a simulation for the (unphysical) limit situation in which turbulence is completely suppressed above the first model layer (10 m). This is achieved by setting c_h to a value of 0.01 (TKE scheme). In addition, two simulations are performed with a first order closure scheme.

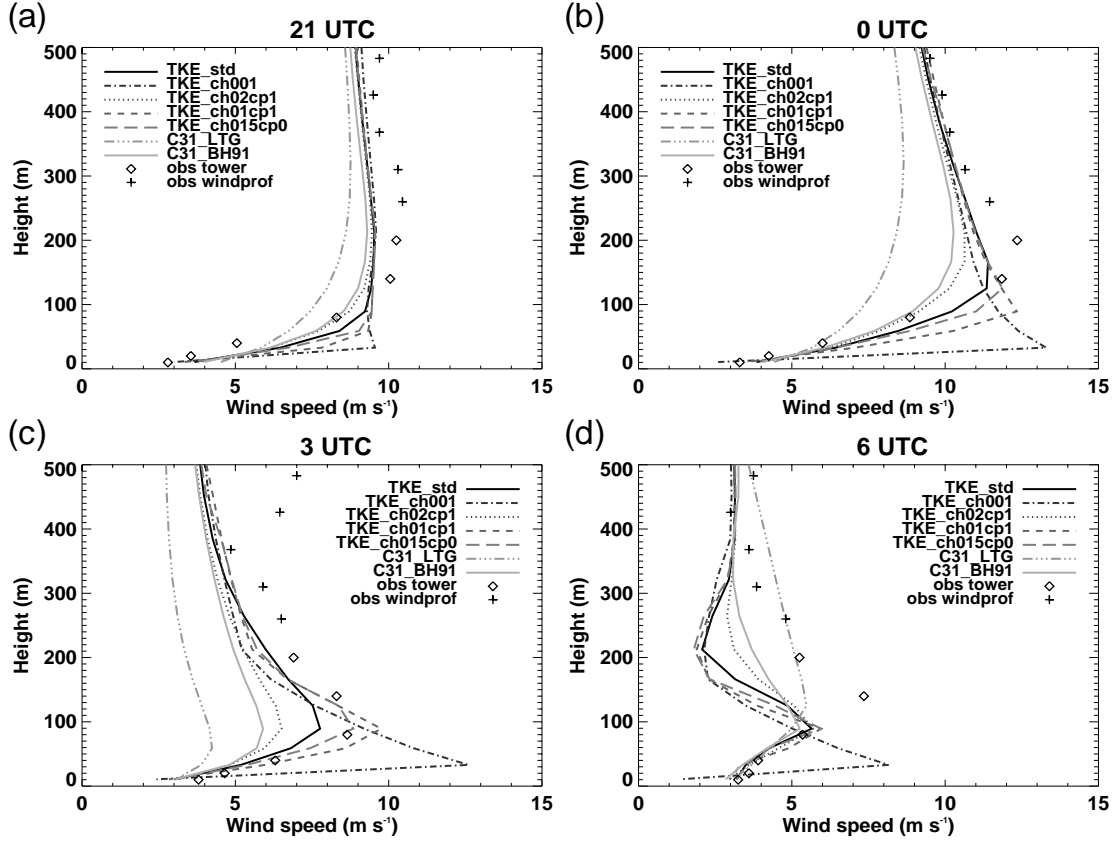


Figure 5.4: Profiles of wind speed at 2100 (a), 0000 (b), 0300 (c), and 0600 UTC (d) for different diffusion parameterizations. Observations are indicated by diamonds (tower) and plusses (wind profiler).

For these seven different turbulence formulations, Figure 5.4 shows vertical profiles of the wind speed at 2100, 0000, 0300, and 0600 UTC, together with observations from the tower and the wind profiler. Like the observations, the model results show a well-developed IO. At 2100 UTC differences are relatively small. Later during the night the model runs diverge. The unphysical TKE_ch001 simulation is included to illustrate the limit of no turbulent diffusion. Above the first model level (below which standard MO theory is applied), this simulation exhibits a freely evolving IO. The altitude below which the other simulations start

to deviate from this run, marks the top of their turbulent layer. Model simulations with more (less) mixing produce slower (faster) LLJs at a higher (lower) altitude. At 0600 UTC, which is 2 h after sunrise, the growing convective boundary layer has reached a depth of about 100 m. In this layer differences between the simulations, apart from the unphysical one, have almost completely disappeared and the correspondence with the observations is very good.

The C31_LTG simulation shows the consequences of applying so-called enhanced mixing. While beneficial for model performance on the medium-range synoptic scale, the nocturnal LLJ is almost totally mixed away (see e.g. Beljaars, 1995; Cuxart et al., 2006; Edwards et al., 2006). When stability functions with more realistic mixing characteristics are applied (C31_BH91), the representation of the LLJ improves. A run with log-linear functions with a slope of 5 (not shown) generates wind profiles which are practically identical to the TKE_ch15cp0 simulation (cf. Baas et al., 2008a).

In the upper part of the profiles, well above the SBL, turbulence does not play a role anymore and the difference between the simulations decreases. Close to the ground (that is to say at the lowest model level, which in our case is at 10 m), differences between the runs are small. At this level the wind is largely determined by the surface layer parameterization and the land-surface interactions, which we do not further discuss in this study. We conclude that the sensitivity to the diffusion parameterization appears to be the largest in the bulk of the SBL. Here non-diffusive schemes (such as TKE_ch01cp1) exhibit still a frictionless IO, while the oscillation in schemes with more mixing (such as C31_LTG) is already seriously damped by friction.

5.4.2 Sensitivity to perturbations of the forcings

To determine the sensitivity to the large-scale forcings, a set of simulations is performed with plausible variations in the prescribed forcings. Figure 5.5a shows vertical profiles of the wind speed at 0000 UTC for different geostrophic forcings. All experiments are carried out with standard settings of the TKE scheme ($c_h=0.15$, $c_p=1$).

First, the time dependence of \mathbf{V}_g is removed, by averaging the surface values of \mathbf{V}_g . The dependence with height is maintained. The corresponding SCM simulation, VGavg, fails to reproduce the LLJ correctly. Soon after initialization the simulated wind vector drifts away from the observations, because in the afternoon the prescribed \mathbf{V}_g is not realistic. By the time of decoupling, between 1700 and 1800 UTC, the ageostrophic wind component is much smaller than in reality. As a result, the amplitude of the IO (and therefore also the nocturnal LLJ) is underestimated.

Alternatively, we neglect the dependence of V_g with height (VGbarotr). In this simulation the wind speed above about 150 m is much higher than for the other SCM experiments. This is not surprising, since in reality V_g decreases with height. The residual layer does exhibit an IO, but a jet-like profile is lacking because the model's ageostrophic wind component is constant with height. Finally, the surface geostrophic wind has been modified by adding and subtracting 1 m s^{-1} to both its u and v-component, resulting in four additional simulations. Given a quantification of the error in estimating the geostrophic wind from the network of pressure observations, the shift of 1 m s^{-1} in both directions is a realistic disturbance. These modifications of V_g affect mainly the magnitude and the phase of the IO. Above 100 m, this causes differences up to 3 m s^{-1} in the modelled wind speed. The height of the LLJ is affected, as well. The results of the VGavg and the VGbarotr simulations demonstrate that the consequences of making crude approximations to the prescription of the geostrophic wind are that the nocturnal evolution of the wind cannot be simulated anymore in a satisfactory way. Even slight modifications of V_g have a significant influence on the modelled wind profile, in particular above the boundary layer. In the lowest 100 m, the SCM results are relatively insensitive to variations in V_g .

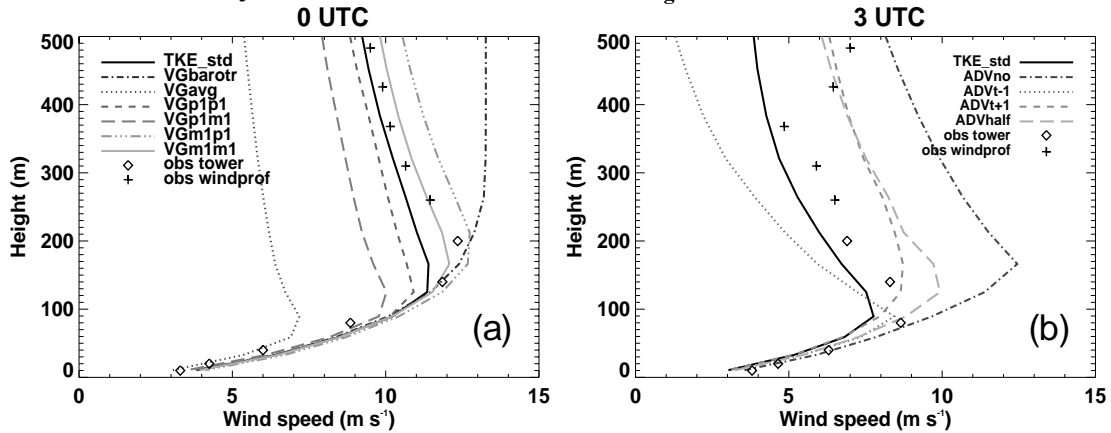


Figure 5.5: Profiles of wind speed at 0000 UTC for different geostrophic forcings (a) and at 0300 UTC for perturbations in the momentum tendencies (b).

Next, the horizontal advective tendencies of momentum are modified to examine their impact on the SCM results. First the tendencies are neglected completely. Then two simulations are performed for which the timing of momentum advection is shifted one hour forward and one hour backward, respectively. Finally, the advective tendencies are divided by two.

From 2300 UTC onwards, the prescribed zonal component of the momentum tendency has a considerable value for four hours (see Figure 5.2c). Therefore, Figure 5.5b presents profiles of the wind speed at 0300 UTC for the various model runs. When the momentum tendencies are neglected, the rapid

decrease in wind speed after 0000 UTC is not resolved. At 0300 UTC the difference between this run and the reference simulation has increased to 5 m s^{-1} . A shift of the advective events one hour forward or backward in time influences the wind profiles considerably: the later the advection is applied, the higher the wind speeds in the second half of the night. Dividing the tendencies into halves, results in too high wind speeds. Note again that below 100 m differences are relatively small.

5.4.3 Forcings from 3D model simulations

As discussed above, the large-scale forcings of the GABLS3 case description are mainly based on observations. However, one might argue that the method by which these forcings are derived is rather tailored for this case, and can not easily be applied in general. Furthermore, the method is arguably at least to some extent subjective. Therefore, we also drive our case-study with forcings directly derived from output of simulations with a 3D model. We use the Regional Atmospheric Climate Model (RACMO2). Appendix 5A provides background information on this model and explains how the forcings for the SCM simulations are derived.

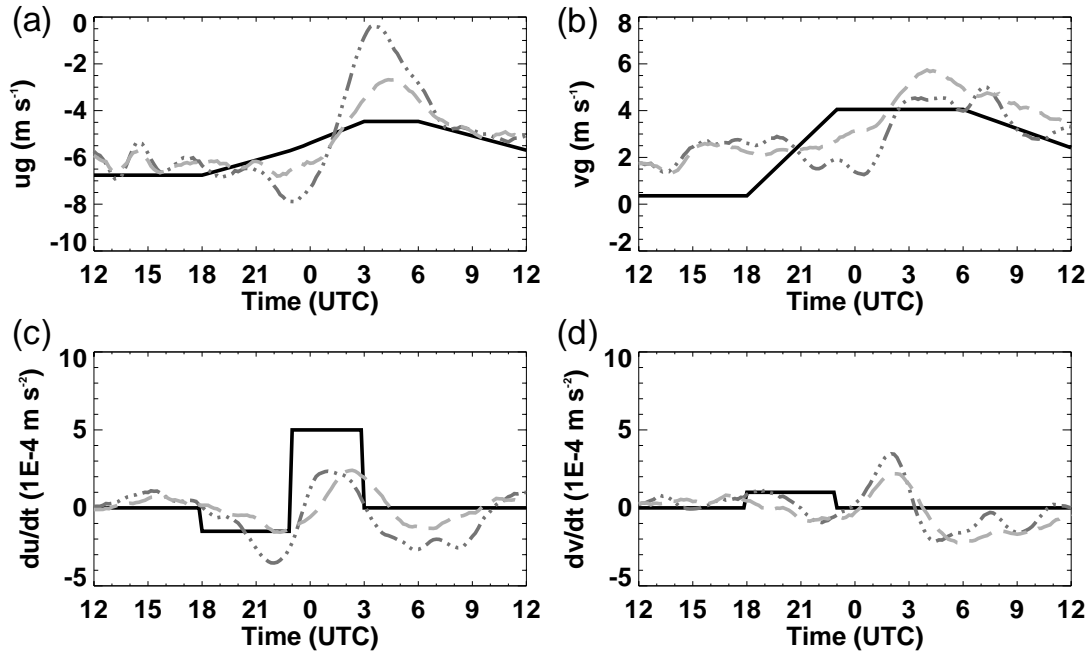


Figure 5.6: Geostrophic winds and momentum tendencies derived from 3D RACMO2 simulations averaged over the layer between 200 and 500 m. The full line represents the GABLS3 set-up, the dashed-dotted line the 3DTKE simulation, and the dashed line the 3DC31 run.

Figure 5.6 shows both components of \mathbf{V}_g and the advective tendencies of momentum as applied in the GABLS3 case set-up and provided by two 3D simulations of RACMO2 with different turbulence schemes. The average values between 200 and 500 m above the surface are presented. Averaging over a layer enables a more objective comparison, because in the different model simulations the advective patterns are not necessarily situated at exactly the same height. The TKE simulation applies the standard parameter settings, which correspond to realistic mixing efficiencies. The C31 run uses the default LTG stability functions. Figure 5.6 shows that the turbulence parameterization in 3D runs has a significant influence on the provided dynamical forcings. The forcings based on the simulation with C31 physics tend to show a more gradual evolution in time. This could be explained by the fact that the C31 formulation is much more diffusive, which potentially dampens mesoscale features in the flow. Additional 3D simulations indicate that differences in domain size and horizontal resolution have a relatively small impact on the resulting forcings (not shown).

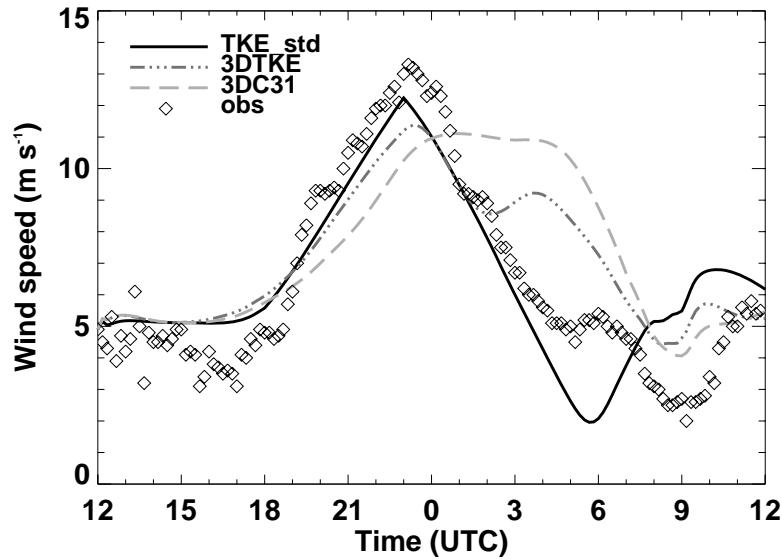


Figure 5.7: Time series of the 200m wind speed for three SCM simulations with different forcings. Tower observations are added for comparison.

Clear deviations exist between the forcings provided by the two 3D simulations and the forcings applied in the GABLS3 set-up. The impact on the SCM results is shown in Figure 5.7, which presents time series of the 200 m wind speed. Both the 3DTKE and the 3DC31 runs fail to capture the rapid decrease of the wind speed after midnight. For the GABLS3 case the use of large-scale forcings derived from 3D model output results in considerable deviations of the SCM results from the observations at the height of the LLJ.

5.4.4 Quantification of uncertainties

Can observations be used to discriminate between different parameterization schemes given the uncertainty in the forcings? This subsection attempts to answer this question quantitatively by attributing model scores to SCM sensitivity experiments. We use the magnitude of the difference vector between the model wind and the observed wind averaged over the period from 1800 UTC to 0600 UTC to measure the performance of a particular SCM run. This quantity was chosen because we are primarily interested in SBL wind profiles.

The 12 sensitivity runs with perturbed forcings (see Table 5.1) were not only integrated with the reference TKE_std formulation, but also with three alternative turbulence formulations, labelled TKE_ch015cp0, TKE_ch02cp1, and C31_LTG (Table 5.1). Together with the undisturbed experiments, which follow exactly the GABLS3 set-up, this gives four times 13 SCM sensitivity experiments. For each of these runs model scores were calculated at 200 m, 80 m and 10 m above the surface.

To discern between parameterization we propose using scatter plots in which the scores of all perturbed experiments of one formulation are plotted versus those of a second formulation. Figure 5.8 shows a comparison of the TKE_std formulation with the other three formulations at 200 m, 80 m, and 10 m. The spread of the data points shows the variability due to uncertainty in the forcings. If a data point is on the 1:1 line the scores of the two turbulence formulations are identical for that particular sensitivity experiment. Firstly, Figure 5.8 shows that the variations induced by perturbation of the forcings are correlated; a perturbation which reduces the performance of one parameterization will generally reduce the performance in the other parameterizations as well. This enhances the ability to distinguish between parameterizations. Secondly, Figure 5.8 shows that the reference case set-up ('plus' sign) has generally very good scores compared to the perturbed experiments. On the opposite, with the crude approximation employed for VGavg (asterisk in Figure 5.8) very inaccurate simulations are obtained. Thirdly, Figure 5.8 confirms that the influence of the forcings on the model results becomes smaller for decreasing height above the surface; the variation in the scores becomes much smaller when going from 200 m to 80 m to 10 m (note the difference in the axes). This appears also from the experiments driven by forcings derived from 3D model output (black squares): at 200 m these perform relatively bad, while at 80 m they perform well in comparison to the other sensitivity experiments. Finally, Figure 5.8 confirms the conclusions from the Sections 5.4.1 and 5.4.2. At 200 m the different formulations perform comparable, except for C31_LTG which shows larger errors. At 80 m the ability to distinguish between model formulations appears to be larger than at 200 m: at this level TKE_std gives consistently lower model errors than

TKE_ch015cp0, while at 200 m the two formulations perform the same. The TKE_std and TKE_ch02cp1 formulations perform similar for this case at all levels. At 10 m the variations between the different parameterizations is very small (except for C31_LTG).

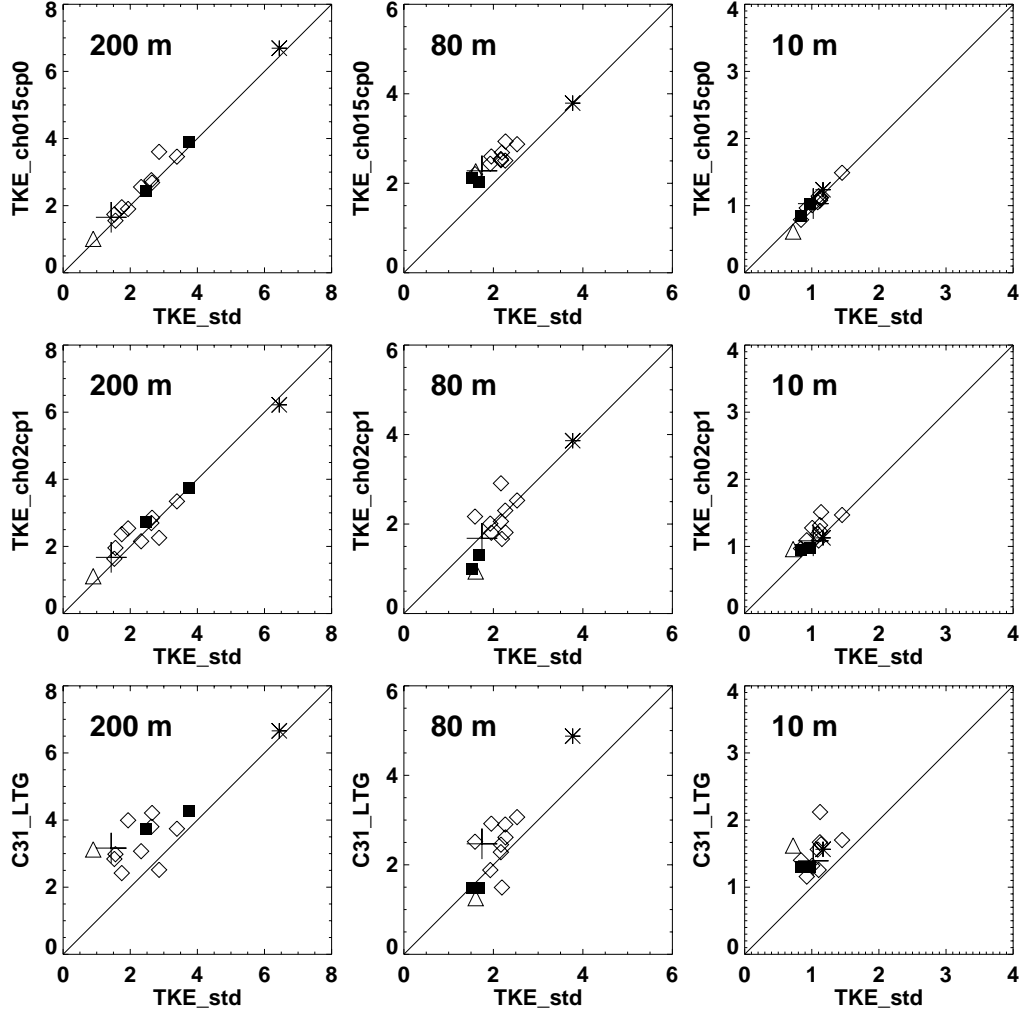


Figure 5.8: Quantitative comparison of turbulence formulations for SCM sensitivity experiments at 200 m, 80 m, and 10 m. The time-averaged magnitude of the difference vector between model results and observations (in m s^{-1}) between 1800 UTC and 0600 UTC is used as a measure (note the difference in the axes). The TKE_ch015cp0, the TKE_ch02cp1, and the C31_LTG formulations are compared to the TKE_std formulation. Open diamonds indicate experiments with perturbed forcings (geostrophic wind and momentum tendencies) as listed in Table 5.1 (VGavg is indicated separately by an asterisk), the ‘plus-sign’ indicates the undisturbed GABLS3 set-up, the black squares indicate the experiments that use forcings from 3D model runs (Table 5.1). The triangle indicates the composite run discussed in Section 5.5.3.

5.5 Composite case

The previous section showed that the dynamic forcings play an important role in the GABLS3 case study (see Figure 5.6). This section analyses eight summertime LLJ events observed at Cabauw to determine whether the GABLS3 case is an exception or that in practice mesoscale disturbances will always play a role. The application of 3D model derived forcings for driving SCM runs is investigated further. In addition, we explore the potential for setting-up an SCM intercomparison study based on a composite case.

5.5.1 Selection of comparable cases

The Cabauw database was examined to find cases with characteristics comparable to the GABLS3 case. From an eight year database (2001-2008), we selected all 24-hour periods from 1200 UTC to 1200 UTC the next day with practically clear sky conditions; during night-time the net radiation was required to be below -30 W m^{-2} , during daytime the short wave incoming radiation was required to be within 100 W m^{-2} of the calculated clear sky shortwave radiation. The geostrophic wind speed was required to vary less than 3 m s^{-1} between 1800 UTC and 0600 UTC and to have values between 5 and 15 m s^{-1} . We focus on the months May, June, and July, because in this period the night time length is relatively constant. This simplifies a comparison of the selected cases. In total, 16 nights were found that satisfied the above criteria. All of these cases show a nocturnal LLJ with a background flow from south-easterly directions (note that there was no selection on these characteristics). From the subset of 16 nights, eight of them with the most ‘ideal’ IOs were selected by eye. That is to say, in order to minimize the influence of mesoscale disturbances, only those cases were chosen in which the wind vector at 200 m rotated as smoothly as possible around the geostrophic wind. In six of the eight selected cases the geostrophic wind decreases with height, indicating that differences in baroclinicity between the cases are small. The data of the cases are included in Figure 5.9.

5.5.2 Model results of an ensemble of cases

The eight selected nights were simulated with 3D RACMO2 (TKE scheme) to compose forcing terms for SCM simulations. Next, each case was simulated with the SCM (TKE scheme, reference parameter settings) using the corresponding forcings from the 3D model. Initial profiles were taken from the 3D model results. Figure 5.9 shows the results for the 200 m wind speed. The thick solid line indicates the average over the eight cases. The diamonds show the corresponding averaged hourly observations. The observations and the average SCM results show a good agreement. This suggests that, at least for the type of cases we study,

large scale forcings derived from 3D models results can be successfully used to perform ensemble averaged SCM studies. When forcings derived from 3D simulations using the C31 (LTG) turbulence formulation are employed, almost similar results are obtained for the ensemble average. The GABLS3 night is part of the ensemble and is indicated by the bold dashed-dotted line (labelled by 20060701). To avoid any confusion, we repeat that this particular simulation does not follow the GABLS3 case set-up, but is driven by output from the 3D model. The thin lines represent the seven other cases of the ensemble and give an impression of the case-to-case variability. This variability shows that in most cases subtle variations in the forcings are present. Apparently, the evolution of the wind field is very sensitive to small mesoscale disturbances, even for these cases, which were selected to have relatively stationary synoptic conditions.

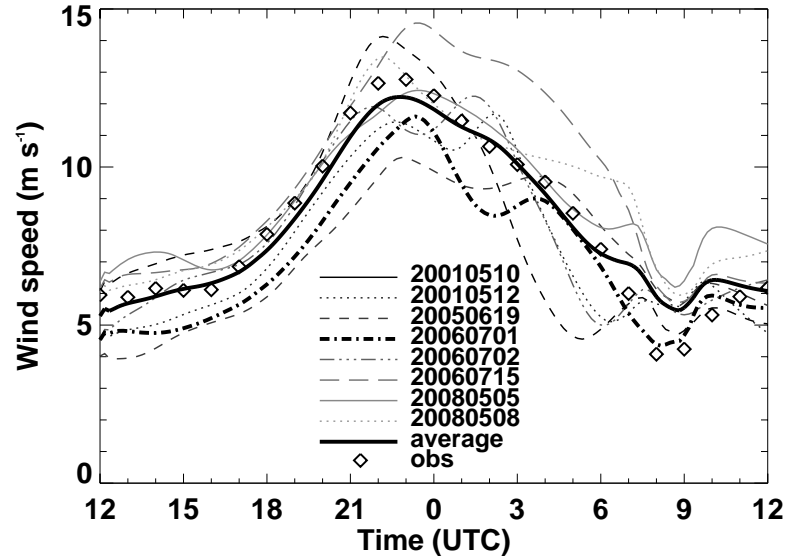


Figure 5.9: Time series of the 200 m wind speed for SCM simulations of eight selected nights using forcings derived from 3D model output. The thin lines represent individual cases (labelled by their respective date, yyyyymmdd), the simulation that corresponds to the GABLS3 night (20060701) is indicated by the bold dashed-dotted line. The full line gives the average of the SCM runs, the diamonds give the averaged observations.

The ensemble averaged wind speed may resemble the observed ensemble mean very well, but how is the performance of the SCM results on a case-to-case basis? Figure 5.10 shows time series of the magnitude of the difference vector between the SCM winds and the observations for each individual case at 200 m above the surface. Again, the GABLS3 night is indicated separately by the bold dashed-dotted line (labelled by 20060701); the thinner lines represent the other seven cases. For the first 12 h of the simulations, the scores of the GABLS3 night

do not differ from the other cases. Then, its performance deteriorates for a few hours, but in the end the scores go back to average values.

For comparison, scores for the TKE_std run, which is driven by the forcings of the GABLS3 case set-up, are added to Figure 5.10. From 1200 to 2200 UTC this run performs comparable to the 20060701 run, which corresponds to the same night but is exclusively driven with forcings from the 3D model. From 2200 to 0500 UTC, which is the major part of the duration of the LLJ, the results of the TKE_std run correspond much better to the observations. In the final part of the simulation, the performance of the TKE_std run is deteriorated because the forcings of the GABLS3 set-up become less realistic for this time period.

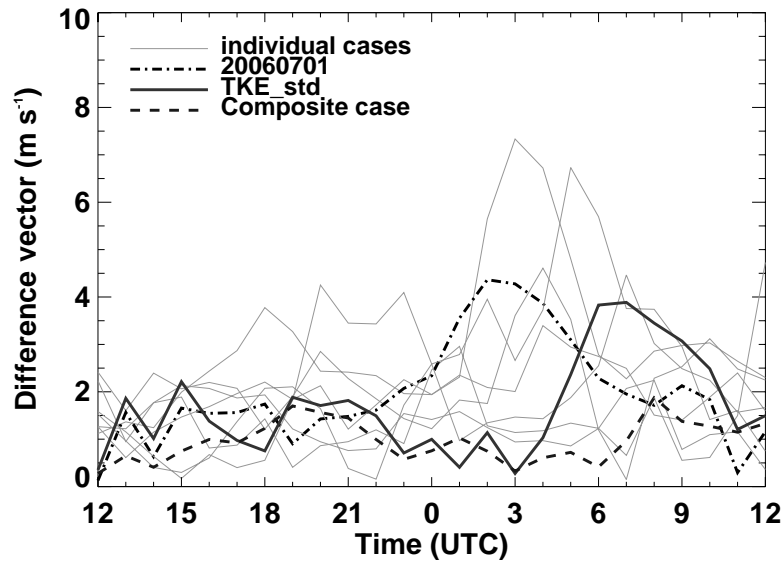


Figure 5.10: Time-series of the magnitude of the wind vector difference at 200 m between SCM results and observations for eight selected summertime LLJ cases. The GABLS3 night (one of the ensemble members) is highlighted by the dashed-dotted line. Time series for the TKE_std simulation (which follows the GABLS3 set-up) and a composite SCM run are added for comparison.

Model scores (the time averaged difference vector between modelled and observed wind between 1800 UTC and 0600 UTC) are presented in Table 5.2 for different heights above the surface and the different ensemble members. Compared to the simulation following the GABLS3 case set-up, TKE_std, the average over the eight ensemble members is slightly worse at 80 m and considerably worse at 200 m. Thus, on a case basis it appears to make sense to manually adapt the forcings (as done in the GABLS3 case setup) to obtain an optimal simulation.

Table 5.2: Model scores for various SCM experiments at 200 m, 80 m, and 10 m above the surface. The time-averaged magnitude of the difference vector between model results and observations (in m s^{-1}) between 1800 UTC and 0600 UTC is used as a measure.

	200 m	80 m	10 m
TKE_std	1.4	1.7	1.0
<i>Ensemble members</i>			
20010510	0.9	2.0	1.3
20010512	2.6	2.5	0.7
20050619	3.4	2.1	0.8
20060701	2.2	1.6	1.0
20060702	2.9	2.5	1.1
20060715	2.7	2.9	1.1
20080505	1.0	1.6	1.0
20080505	1.8	1.1	0.9
Average over 8 cases	2.2	2.0	1.0
<i>Composite case</i>			
Comp_TKE_std	0.9	1.6	0.7
Comp_TKE_ch02cp1	1.1	0.9	1.0
Comp_noadv	2.5	2.0	0.9
Comp_relax	1.0	1.7	0.7

5.5.3 Composite case

By averaging the forcings of the eight selected cases, a composite case can be defined. Figure 5.11 shows averaged geostrophic winds and tendencies of momentum. For each of the cases the wind and wind tendency vectors have been rotated towards the ensemble time averaged surface geostrophic wind. For an ideal composite case of the nocturnal boundary layer, \mathbf{V}_g would be constant in time and the momentum tendencies negligible, but this turns out not to be the case. A clear veering is present in \mathbf{V}_g and the tendencies show a systematic pattern. This agrees with the findings of Tijn et al. (1999) that in The Netherlands in summertime a diurnal cycle in the wind direction can be distinguished. As a result of the differential heating of the North Sea and the land surface during the day, the air pressure becomes relatively high above sea and relatively low above land. As a result, a NNE-SSW oriented component in \mathbf{V}_g develops (i.e. parallel to the coast). When after sunset the land-sea temperature contrast diminishes (or even reverses), this component disappears. For a south-easterly background flow, this means that \mathbf{V}_g will veer during the night. Since we selected only cases with high solar

insolation in the months May, June, and July, it is not surprising that this veering appears in our averaged V_g time series. Time-height plots of V_g obtained from the 3D model results (not shown) indicate that this feature is confined to the lowest 1500 m of the atmosphere. Also the momentum tendencies show a systematic pattern over the day. We speculate that the observed patterns in V_g and the momentum tendencies are related to a mesoscale circulation induced by the sea, the lowlands of The Netherlands and the low mountain ranges (~ 500 m) in Germany and Belgium about 300 km from the coast (personal communication Tijm, 2008). Because the off-shore component of the geostrophic wind is larger than 5 m s^{-1} , no sea-breeze front penetrates inland (Tijm et al., 1999).

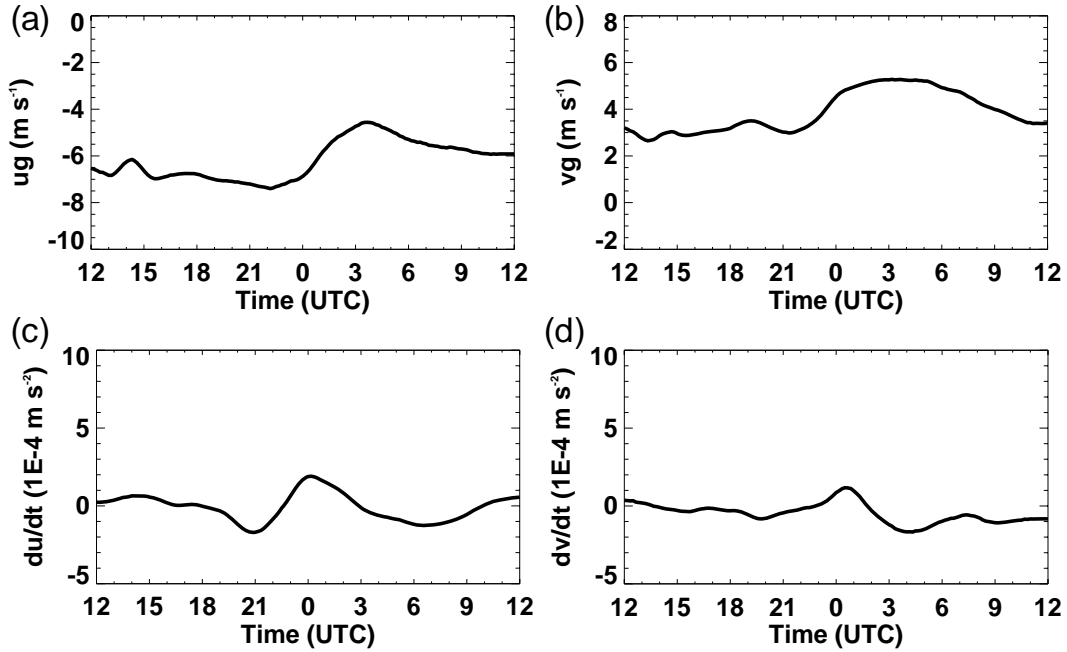


Figure 5.11: Geostrophic wind and tendencies of momentum averaged over eight selected cases. Average values between 200 and 500 m are shown.

The forcings presented in Figure 5.11 have been used to drive a composite SCM case. As initial profile, the average of the rotated 3D initial profiles is taken. Figure 5.12 compares composite model results with observations at 200 (a) and 80 m (b). To illustrate the differences between a composite case and a single case, similar time series are presented for the GABLS3 case (Figure 5.12c and d). For the composite case, the reference run, `Comp_TKE_std`, compares reasonably well with the composite observations. Figure 5.10 shows that the performance of this `Comp_TKE_std` is better than the performance of the SCM results of most individual cases. The composite run performs comparable to the reference simulation of the GABLS3 case (`TKE_std`), except for the final part of the simulation where it is much closer to the observations.

These findings are confirmed by model scores presented in Table 5.2. The Comp_TKE_std run performs better than the average of the scores of the eight individual cases. The composite case was run with three alternative turbulence formulation, i.e. TKE_ch015cp0, TKE_ch02cp1, and C31_LTG (see Table 5.1). Figure 5.8 shows that for all formulations the scores of the composite case (triangles) are better than the scores of the reference GABLS3 run ('plus-sign'). Differences between various parameterizations may not be larger than for the individual case, but the combination of data from multiple cases enhances the confidence that the observed differences are significant.

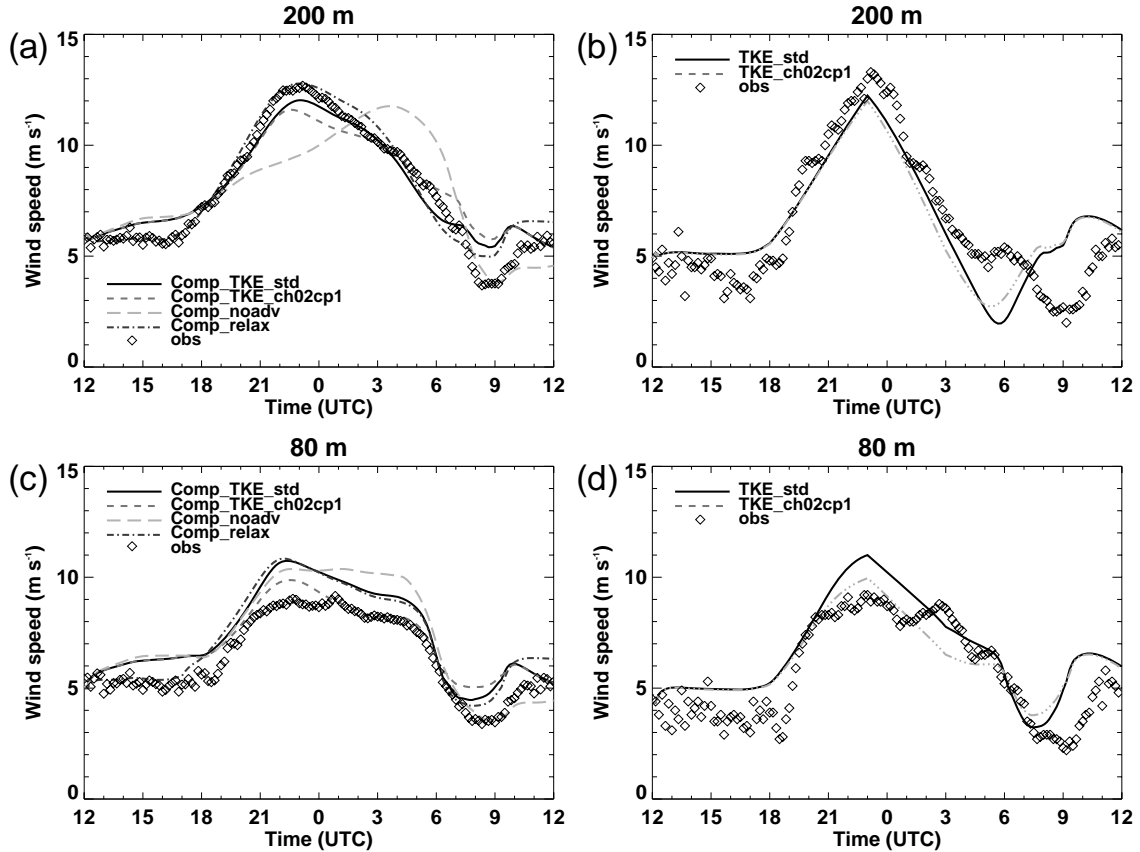


Figure 5.12: Time series of observed and modelled wind speed at 200 and 80 m for the composite case (a and c) and for the GABLS3 case (b and d).

Figure 5.12 shows the benefits of a composite case above an individual case: at the different levels the noise in the composite observations is much less than in the observations of the individual GABLS3 case, which simplifies a comparison with model results. For illustration, results of SCM runs with slightly different mixing characteristics are presented. For the composite case, at 80 m the Comp_TKE_ch02cp1 run is closer to the observations than the reference (Comp_TKE_std) simulation (see also Figure 5.8 and Table 5.2). For the

individual GABLS3 case this is harder to conclude, because randomly distributed disturbances mask the generic signal.

Figure 5.12a shows that neglecting the averaged momentum tendencies (Comp_noadv) deteriorates the model performance at 200 m considerably (see also Table 5.2). At 80 m the influence of the forcings appears to be smaller. The composite case, Comp_TKE_std, seems to underestimate the increase of wind speed in the development stage of the nocturnal LLJ (Figure 5.12a). However, this is not necessarily caused by errors in the night time mixing by the SBL turbulence parameterization. Already at the evening transition (around 1700 UTC) the magnitude of the difference vector between the SCM simulation and the observations amounts to about 1 m s^{-1} . This difference influences the development of the nocturnal IO in the model, illustrating that the evolution of the SBL depends on the representation of the preceding daytime boundary layer (Tjemkes and Duynkerke, 1989). To show the impact of this, we relaxed the SCM solution rigidly towards the observations until sunset and let the model evolve freely from there. The relaxation time amounts to 1 h. The results, labelled with Comp_relax, show almost no underestimation of the amplitude of the 200 m wind. However, it appears from Table 5.2 that the scores for Comp_relax are not better than for Comp_TKE_std. This is due to a decrease in performance of Comp_relax in the second half of the night.

The potential of a composite case in comparison with an individual case is evident. A relevant question is how many cases are needed to be able to construct a successful composite case. It is difficult to answer this question in general terms. For an increasing ensemble size the errors of the composite case are expected to reduce because randomly distributed disturbances will average out progressively. However, the answer will depend on the nature of the disturbances, but also on the type of boundary layer or phenomenon that is studied. A possible approach would be to perform SCM simulations on an operational basis. This would allow, for example, for composing monthly averages of variables or situations as desired (personal communication Neggers, 2009).

5.6 Conclusions

A comparison of Single Column Model (SCM) results with observations is often hampered by uncertainties in the forcings. This makes it difficult to discriminate between different parameterization schemes. We analysed the role of large-scale forcings on SCM simulations of the summertime low-level jet (LLJ) at Cabauw, The Netherlands. Using the SCM version of the ECMWF model, we performed a sensitivity study to the turbulence parameterization and to the influence of the

large-scale forcings. We studied the GABLS3 intercomparison case, as well as an ensemble of eight comparable cases, all selected from the Cabauw data base.

For these cases, the LLJ is situated at the top of the stable boundary layer (SBL), 200 m above the surface. The SCM results are most sensitive to the turbulence parameterization in the bulk of the SBL, roughly between 50 and 150 m. Above 150 m the role of turbulence decreases and the results from the different model runs converge, except for the most aggressive mixing scheme. Below 50 m, the representation of the surface layer and the surface boundary conditions (the soil-vegetation scheme) dominate. Perturbing the geostrophic wind and the tendencies of momentum gave large differences in the simulation of the wind. However, below 100 m the sensitivity of the simulated winds to the forcings decreases strongly. This indicates that particularly at levels between about 50 and 100 m above the surface (i.e. between 25% and 50% of the turbulent layer), observations are suitable to discriminate between turbulence parameterizations.

Model errors were quantified by using the magnitude of difference vector between the modelled and the observed wind as a measure. A method was proposed to compare different parameterizations given the uncertainty in the dynamical forcings. It is found that a particular perturbation of the dynamical forcings which reduces the performance of one parameterization will generally reduce the performance of other parameterization, as well. This enhances the ability to distinguish between parameterizations.

To enable a comparison of turbulence schemes with observations within the SBL, it is crucial that the wind at the top of the boundary layer is represented with satisfactory agreement. For this to achieve, a detailed prescription of the forcings is required. To arrive at realistic forcings, local observations or physical constraints can be used as was done, for example, in the GABLS3 intercomparison study. Given the observed sensitivity to the forcings, SCM studies should always be accompanied by some sensitivity experiments. For individual cases, forcings directly derived from 3D model output do not yield satisfactory results at the height where the LLJ is typically positioned. Even more, forcings derived from 3D simulations that used different physical parameterizations proved to be significantly different. Future developments in assimilating local observations into high-resolution models may give a better representation of meso-scale disturbances, which would enable a more accurate forcing of SCMs.

A way to move forward is to run an ensemble of comparable cases and then average the result. We selected eight summertime LLJ cases from the Cabauw data-archive. Each of these cases has been simulated with the SCM, steered by forcings obtained from 3D model output. Correspondence between averaged observations and ensemble averaged SCM results appears to be very good. When an ensemble of cases is considered, 3D model derived forcings can be adequately

used, because in this approach randomly distributed disturbances tend to average out. As a by-product, we found a systematic pattern in the dynamic forcings, which is probably related to the differential heating of land and sea.

As a step further we defined a composite case by averaging the forcings over eight selected LLJ cases. The resulting composite SCM run represented the observations better than the SCM results of most individual cases. Moreover, the fact that observations from multiple cases are combined may enhance the confidence in the results. The smoother time evolution of the winds in the composite case greatly enhances the ability to compare SCM results with observations, and to assess the quality of the boundary layer parameterizations. For defining a proper composite case, a prerequisite is that a sufficiently large database must be available to select suitable cases from. Using a composite case makes it easier to get insight in the strengths and weaknesses of a model.

Acknowledgements

We thank Henk Klein Baltink for processing and providing the wind profiler data. This work has been inspired by many discussions with colleagues at KNMI, Wageningen University, and the GABLS community. The first author has been supported by the Netherlands Organization for Scientific Research (NWO), in particular through the project “land surface climate and the role of the stable boundary layer”.

Appendix 5A: Dynamical forcings for SCM integrations from RACMO2

The Regional Atmospheric Climate Model (RACMO2) (van Meijgaard et al., 2008) uses the semi-Lagrangian dynamics kernel of HIRLAM. The physical package is derived from the ECMWF model. In this study we do simulations with the ECMWF CY31r1 physics and with the TKE scheme described in section 5.2. The domain size of our 3D simulations is about 1100 x 1100 km, centred on The Netherlands. The horizontal resolution amounts to 12 km. In the vertical, 40 layers are used. The lowest layers are situated at about 10, 40, 80, 130, 200, and 300 m. As boundary conditions ECMWF operational analyses are used.

To drive SCM runs, both the horizontal and vertical part of the dynamic tendencies are required. Concerning momentum, the semi-Lagrangian scheme provides the *total* dynamic tendencies, i.e. the sum of the horizontal advective tendency, the vertical advective tendency and the geostrophic departure term. To enable an estimation of the horizontal tendency, RACMO2 provides additional variables like the geostrophic wind and the vertical velocity, as well. By means of these variables the horizontal momentum tendency is deduced from the total

tendency. To make sure that the SCM is subjected to the same forcing as the column in the 3D model, the horizontal diffusion is added. In the SCM the vertical advection is calculated from the vertical motion as provided by the 3D model and the vertical gradients as calculated by the SCM itself. At last, the resulting tendencies are interpolated to the 80 levels of the SCM configuration.

6 Summary, Reflections, and Outlook

6.1 Summary

The subject of this thesis is the atmospheric nocturnal stable boundary layer (SBL) over land. SBLs form after sunset when the long-wave radiative cooling of the surface is not compensated for anymore by shortwave radiation from the sun. Therefore, the surface cools and the air adjacent to the surface becomes stably stratified, in particular for clear skies. An important characteristic of stably stratified flows is that vertical motions (turbulence) are suppressed by buoyancy effects; air parcels that are vertically displaced in a stably stratified environment tend to move back to their original position due to the restoring force of gravity. At the top of the SBL often a maximum in the wind speed profile is observed, the nocturnal low-level jet (LLJ). It forms after sunset in response to the fast collapse of the vigorous turbulent motions of the daytime convective boundary layer.

In the SBL many physical processes play a role, for example, turbulence, long-wave radiative flux divergence, gravity waves, slope flows, and interactions with the land surface. The complex interactions between these processes complicate modeling of the SBL, especially in weak wind conditions. This thesis aims to improve the understanding of SBL processes, in particular turbulent mixing and the development of the nocturnal LLJ. Another purpose is to test various turbulence mixing assumptions from literature in a single-column model (SCM) in comparison with selected tower and land surface data. Finally, it is aimed to make a climatology and classification of SBL observations, suitable to evaluate the performance of atmospheric models.

Chapter 2 presents a climatology of nocturnal LLJs at Cabauw, The Netherlands. Seven years of data from a 200 m tower and a wind profiler system are analyzed to derive characteristics of the LLJ. In this study, a LLJ is defined as a maximum in the wind speed profile in the lowest 500 m of the atmosphere. The decrease in wind speed above the wind maximum is required to be both larger than 2 m s^{-1} and larger than 20 % of the observed wind maximum. For each night only the wind profile six hours after sunset is analyzed, to guarantee that the detected LLJs were in the same phase of their development. At this moment in time, LLJs approximately attain their maximum strength. At Cabauw, in about 20% of the nights a maximum in the wind speed profile is observed. These LLJs are typically situated at 140-200 m above the surface, and have a speed of 6 to 10 m s^{-1} .

The observations were classified in terms of the two main forcings of the SBL, namely the geostrophic wind and the radiative cooling. In this way, nine SBL classes are defined varying from clear sky and calm conditions to cloudy conditions with strong winds. It is shown that this classification covers a wide

range of SBL wind and temperature structures. For each of these classes LLJ characteristics are determined. Significant LLJs are most likely to occur for a moderate geostrophic forcing in combination with clear skies. In general, it is found that the frequency of occurrence of LLJs increases with decreasing wind forcing and with increasing cooling. The turning of the wind vector between the jet nose and the surface seems to be rather insensitive to the wind forcing, but becomes larger for increasing cooling. The average height of the jets increases with stronger wind forcing and with weaker cooling.

A comparison with model reanalysis (ERA40) illustrates the potential for model evaluation. In ERA40 the frequency of LLJ occurrence and the wind turning between the jet and the surface are underestimated. Furthermore, the LLJs are generally situated at a higher level than in the observations.

The representation of LLJs in atmospheric models depends on the formulation of turbulent mixing. Turbulent processes cannot be resolved directly, but must be parameterized. In many models, stability effects are accounted for by semi-empirical flux-gradient relations. Chapter 3 provides a critical discussion of these relations. In the literature it is generally found that scatter in the dimensionless temperature gradient, ϕ_h , is larger than in the dimensional wind shear, ϕ_m , when plotted versus the stability parameter z/Λ (where Λ is the local Obukhov length). This peculiarity is explained to be a result of self-correlation, caused by the occurrence of common variables on the y and the x axis. Self-correlation is a mathematical effect that spuriously masks spread in scatter plots. It appears that scatter in ϕ_m is artificially suppressed, while for ϕ_h this is not the case. For ϕ_m this may lead to false confidence in the found relations, especially for stronger stabilities when measuring errors can be significant. To avoid self-correlation and the large relative errors related to the ‘flux-based’ MOST, Chapter 3 suggests to use a scaling approach based on gradients (e.g. on the Richardson number), instead.

Flux-gradient relations are applied in so-called first-order turbulence schemes, where the magnitude of turbulent mixing is basically a function of the local gradient of the mean quantity. Another popular approach to parameterize turbulence is the so-called 1.5-order or turbulent kinetic energy (TKE) closure method. In this case the efficiency of turbulent mixing is made a function of the TKE, which is now prognostically resolved in the model. Chapter 4 discusses how the scaling behavior of a TKE-closure scheme relates to the flux-gradient relations discussed in Chapter 3. The analysis is done by using a state-of-the-art SCM. From the model equations, expressions are derived for the stable limit behavior of the TKE-scheme in terms of the flux-gradient relations. It turns out that the scaling behavior of the model depends on only a few parameters of the TKE scheme and that local scaling theory is strictly followed. The analytical findings are illustrated

with model runs for the second GEWEX Atmospheric Boundary Layer Studies (GABLS) intercomparison study. Solutions were investigated for the case in which an empirical correction function was included that increases the eddy-diffusivity for momentum for an increasing Richardson number. It is demonstrated that including such empirical correction functions may have large and undesired consequences for the model behavior.

In Chapter 5 much of the previous material comes together. SCMs are widely employed to test boundary layer parameterizations. However, these models must be driven by the large-scale forcings on the column, like the geostrophic wind and the advective tendencies. Unfortunately, these forcings are inherently uncertain and are often contaminated by mesoscale disturbances. This complicates a comparison of SCM results with observations. The central question is therefore: can observations actually be used to distinguish between different parameterization schemes or is the spread in model results due to uncertainties in the forcings just too large? Chapter 5 investigates this question for the nocturnal LLJ.

First, a single LLJ case is analyzed. The same case has been used for the third GABLS intercomparison study. To estimate the large-scale forcings, a blend of local observations and output from integrations with three dimensional models is used. A sensitivity study to both the forcings and the turbulence formulation is performed using the SCM of the ECMWF model. It appears that the sensitivity to the turbulence formulation is largest in the bulk of the SBL, while the influence of the forcings manifests itself mainly in the upper part of the SBL and above.

Second, an ensemble of cases is investigated. Eight nights with comparable LLJs were selected from the Cabauw database. Using forcings exclusively derived from 3D model output, the selected cases were run with the SCM. Results of the individual cases show considerable differences with the observations, indicating that the quality of 3D model derived forcings is insufficient on a single case basis. However, the mean of the eight SCM integrations agrees well with the mean of the observations. By averaging the forcings of the selected cases, a single composite case is defined. Good correspondence is achieved between the composite SCM run and the composite observations. Apparently, when multiple cases are considered, randomly distributed mesoscale disturbances average out. This enables a better judgment of the quality of boundary layer parameterizations in comparison with observations.

6.2 Reflections

6.2.1 Interactions between the SBL physics and mesoscale fluctuations

In Chapter 5 eight ‘ideal’ cases of the summertime nocturnal LLJ at Cabauw were investigated. Although these cases were selected to have a stationary synoptic situation a systematic pattern in the dynamical forcings emerged, which influenced the development of the nocturnal LLJ. Recall that the Cabauw site is situated in the western part of The Netherlands and that the distance to the North Sea is 50 km. The area around the site is topographically flat. The first significant hills are located 150 km to the southeast. The presence of the sea and the hills may induce mesoscale circulations above the lower part of The Netherlands, from which the sea breeze is the most obvious example (Tijm et al., 1999). This paragraph illustrates how mesoscale circulations can influence the development of the SBL.

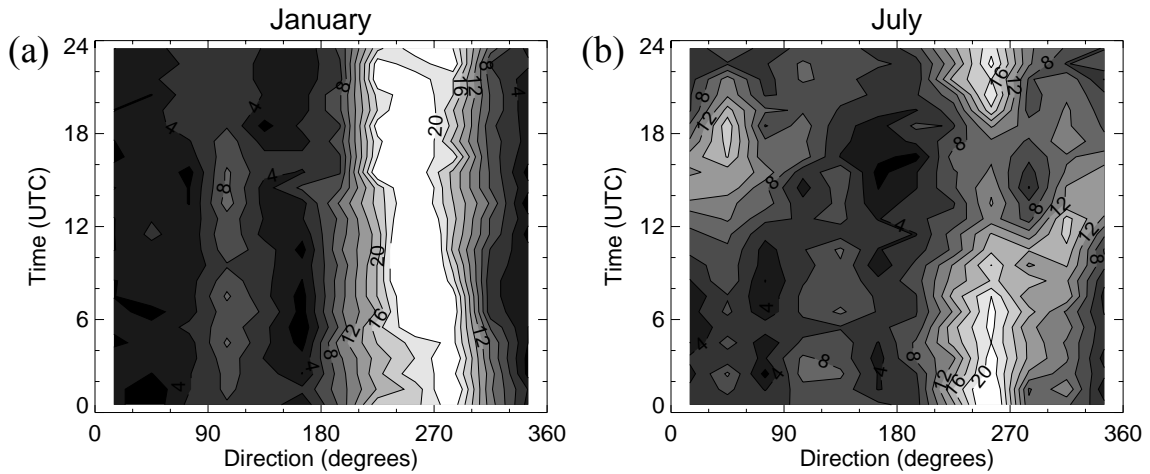


Figure 6.1: Diurnal cycle of the direction of the geostrophic wind vector for the months January (a) and July (b). The isolines represent the frequency of occurrence (in %) of the direction of \mathbf{V}_g for bins of 30° .

Van Delden (1993) and Tijm et al. (1999) presented observational evidence of a diurnal cycle in the wind direction as a result of differential heating of the land and the sea. For the month May they found an enhanced frequency of occurrence of northerly winds in the evening for meteorological stations in The Netherlands. Figure 6.1 presents an analysis of the direction of the geostrophic wind at Cabauw for January and July as derived from a network of pressure observations. The analysis is based on five years of observations. The isolines represent the frequency of occurrence of the direction of \mathbf{V}_g for bins of 30° . In January the predominant direction of \mathbf{V}_g is southwest and no diurnal cycle can be distinguished. In July the southwesterly winds are still dominant (although weaker than in January), except for the afternoon and the early evening when a clear

northeasterly component in V_g emerges. This enhanced frequency for this direction occurs from April to September. This confirms the earlier work of Van Delden (1993) and Tijn et al. (1999) that in spring and summer differential heating between sea and land affects the pressure distribution above The Netherlands. During the afternoon the pressure above land is relatively low and above sea relatively high. As a result, a northeasterly component in V_g develops, which is parallel to the coast. Due to this change in pressure gradient a sea-breeze front may start to penetrate inland. Whether this actually happens depends on additional prerequisites like the direction and speed of the background flow and the magnitude of the differential heating (Tijn et al., 1999).

It is interesting to note that the eight LLJ cases discussed in Chapter 5 all had easterly background flow. Clear skies enabled high values of sensible heat flux over land. The differential heating between land and sea induces a backing of V_g . After sunset, when the forcing of the differential heating stopped, V_g veered back to its original direction. It was demonstrated that this systematic pattern has a noticeable influence on the development of the LLJ for these cases.

One particular case has been investigated into more detail by using local observations, SCM integrations, and 3D model runs from the Regional Atmospheric Climate Model (RACMO2). It appears that in this case after midnight the wind speed decreases significantly faster than can be expected from a frictionless inertial oscillation model. This is attributed to a mesoscale dynamical feature that passes the site during the night. Inspection of 3D model results indeed suggests the presence of a mesoscale feature. It seems to originate from the leeside of the hills in Belgium and Germany. These hills have a southwest-northeast orientation and have a height of typically 500 m. After the evening transition a southwest-northeast oriented dynamical disturbance moves from the southeast to the northwest over The Netherlands. Figure 6.2 shows the zonal momentum advection at 200 m as derived from RACMO2 output at 0 UTC. The evolution of the observed wind speed at the Cabauw tower indicates that this is not just a model curiosity, but represents a realistic feature. Note that there is no data assimilation in this model. The underlying mechanism of this phenomenon is not clear, but probably the presence of the hills plays a role. It is hypothesized that during daytime the topography induces a mesoscale circulation in the wind. After sunset its forcings collapses and the disturbance in the wind field is advected with the easterly background flow over The Netherlands.

This example illustrates the complexity of the real atmosphere. For SCM case-studies often so-called golden days are selected. However, the above example shows that subtle interactions between the 3D dynamics and the local physics may easily complicate a comparison of SCM results with observations. Further

research must reveal to what extent data assimilation can contribute to a better representation of mesoscale disturbances in 3D models.

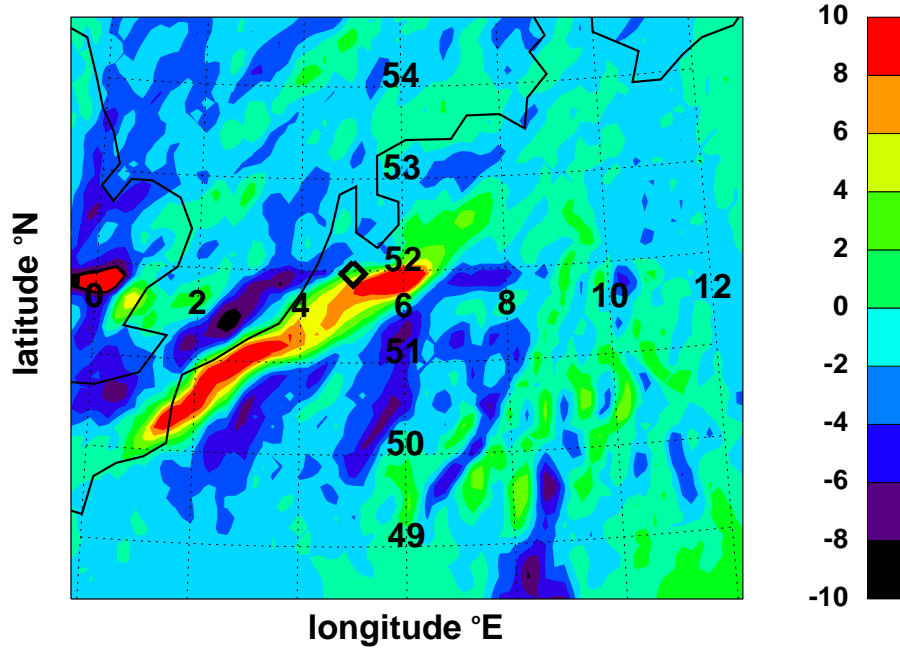


Figure 6.2: Zonal momentum advection (in $1\text{E-}4 \text{ m s}^{-2}$) at 2 July 2006, 0 UTC at 200 m as calculated from RACMO2 output. Cabauw is indicated by the diamond.

6.2.3 Turbulence formulation in climate runs

In previous Chapters various mixing formulations were tested using a SCM. Not surprisingly, removing the enhanced mixing had a positive effect on the structure of the SBL, especially on the representation of the wind field. However, a few questions remain. Firstly, only a limited amount of cases were considered. These mainly consisted of relatively well-behaved summertime cases with clear skies. All cases showed well-developed LLJs. So far, it is unclear how the TKE scheme with realistic mixing characteristics performs on a climatological basis. Secondly, removing enhanced mixing may be beneficial in SCM mode, but how does the TKE scheme perform in a less constrained and fully coupled 3D model where all kinds of three dimensional feedback mechanisms may play a role?

In this Section we discuss these questions by analyzing two eight-year climate runs of RACMO2 (pers. comm. Van Meijgaard, 2009). One run employs the reference ECMWF CY31r1 physical package, labeled STD. In this run the mixing of momentum and heat is artificially enhanced. In the other run the first order closure turbulence scheme is replaced by a turbulent kinetic energy (TKE)

closure scheme, labeled TKE. The other components of the original model are not changed. This turbulence scheme is described by Lenderink and Holtslag (2004) and has realistic mixing characteristics. Every six hours ECMWF analyses were provided as lateral boundary conditions (Lenderink et al., 2003). The horizontal resolution of the runs amounts to 50 km. The model consists of 40 vertical layers. The bottom layers are situated at (approximately) 10, 35, 70, 125, and 200 m.

This Section compares the diurnal cycle of wind and temperature in the climate runs with observations from the Cabauw measuring tower (observations at 10, 20, 40, 80, 140, and 200 m) for the period 2001-2007. The observations are compared with the model grid point which is situated closest to Cabauw. In conclusion, the impact of replacing the STD turbulence scheme by the TKE closure scheme on the 2 m temperature over Europe is presented.

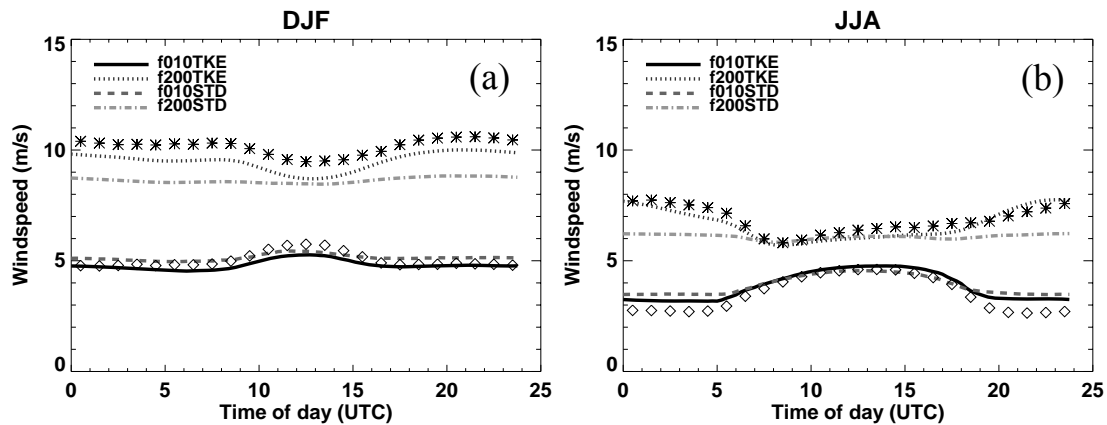


Figure 6.3: Diurnal cycle of wind speed as modeled by two climate runs for winter (a) and summer (b). Symbols indicate observations from the Cabauw tower from 10 (diamonds) and 200 m (stars).

Figure 6.3 shows the diurnal cycle of the wind speed for the three winter (DJF) and summer months (JJA). The observations show that the maximum wind speed at 10 m occurs during daytime, while at 200 m the maximum wind speed is reached during the night. The small difference between the 10 and 200 m wind during daytime in summer reflects the intense turbulent mixing under these conditions. In summer the wind speed tends to be somewhat smaller than in winter. Both model runs give a reasonable representation of the 10 m wind speed. At 200 m the STD run shows almost no diurnal cycle. The TKE run represents the observations much better: both in winter and in summer a clear diurnal cycle is present. This shows that removing the artificially enhanced mixing has clear beneficial effects on the evolution of the wind speed on a climatological basis. The effect is strongest in the upper part of the stable boundary layer.

In the boundary layer the wind is backed (turned counterclockwise) compared to the geostrophic wind due to frictional forces. Figure 6.4 presents the backing of the wind vector with respect to the geostrophic wind. Results for 10 and 200 m are shown. In this shallow layer the directional shear due to temperature advection is probably small (cf. Brown et al. 2005). The ‘observed’ surface geostrophic wind vector has been derived from a network of pressure observations, while for the climate runs the geostrophic wind was provided by the individual model runs.

The observations show clear differences between winter and summer. In summer the diurnal cycle is much stronger than in winter. In summer strong convective mixing minimizes the directional shear in the lowest 200 m, while in winter, when stably stratified conditions may regularly persist during daytime, the directional shear is larger. During daytime in the summer months the cross-isobaric angle amounts to 35° over the lowest 200 m of the boundary layer. For nocturnal conditions the observed directional shear between 10 and 200 m amounts to about 25° in winter and about 35° in summer.

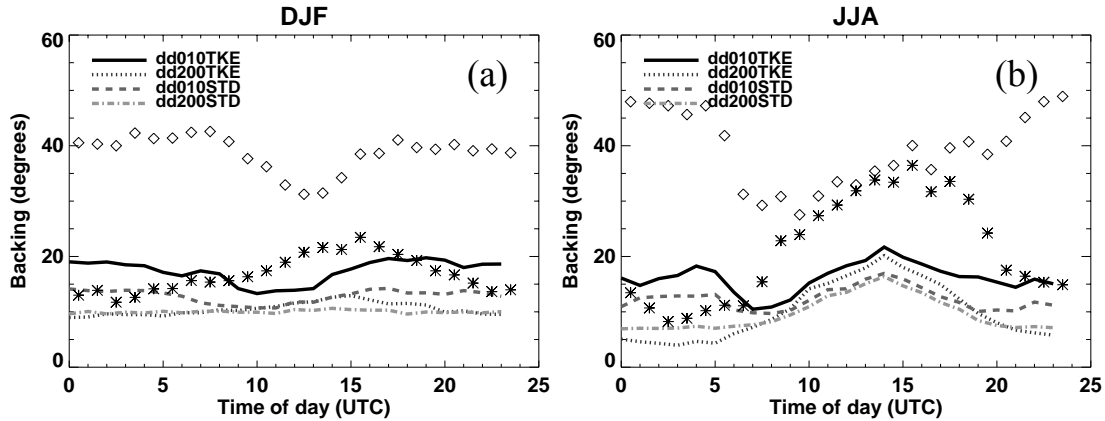


Figure 6.4: As Figure 6.3 but for the backing of the wind vector compared to the geostrophic wind.

Figure 6.4 indicates that the climate runs considerably underestimate both the directional shear between 10 and 200 m and the backing of the near-surface wind with respect to the geostrophic wind. For nocturnal conditions, the directional shear between 10 and 200 m in the TKE run is considerably larger than in the STD run. Still, this directional shear is too small compared to the observations (see also Bosveld and Beyrich, 2004; Chapter 2). The ageostrophic angle appears to be seriously underestimated in both climate runs. On average, the difference amounts to approximately 15° , both during daytime and during nighttime. The underestimation of the ageostrophic angle has detrimental effects on the modeled cross-isobaric transport of momentum. This may influence the

dynamical development of the large-scale weather patterns (Beare, 2007; Svensson and Holtlag, 2009). Since this problem, which is known for already a long time, manifests itself over the whole diurnal period, it is most likely not only a SBL problem.

The diurnal cycle of temperature is presented in Figure 6.5. For both the summer and the winter months, the STD run resembles the observations at 10 and 200 m better than the TKE run. It appears that the latter exhibits a too large diurnal cycle at the 10 m level. In winter this results in too low minimum temperatures. This feature is not occurring during summer, because by then the TKE run warms too fast during daytime. The fact that the average of a $(50 \text{ km})^2$ grid-cell is compared to single point measurements may explain part of the observed bias: Cabauw is situated in a relatively wet area, which may slow down the temperature rise during daytime. Differences between the model runs can also arise due to differences in cloud cover. Too much entrainment in the current TKE implementation might play a role, as well.

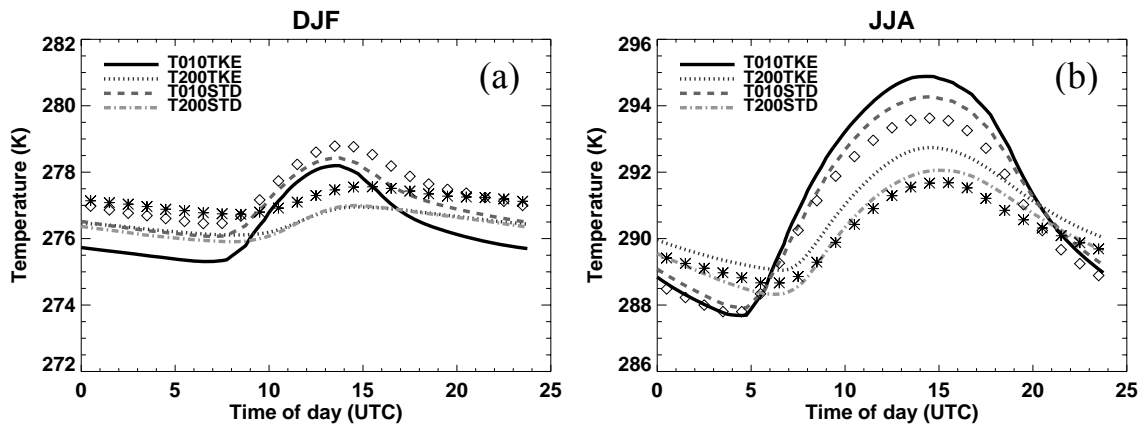


Figure 6.5: As for Figure 6.3 but for temperature.

So far, only results for a single grid point were presented. Figure 6.6 puts the previous results in a spatial perspective. It shows the bias in the daily minimum 2 m temperature in winter (DJF) of the two climate runs as compared to data from the ECA dataset (Haylock et al., 2008) for the period 2000-2006. The minimum temperature is influenced by many components of the model, for example, the turbulence formulation, the radiation budget (cloud cover), the dynamics (geostrophic forcing), the representation of the soil and the vegetation, and the possible presence of a snow cover. From Figure 6.6 it is immediately clear that large differences in the winter minimum temperature bias occur over the continent. This illustrates the complexity of atmospheric modeling. Generally, at high latitudes the models have a warm bias in the winter minimum temperature, while at lower latitudes they show a cold bias. Moberg and Jones (2004) found

comparable patterns using the regional climate model of the Hadley Centre. The warm bias at high latitudes amounts to more than 6 K in the STD run. In these areas hardly any solar radiation is present in winter. This so-called Nordic temperature bias is a persistent problem in weather and climate models. Above the snow cover, shallow surface layers develop with a very strong stratification. Replacing the enhanced mixing stability functions (STD) by a turbulence scheme with realistic mixing efficiencies (TKE) has a clear impact. In the less diffusive TKE run minimum temperatures are generally lower. This leads to a reduction of the Nordic temperature bias, although still considerable differences are present. Apart from the turbulence formulation, problems in radiation and soil processes may contribute to the warm bias in these areas. While beneficial for the high latitudes, reducing the mixing has clear negative impacts in other parts of the model domain, especially in mountainous areas as the Alps and the Norwegian Mountains. Generally, the north-south gradient in the temperature bias remains intact but is a shifted to lower values.

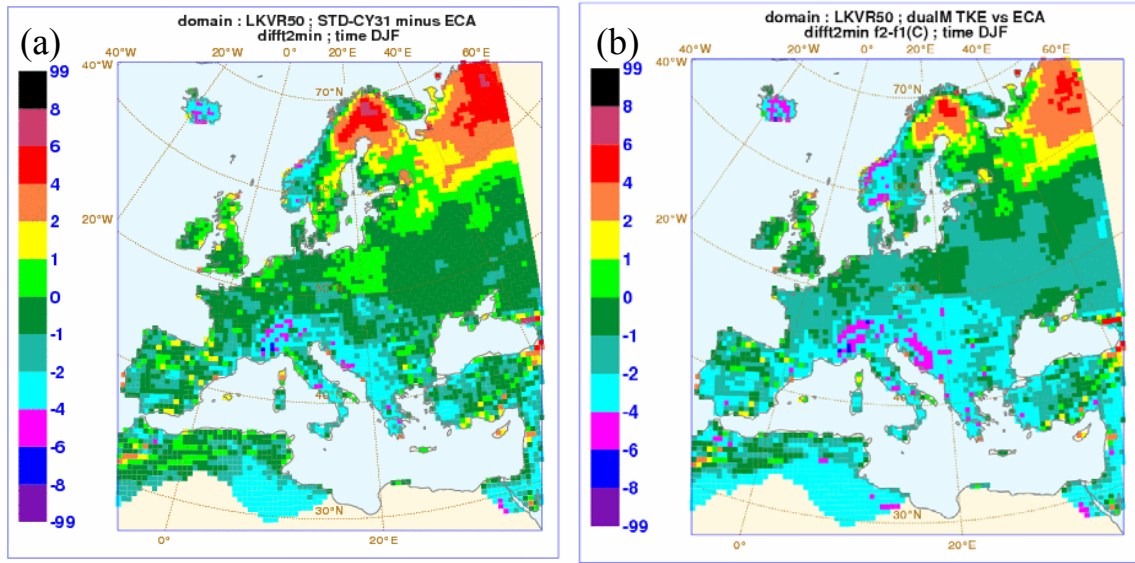


Figure 6.6: Differences in minimum 2 m temperature in winter (DJF) between two climate runs (a, STD; b, TKE) and the ECA dataset.

The results presented in this Section show that the beneficial characteristics of a TKE scheme with realistic mixing properties over an enhanced mixing first-order closure scheme, as earlier identified in SCM studies (Chapter 4, 5), are also present in a multi-year run of a fully coupled regional climate model. The representation of the diurnal cycle in the wind speed above Cabauw improves clearly, especially at 200 m. This will probably results in a better representation of nocturnal LLJs, which occur predominantly at this level. The underestimation of the directional shear and the ageostrophic angle remains problematic. The diurnal

cycle of temperature is overestimated in the TKE run. Finally, model results were compared to observed winter minimum 2m temperatures above Europe. Large differences occur over the continent. The TKE runs show consistently lower minimum temperatures than the run with reference ECMWF physics.

6.3 Perspectives

6.3.1 *Turbulence and SBL research*

In SBL modeling, the representation of turbulent mixing is of crucial importance. It determines to a large extent the structure of the wind and temperature profiles, as well as the depth of the turbulent layer adjacent to the surface. However, it is important to realize that, apart from turbulent mixing, other processes play a role. For example, breaking gravity waves impact on the momentum mixing and long-wave radiation divergence influences the temperature profile.

Nonetheless, SBL research has traditionally been focused on turbulence. This can probably be understood by the dominance of turbulence in weakly stable conditions and the success of Monin-Obukhov similarity theory in the surface layer. Moreover, with the widespread eddy-covariance technique direct measurements of turbulence can be relatively easily made, although issues like time-averaging, heterogeneity, and representativity make the interpretation of the data a challenging task (e.g. Vickers and Mahrt, 2003; De Roode et al., 2009). Still, measurements of other processes are less easily made.

For stronger stability, turbulence parameterizations are easily affected by non-turbulent processes. For example, gravity wave drag is often used as an argument for allowing more *turbulent* diffusion in the parameterization for momentum than for heat. Incorporating effects of other processes in the turbulence parameterization may blur the view on the role of turbulence and promotes compensating modeling errors. It may be one of the reasons why proposed flux-gradient relations, which are supposed to be universal, diverge so much in very stable conditions between various field experiments. To reduce ambiguity and to come to a better understanding of SBL processes and their interactions, it may be better to invest in realistic parameterizations of the separate processes themselves (see e.g. Steeneveld et al., 2008b; 2008c).

6.3.2 *Model evaluation*

In recent years, several SBL model intercomparison studies have been performed in the context of GEWEX Atmospheric Boundary Layer Studies (GABLS). The first two SCM intercomparison cases (Cuxart et al., 2006; Svensson and Holtslag, 2006) used a prescribed surface temperature as a lower boundary condition in

order to keep the cases relatively simple. The geostrophic wind was specified independently. However, Holtslag et al. (2007) concluded that spurious variability may be introduced between models when the prescribed geostrophic wind is not consistent with the prescribed surface temperature. In fact, the surface temperature is part of the solution of the problem. For this reason, the third GABLS study was performed with a fully interactive soil-vegetation scheme. In this approach, interactions between the radiation, the turbulence and the soil make the analysis of the results more complex. On the other hand it provides opportunities to learn more about the models behavior and the interactions between the different processes, which also play a role in the real atmosphere.

So far, the focus of the GABLS studies has been on the parameterization of turbulent mixing. However, in operational models the largest difficulties arise for strongly stratified boundary layers when the role of turbulence decreases and other processes like radiation divergence become relatively more important. Therefore, as suggested by Steeneveld (2007), it would be interesting to perform an intercomparison study for a situation with weak winds and a strong temperature inversion.

In order to allow for a better comparison between models and observations, a composite of cases with comparable characteristics can be defined (see Chapter 5). In this way noise of the individual cases is filtered out, while the generic signal remains. For example, it was shown that when a comparison study is based on multiple cases, large-scale forcings derived from 3D model output can be adequately used, while for individual comparison studies this is generally not the case. Using multiple cases would enable a better evaluation of boundary layer parameterizations. When constructing a composite, a careful selection of the individual cases is necessary.

Recently, a so-called testbed for SCM integrations has been set-up (Neggers, 2008). Its purpose is to evaluate parameterizations for large-scale models against atmospheric measurements on an operational basis. This testbed consists of daily forecasts of various SCMs, which are driven by forcings derived from 3D atmospheric models. The forecasts are made for various meteorological sites, among which Cabauw. The concept of this parameterization testbed has a promising potential for model intercomparison. To study, for example, the nocturnal LLJ or the temperature evolution in very stable conditions, relevant cases can be selected from the constructed archive. Next, these selected cases can be studied in more detail, for example, by making ensemble averages of relevant parameters. From a SBL perspective, it would be interesting to include a station like Sodankylä in Northern Finland. This site is situated in an area which is known for its very stable conditions and persistent warm bias in large scale models especially in the polar winter.

6.3.3 The role of the LLJ in the morning transition

The morning transition is the period after sunrise when the nocturnal inversion is eroded. It marks the onset of convective turbulence. The warming of the developing mixed layer is predominantly caused by entrainment (Angevine et al., 2001; Lapworth, 2006). The onset of convective turbulence also causes an increase in the near-surface wind. Several studies indicate that the evolution of the wind speed in atmospheric models during the morning transition is not well captured (e.g. Svensson and Holtslag, 2006).

The presence of a LLJ at the top of the nocturnal inversion may influence the evolution of the near-surface wind during the morning transition. When the growing CBL reaches the nocturnal low-level jet, fast moving air from the LLJ may be mixed towards the surface, resulting in an unexpected additional increase in the wind speed close to the surface. Possibly, the length of the night is playing a role. For example, if the nocturnal period is comparable to the period of the inertial oscillation, the LLJ will be disappeared dynamically by the time of the morning transition. This relation between the decay of the LLJ and the increase of the near-surface wind in the early morning has never extensively been studied.

6.4 Final remarks

The aim of this thesis has been to contribute to the understanding of processes in the stable boundary layer (SBL) and their representation in atmospheric models, in particular turbulent mixing and the formation of the nocturnal low-level jet (LLJ). To this end, observations were analyzed and turbulence parameterizations of SBL turbulence were tested in a state-of-the-art SCM.

This has resulted in a climatology and classification of SBL observations from Cabauw, which can be used for evaluating Numerical Weather Prediction Model and climate runs (Chapter 2). It would be interesting to perform a similar analysis with observations from other sites. An assessment was made of the influence of self-correlation on the frequently used flux-gradient relations, illustrating the problems that may arise in analyzing (SBL) observations (Chapter 3). The parameters occurring in the model equations of a TKE-closure scheme were directly related to the well-known flux-gradient relations used in first-order schemes, thus increasing the knowledge of the behavior of the model (Chapter 4). Directions for setting-up single-column model studies of the nocturnal LLJ were provided and the potential for utilizing a composite case for intercomparison studies was demonstrated (Chapter 5).

To conclude, this thesis has attempted to bring boundary layer observations and models closely together. The results may be used to further improve on the evaluation and testing methods of atmospheric models and the physical

parameterizations, which are part of them. It is also clear from the presented material that the physical understanding of SBL processes is still insufficient, especially for weak wind conditions. More fundamental research to the individual processes is still needed, although progress is expected to be slow because it is hard to disentangle the interactions between the various processes from observations. At present, many numerical weather prediction models make use of ‘enhanced mixing’ stability functions in stable conditions to increase model scores for medium-range weather forecasts. From a SBL perspective this is very disappointing, since this rules out an accurate representation of the SBL structure. More research is needed on this issue, for example, it is not clear what exactly controls the wind turning in the boundary layer in atmospheric models.

Reference list

- Akima, H., 1970: A new method of interpolation and smooth curve fitting based on local procedures. *J. Assoc. Comp. Machinery*, **17**, 589-602.
- Aldrich, J., 1995: Correlations genuine and spurious in Pearson in Yule. *Statistical Sci.*, **10**, 364-376.
- André, J.C., and L. Mahrt, 1982: The nocturnal surface inversion and influence of clear-air radiative cooling. *J. Atmos. Sci.*, **39**, 864-878.
- Anderson, C.J., and R.W. Arritt, 2001: Representation of summertime low-level jets in the central United States by the NCEP-NCAR reanalysis. *J. Climate*, **14**, 234-247.
- Andreas, E.L., 2002: Parameterizing scalar transfer over snow and ice: A review. *J. Hydromet.*, **3**, 417-432.
- Andreas, E.L., K.J. Claffey, and A.P. Makshtas, 2000: Low-level atmospheric jets and inversions over the Western Weddell Sea. *Bound.-Layer Meteor.*, **97**, 459-486.
- Andreas, E.L., and B.B. Hicks, 2002: Comments on “Critical test of the validity of Monin-Obukhov Similarity during convective conditions”. *J. Atmos. Sci.*, **59**, 2605-2607.
- Angevine, W.M., H. Klein Baltink, and F.C. Bosveld, 2001: Observations of the morning transition of the convective boundary layer. *Bound.-Layer Meteor.*, **101**, 209-227.
- Baas, P., G.J. Steeneveld, B.J.H. van de Wiel, and A.A.M. Holtslag, 2006: Exploring Self-Correlation in Flux-Gradient Relationships for Stably Stratified Conditions. *J. Atmos. Sci.*, **63**, 3045-3054.
- Baas P., S.R. de Roode, and G. Lenderink, 2008a. The scaling behaviour of a turbulent kinetic energy closure model for stably stratified conditions. *Bound.-Layer. Meteor.*, **127** : 17-36.
- Baas, P., F.C. Bosveld, G.J. Steeneveld, and A.A.M. Holtslag, 2008b. Towards a third intercomparison case for GABLS using Cabauw data. *In: 18th Symposium on Boundary Layers and Turbulence*. Stockholm, Sweden. Amer. Met. Soc., Boston, 8A.4.
- Baas, P., F.C. Bosveld, H. Klein Baltink, and A.A.M. Holtslag, 2009a. A climatology of nocturnal low-level jets at Cabauw. *J. Appl. Meteor. Climatol.*, **48**, 1627-1742.
- Baas, P., F.C. Bosveld, G. Lenderink, E. van Meijgaard, and A.A.M. Holtslag, 2009b: How to design single-column model experiments for comparison with observed nocturnal low-level jets at Cabauw?, *submitted to Q. J. Roy. Meteor. Soc.*

- Banta, R.M., C.J. Senff, A.B. White, M. Trainer, R.T. McNider, R.J. Valente, S.D. Mayor, R.J. Alvarez, R.M. Hardesty, D.D. Parish, and F.C. Fehsenfeld, 1998: Daytime buildup and nighttime transport of urban ozone in the boundary layer during a stagnation episode. *J. Geophys. Res.*, **103**, 22,519-22,544.
- Banta, R.M., R.K. Newsom, J.K. Lundquist, Y.L. Pichugina, R.L. Coulter, and L. Mahrt, 2002: Nocturnal low-level jet characteristics over Kansas during CASES-99. *Bound.-Layer Meteor.*, **105**, 221-252.
- Banta, R.M., Y.L. Pichugina, and R.K. Newsom, 2003: Relationship between low-level jet properties and turbulence kinetic energy in the nocturnal stable boundary layer. *J. Atmos. Sci.*, **60**, 2549-2555.
- Banta, R.M., Y.L. Pichugina, and W.A. Brewer, 2006: Turbulent velocity-variance profiles in the stable boundary layer generated by a nocturnal low-level jet. *J. Atmos. Sci.*, **63**, 2700-2719.
- Basu, S., Z.N. Begum, and E.N. Rajagopal, 1998: Impact of boundary-layer parameterization schemes on the prediction of the Asian summer monsoon. *Bound.-Layer Meteor.*, **86**, 469-485.
- Basu, S., F. Porté-Agel, E. Foufoula-Georgiou, J.F. Vinuesa, and M. Pahlow, 2006: Revisiting the local scaling hypothesis in stably stratified atmospheric boundary-layer turbulence: an integration of field and laboratory measurements with large-eddy simulations, *Bound.-Layer Meteor.*, **119**, 473-500.
- Basu S., A.A.M. Holtslag, B.J.H. van de Wiel, A.F. Moene, and G.J. Steeneveld, 2008: An inconvenient “truth” about using sensible heat flux as surface boundary condition in models under stably stratified regimes. *Acta Geophysica*, **56**, 88-99.
- Beare, R.J., 2007: Boundary layer mechanisms in extratropical cyclones. *Q. J. Roy. Meteor. Soc.*, **133**, 503-515.
- Bechtold, P., M. Köhler, T. Jung, F. Doblas-Reyes, M. Leutbecher, M.J. Rodwell, F. Vitart, and G. Balsamo, 2008: Advances in simulating atmospheric variability with the ECMWF model: From synoptic to decadal time-scales. *Q. J. Roy. Met Soc.*, **134**, 1337-1351.
- Beljaars, A.C.M. 1995: The Impact of Some Aspects of the Boundary Layer Scheme in the ECMWF Model. *ECMWF Seminar Proceedings on Parameterization of Subgrid Scale Physical Processes*. Reading, U.K., p 125–161.
- Beljaars, A.C.M., and A.A.M. Holtslag, 1991: Flux parameterization over land surfaces for atmospheric models. *J. Appl. Meteor.*, **30**, 327-341.
- Beljaars, A.C.M., and F.C. Bosveld, 1997: Cabauw data for the validation of land surface parameterization schemes. *J. Climate*, **10**, 1172-1193.

- Beljaars, A.C.M., and P. Viterbo, 1998: Role of the Boundary Layer in a Numerical Weather Prediction Model. in A. A. M. Holtslag and P. G. Duynkerke (eds.), *Clear and Cloudy Boundary Layers*, Royal Netherlands Academy of Arts and Sciences, Amsterdam, pp. 287–304.
- Bertin, F., J. Barat, and R. Wilson, 1997: Energy dissipation rates, eddy-diffusivity, and the Prandtl number: an in situ experimental approach and its consequences on radar estimate of turbulent parameters. *Radio Sci.*, **32**, 791-804.
- Beyrich, F., 1994: Sodar observations of the stable boundary layer height in relation to the nocturnal low-level jet. *Meteor. Z.*, **3**, 29-34.
- Blackadar, A.K., 1957: Boundary layer wind maxima and their significance for the growth of nocturnal inversions. *Bull. Amer. Meteor. Soc.*, **38**, 283-290.
- Bonner, W.D., 1968: Climatology of the low level jet. *Mon. Wea. Rev.*, **96**, 833-850.
- Bosveld, F.C., and F. Beyrich, 2004: Classifying observations of stable boundary layers for model validation. In: *16th Symposium on Boundary Layers and Turbulence*, Portland, ME. Amer. Meteor. Soc., P4.13.
- Bosveld, F.C., E.I.F. de Bruijn, and A.A.M. Holtslag, 2008: Intercomparison of single-column models for GABLS3: preliminary results. In: *18th Symposium on Boundary Layers and Turbulence*, Stockholm, Sweden. Amer. Meteor. Soc., Boston, 8A.5.
- Bougeault, P., and P. Lacarrère, 1989: Parameterization of orography-induced turbulence in a mesobeta-scale model. *Mon. Wea. Rev.*, **117**, 1872-1890.
- Brinkop, S., and E. Roeckner, 1995: Sensitivity of a general circulation model to parameterizations of cloud-turbulence interactions in the atmospheric boundary layer. *Tellus*, **47A**, 197-220.
- Brown, A.R., A.C.M. Beljaars, H. Hersbach, A. Hollingsworth, M. Miller, and D. Vasiljevic, 2005: Wind turning across the marine atmospheric boundary layer. *Q. J. Roy. Meteor. Soc.*, **131**, 1233-1250.
- Brown, A.R., R.J. Beare, J.M. Edwards, A.P. Lock, S.J. Keogh, S.F. Milton, and D.N. Walters, 2008: Upgrades to the boundary-layer scheme in the Met Office numerical weather prediction model. *Bound.-Layer Meteor.*, **128**, 117-132.
- Businger, J.A., J.C. Wyngaard, Y. Izumi, and E.F. Bradley, 1971: Flux profile relationships in the atmospheric surface layer. *J. Atmos. Sci.*, **28**, 181–189.
- Canuto, V.M., A.M. Howard, Y. Cheng, and M.S. Dubovikov, 2001: Ocean turbulence. Part I: One-point closure – momentum and heat vertical diffusivities. *J. Phys. Oceanogr.*, **31**, 1413-1426.
- Cassa-Torralba P., J. Vilà-Guerau de Arellano, F. Bosveld, M.R. Soler, A. Vermeulen, C. Werner, and E. Moors, 2008: Diurnal and vertical variability

- of the sensible heat and carbon dioxide budgets in the atmospheric surface layer. *J. Geophys. Res.*, **113**, D12119.
- Castro, C.L., R.A. Pielke Sr., and J.O. Adegoke, 2007: Investigation of summer climate of the contiguous United States and Mexico using the Regional Atmospheric Modeling System (RAMS). *J. Climate*, **15**, 3844-3865.
- Cheinet, S., A. Beljaars, M. Köhler, J.J. Morcrette, and P. Viterbo, 2005: Assessing physical processes in the ECMWF model forecasts using ARM SGP observations. *ARM Report Series No. 1*, ECMWF, U.K., 25 pp.
- Cheng, Y., and W. Brutsaert, 2005: Flux-Profile Relationships for wind speed and temperature in the stable atmospheric boundary layer. *Bound.-Layer Meteor.*, **114**, 519-538.
- Cheng, Y., V.M. Canuto, and A.M. Howard, 2002: An improved model for the turbulent PBL, *J. Atmos. Sci.*, **59**, 1550-1565.
- Cheng, Y., M.B. Parlange, and W. Brutsaert, 2005: Pathology of Monin-Obukhov similarity in the stable boundary layer. *J. Geophys. Res.*, **110**, D06101.
- Chimonas, G., 2005: The nighttime accelerations of the wind in the boundary layer. *Bound.-Layer Meteor.*, **116**, 519-531.
- Chimonas, G., and C.J. Nappo, 1989: Wave drag in the planetary boundary layer over complex terrain. *Bound.-Layer Meteor.*, **47**, 217-232.
- Conangla, L., and J. Cuxart, 2006: On the turbulence in the upper part of the low-level jet: an experimental and numerical study. *Bound.-Layer Meteor.*, **118**, 379-400.
- Cuxart, J., P. Bougeault, and J.L. Redelsperger, 2000: A turbulence scheme allowing for mesoscale and large-eddy simulations. *Q. J. Roy. Meteor. Soc.*, **126**, 1-30.
- Cuxart, J., G. Morales, E. Terradellas, and C. Yagüe, 2002: Study of coherent structures and estimation of the pressure transport terms for the nocturnal stable boundary layer. *Bound.-Layer Meteor.*, **105**, 305-328.
- Cuxart, J., A.A.M. Holtslag, R.J. Beare, E. Bazile, A. Beljaars, A. Cheng, L. Conangla, M.B. Ek, F. Freedman, R. Hamdi, A. Kerstein, H. Kitagawa, G. Lenderink, D. Lewellen, J. Mailhot, T. Mauritsen, V. Perov, G. Schayes, G.J. Steeneveld, G. Svensson, P. Taylor, W. Weng, S. Wunsch, and K.M. Xu, 2006: Single-Column Model Intercomparison for a Stably Stratified Atmospheric Boundary Layer. *Bound.-Layer Meteor.*, **118**, 273-303.
- Deardorff, J.W.: 1980, 'Stratocumulus-capped mixed layers derived from a three-dimensional model', *Bound.-Layer Meteor.*, **18**, 495-527.
- Delden, A.J. van, 1993: Observational evidence of the wave-like character of the sea breeze effect. *Beitr. Phys. Atmos.*, **66**, 63-72.
- Derbyshire, S.H., 1990: Nieuwstadt's stable boundary layer revisited. *Q. J. Roy. Meteor. Soc.*, **116**, 127-158.

- Derbyshire, S.H., 1999a: Boundary-layer decoupling over cold surfaces as a physical boundary-instability. *Bound.-Layer Meteor.*, **90**, 297-325.
- Derbyshire, S.H., 1999b: Stable boundary-layer modelling: established approaches and beyond. *Bound.-Layer Meteor.*, **90**, 423-446.
- Dijk, A. van, and A.F. Moene, 2004: The Joint Eddy-covariance Project (JEP): towards a standard for the interpretation of eddy-covariance measurements. Preprint, *16th Symposium on Boundary Layers and Turbulence*, Portland, ME, Amer. Meteor. Soc., P9.1.
- Duynderke, P.G., 1991: Radiation fog: a comparison of model simulations with detailed observations. *Mon. Wea. Rev.*, **119**, 324-341.
- Duynderke, P.G., 1999: Turbulence, radiation and fog in Dutch stable boundary layers. *Bound.-Layer Meteor.*, **90**, 447-477.
- Duynderke, P.G., and S.R. de Roode, 2001: Surface energy balance and turbulence characteristics observed at the SHEBA ice camp during FIRE III. *J. Geophys. Res.*, **106**, 15313-15322.
- Duynderke, P.G., P.J. Jonker, A. Chlond, M.C. van Zanten, J. Cuxart, P. Clark, E. Sanchez, G. Martin, G. Lenderink, J. Teixeira, 1999: Intercomparison of three- and one-dimensional model simulations and aircraft observations of stratocumulus. *Bound.-Layer Meteor.*, **92**, 453-487.
- Duynderke, P.G., S.R. de Roode, M.C. van Zanten, J. Calvo, J. Cuxart, S. Cheinet, A. Chlond, H. Grenier, P.J. Jonker, M. Köhler, G. Lenderink, D. Lewellen, C.L. Lappen, A.P. Lock, C.H. Moeng, F. Müller, D. Olmeda, J.M. Piriou, E. Sánchez, and I. Sednev, 2004: Observations and numerical simulation of the diurnal cycle of the EUROCS stratocumulus case. *Q. J. R. Meteor. Soc.*, **130**, 3269-3296.
- Dyer, A. J., 1974: A Review of Flux-Profile Relationships. *Bound.-Layer Meteor.*, **7**, 363-372.
- Edwards, J.M., 2009: Radiative processes in the stable boundary layer: part II. The development of the nocturnal boundary layer. *Bound.-Layer Meteor.*, **131**, 127-146.
- Edwards, J.M., R.J. Beare, and A.J. Lapworth, 2006: Simulation of the observed evening transition and nocturnal boundary layers: Single-column modeling. *Q. J. R. Meteor. Soc.*, **132**, 61-80.
- Ek, M.B., and A.A.M. Holtslag, 2004: Influence of soil moisture on boundary layer cloud development. *J. Hydromet.*, **5**, 86-99.
- Forrer, J., and M.W. Rotach, 1997: On the turbulence structure in the stable boundary layer over the Greenland ice sheet. *Bound.-Layer Meteor.*, **85**, 111-136.

- Frentzen, P., and A.G. Vogel, 2001: Further studies of atmospheric turbulence in layers near the surface: scaling the TKE budget above the surface layer. *Bound.-Layer Meteor.*, **99**, 173-206.
- Gaffard, C., L. Bianco, V. Klaus, and M. Matabuena, 2006: Evaluation of moments from wind profiler spectra: a comparison between five different processing techniques. *Meteor. Z.*, **15**, 73-85.
- Garratt, J.R., 1985: Inland boundary layer at low latitudes. Part 1, the nocturnal jet. *Bound.-Layer Meteor.*, **32**, 307-327.
- Garratt, J.R., and R.A. Brost, 1981: Radiative cooling effects within and above the nocturnal boundary layer. *J. Atm. Sci.*, **38**, 2730-2746.
- Ghan, S.J., X. Bian, and L. Corsetti, 1996: Simulation of the Great Plains low-level jet and associated clouds by general circulation models. *Mon. Wea. Rev.*, **124**, 1388-1408.
- Hartogensis, O.K., and H.A.R. de Bruin, 2005: Monin-Obukhov similarity functions of the structure parameter of temperature and turbulent kinetic energy dissipation rate in the stable boundary layer. *Bound.-Layer Meteor.*, **116**, 253-276.
- Haylock, M.R., N. Hofstra, A.M.G. Klein Tank, E.J. Klok, P.D. Jones, and M. New, 2008: A European daily high-resolution gridded data set of surface temperature and precipitation for 1950-2006. *J. Geophys. Res.*, **113**, D20119.
- Hicks, B.B., 1978: Some limitations of dimensional analysis and power laws. *Bound.-Layer Meteor.*, **14**, 567-569.
- Hicks, B.B., 1981: An examination of turbulence statistics in the surface boundary layer. *Bound.-Layer Meteor.*, **21**, 389-402.
- Högström, U., 1988: Non-dimensional wind and temperature profiles in the atmospheric surface layer: A Re-evaluation. *Bound.-Layer Meteor.*, **42**, 55-78.
- Högström, U., 1996: Review of some basic characteristics of the atmospheric surface layer. *Bound.-Layer Meteor.*, **78**, 215-246.
- Holtslag, A.A.M., 1998: Modelling of atmospheric boundary layers. In: A. A. M. Holtslag and P. G. Duynkerke (eds.), *Clear and Cloudy Boundary Layers*, Royal Netherlands Academy of Arts and Sciences, Amsterdam, pp. 287-304.
- Holtslag, A.A.M., 2006: GEWEX atmospheric boundary-layer study (GABLS) on stable boundary layers. *Bound.-Layer Meteor.*, **118**, 85-110.
- Holtslag, A.A.M., and F.T.M. Nieuwstadt, 1986: Scaling the atmospheric boundary layer. *Bound.-Layer Meteor.*, **36**, 201-209.
- Holtslag, A.A.M., and H.A.R. de Bruin, 1988: Applied modeling of the nighttime surface energy balance over land. *J. Appl. Meteor.*, **27**, 689-704.

- Holtstag, A.A.M., and B.A. Boville, 1993: Local versus nonlocal boundary-layer diffusion in a global climate model. *J. Climate*, **6**, 1825-1842.
- Holtstag, A.A.M., G.J. Steeneveld, and B.J.H. van de Wiel, 2007: Role of land surface temperature feedback on model performance for stable boundary layers. *Bound.-Layer Meteor.*, **125**, 361-376.
- Holton, J.R., 1967: The diurnal boundary layer wind oscillation above sloping terrain. *Tellus*, **19**, 199-205.
- Holton, J.R., 1992: *An introduction to dynamic meteorology*. Academic Press, San Diego, 511 pp.
- Howell, J.F., and J. Sun, 1999: Surface-layer fluxes in stable conditions. *Bound.-Layer Meteor.*, **90**, 495-520.
- Jacobs, A.F.G., B.G. Heusinkveld, and A.A.M. Holtstag, 2003: Carbon dioxide and water vapour flux densities over a grassland area in the Netherlands. *Int. J. Climatol.*, **23**, 1663-1675.
- Jacobs, A.F.G., B.G. Heusinkveld, R.J. Wichink Kruit, and S.M. Berkowicz, 2006: Contribution of dew to the water budget of a grassland area in the Netherlands. *Water Resour. Res.*, **42**, W03415.
- Jiang, X, N.C. Lau, I.M. Held, and J.J. Ploshay, 2007: Mechanisms of the Great Plains low-level jet as simulated in an AGCM. *J. Atmos. Sci.*, **64**, 532-547.
- Johansson, C., A.S. Smedman, U. Högström, J.G. Brasseur and S. Khanna, 2001: Critical test of the validity of Monin-Obukhov Similarity during convective conditions. *J. Atmos. Sci.*, **58**, 1549-1566.
- Jones, C.G., G. Lenderink, and L.I. Ivarsson, 2003: Representing subgrid scale mixing under stable conditions: importance for overall model synoptic development. *Hirlam Newsletter*, **43**, 125-134.
- Kaimal, J.C., and J.E. Gaynor, 1991: Another look at sonic thermometry. *Bound.-Layer Meteor.*, **56**, 401-410.
- Karipot, A., M.Y. Leclerc, G. Zhang, T. Martin, G. Starr, D. Hollinger, J.H. McCaughey, and G.R. Hendrey, 2006: Nocturnal CO₂ exchange over a tall forest canopy associated with intermittent low-level jet activity. *Theor. Appl. Climatol.*, **85**, 243-248.
- Kastner-Klein, P., E. Fedorovich, M. Ketzel, R. Berkowicz, and R. Britter, 2003: The modelling of turbulence from traffic in urban dispersion models – Part II: Evaluation against laboratory and full-scale concentration measurements in street canyons. *Env. Fluid. Mech.*, **3**, 145-172.
- Kenney, B.C., 1982: Beware of spurious self-correlations! *Water Resour. Res.*, **18**, 1041-1048.
- Kim, J., and L. Mahrt, 1992: Simple formulation of mixing in the stable free atmosphere and nocturnal boundary layer. *Tellus*, **44A**, 381-394.

- Kim, J.H., 1999: Spurious correlation between ratios with a common divisor. *Statistics & Probability Letters*, **44**, 383-386.
- King, J.C., W.M. Connolley, and S.H. Derbyshire, 2001: Sensitivity of modelled Antarctic climate to surface and boundary-layer flux parameterizations. *Q. J. Roy. Meteor. Soc.*, **127**, 779-794.
- King, J.C., A. Jrrar, and W.M. Connolley, 2007: Sensitivity of modelled atmospheric circulation to the representaion of stable boundary layer processes. *Geophys. Res. Letters*, **34**, L06708.
- Klein Baltink, H., 1998: A long-term intercomparison of windprofiler/RASS and tower measurements. *Meteor. Z.*, **7**, 271-279.
- Klipp, C.L., and L. Mahrt, 2004: Flux-gradient relationship, self-correlation and intermittency in the stable boundary layer. *Q. J. Roy. Meteor. Soc.*, **130**, 2087-2103.
- Kondo, J., O. Kanechika, and N. Yasuda, 1978: Heat and momentum transfer under strong stability in the atmospheric surface layer. *J. Atmos. Sci.*, **35**, 1012-1021.
- Kotroni, V., and K. Lagouvardos, 1993: Low-level jet streams associated with atmospheric cold fronts: seven case studies selected from the FRONTS 87 experiment. *Geophys. Res. Lett.*, **20**, 1371-1374.
- Kraus, H., J. Malcher, and E. Schaller, 1985: A nocturnal low-level jet during PUKK. *Bound.-Layer Meteor.*, **31**, 187-195.
- Kumar, V., G. Svensson, A.A.M. Holtslag, C. Meneveau, and M. Parlange, 2009: Impact of surface flux formulations and geostrophic forcing on large-eddy simulations of the diurnal atmospheric boundary layer. *Submitted to J. Appl. Meteor. Climatol.*
- Kurzeja R.J., S. Berman, and A.H. Weber, 1991: A climatological study of the nocturnal planetary boundary layer. *Bound.-Layer Meteor.*, **54**, 105-128.
- Lapworth, A., 2006: The morning transition of the nocturnal boundary layer. *Bound.-Layer Meteor.*, **119**, 501-526.
- Lenderink, G., and A.A.M. Holtslag, 2000: Evaluation of the kinetic energy approach for modeling turbulent fluxes in stratocumulus. *Mon. Wea. Rev.*, **128**, 244-258.
- Lenderink, G., and A.A.M. Holtslag, 2004: An updated length scale formulation for turbulent mixing in clear and cloudy boundary layers. *Q. J. Roy. Meteor. Soc.*, **130**, 3405-3427.
- Lenderink, G., and A.P. Siebesma, 2004: On the role of drizzle in stratocumulus and its implications for large-eddy simulation. *Q. J. R. Meteor. Soc.*, **130**, 3429-3434.

- Lenderink, G., M.C. van Zanten, and P.G. Duynkerke, 1999: Can an E-/turbulence closure simulate entrainment in radiatively driven convective boundary layer? *J. Atm. Sci.*, **56**, 3331-3337.
- Lenderink, G., B. van den Hurk, E. van Meijgaard, A. van Ulden, and H. Cuijpers, 2003: Simulation of present-day climate in RACMO2: first results and model development. *TR-252*, KNMI, The Netherlands, 24 pp.
- Lenderink, G., A.P. Siebesma, S. Cheinet, S. Irons, C.G. Jones, P. Marquet, F. Mueller, D. Olmeda, J. Calvo, E. Sanchez, and P.M.M. Soares, 2004: The diurnal cycle of shallow cumulus clouds over land: A single column model intercomparison study. *Q. J. Roy. Meteor. Soc.*, **130**, 3339-3364.
- Lipzig, P.M., E. van Meijgaard, and J. Oerlemans, 1998: Evaluation of a regional atmospheric model for January 1993 using in-situ measurements from the Antarctic. *Ann. Glaciol.*, **27**, 507-514.
- Lock, A., and J. Mailhot, 2006: Combining non-local scalings with a TKE closure for mixing in boundary layer clouds. *Bound.-Layer Meteor.*, **121**, 313-338.
- Louis, J.F., M. Tiedtke, and J.F. Geleyn, 1982: A short history of the PBL parameterization at ECMWF. *Workshop on Boundary Layer Parameterization*, ECMWF, U.K., pp. 59-79.
- Lundquist, J.K., 2003: Intermittent and elliptical inertial oscillations in the atmospheric boundary layer. *J. Atmos. Sci.*, **60**, 2661-2673.
- Maddox, R.A., 1983: Large-scale meteorological conditions associated with mid-latitude mesoscale convective complexes. *Mon. Wea. Rev.*, **111**, 1475-1493.
- Mahrt, L., 1987: Grid-averaged surface fluxes. *Mon. Wea. Rev.*, **115**, 1550-1560.
- Mahrt, L., 1999: Stratified atmospheric boundary layers. *Bound.-Layer Meteor.*, **90**, 375-396.
- Mahrt, L., 2007: The influence of nonstationarity on the turbulent flux-gradient relationship for stable stratification. *Bound.-Layer Meteor.*, **125**, 245-264.
- Mahrt, L., and D. Vickers, 2003: Formulation of turbulent fluxes in the stable boundary layer. *J. Atmos. Sci.*, **60**, 2538-2548.
- Mahrt, L., J. Sun, W. Blumen, W. Delany, and S. Oncley, 1998: Nocturnal boundary layer regimes. *Bound.-Layer Meteor.*, **88**, 255-278.
- Mailot, J., and R. Benoit, 1982: A finite-element model of the atmospheric boundary layer suitable for use with numerical weather prediction models. *J. Atmos. Sci.*, **39**, 2249-2266.
- Martín, F., S.N. Crespi, and M. Palacice, 2001: Simulations of mesoscale circulations in the center of the Iberian Peninsula for thermal low pressure conditions. Part I: Evaluation of the topography vorticity-mode mesoscale model. *J. Appl. Meteor.*, **40**, 880-904.

- Mathieu, N., I.B. Strachan, M.Y. Leclerc, A. Karipot, and E. Pattey, 2005: Role of low-level jets and boundary layer properties on the NBL budget technique. *Agr. Forest Meteor.*, **135**, 35-43.
- Mauritsen, T., and G. Svensson, 2007: Observations of stably stratified shear-driven atmospheric turbulence at low and high Richardson numbers. *J. Atmos. Sci.*, **64**, 645-655.
- Mauritsen, T., G. Svensson, S.S. Zilitinkevich, I. Esau, L. Enger, and B. Grisogono, 2007: A total turbulent energy closure model for neutrally and stably stratified atmospheric boundary layers. *J. Atmos. Sci.* **64** : 4113-4126.
- McCabe, A., and A.R. Brown, 2007: The role of surface heterogeneity in modeling the stable boundary layer. *Bound.-Layer Meteor.*, **122**, 517-534.
- McNider, R.T., and R.A. Pielke, 1981: Diurnal boundary layer development over sloping terrain. *J. Atmos. Sci.*, **38**, 2198-2212.
- Means, L.L., 1952: On thunderstorm forecasting in the central United States. *Mon. Wea. Rev.*, **80**, 165-189.
- Meijgaard, E. van, L.H. van Uft, W.J. van de Berg, F.C. Bosveld, B.J.J.M. van den Hurk, G. Lenderink, and A.P. Siebesma, 2008: The KNMI regional atmospheric climate model RACMO, version 2.1. *KNMI Technical Report 302*, 43 pp. Available from KNMI, Postbus 201, 3730 AE, De Bilt, The Netherlands.
- Mellor, G.L., and Yamada, T., 1974: A hierarchy of turbulence closure models for planetary boundary layers, *J. Atmos. Sci.*, **31**, 1791-1806.
- Mellor, G.L., and Yamada, T., 1982: Development of a turbulence closure model for geophysical fluid problems. *Rev. Geophys.*, **20**, 851-875.
- Miles, J.W., 1961: On the stability of heterogenous shear flows. *J. Fluid Mech.*, **10**, 496-508.
- Moberg, A., and P.D. Jones, 2004: Regional climate model simulations of daily maximum and minimum near-surface temperatures across Europe compared with observed station data 1961-1990. *Climate Dyn.*, **23**, 695-715.
- Monin, A.S., and A.M. Obukhov, 1954: Basic laws of turbulent mixing in the atmosphere near the ground. *Trudy Geofiz. Inst. AN SSSR*, **24**, 163-187.
- Monteith, J.L., 1981: Evaporation and surface temperature. *Q. J. Roy. Meteor. Soc.*, **107**, 1-27.
- Neggers, R.A.J., 2008: The KNMI Parameterization Testbed: Motivation, Configuration and Preliminary results. In: *18th Symposium on Boundary Layer and Turbulence*. Stockholm, Sweden, Amer. Met. Soc., Boston, 8A.7.

- Neggers, R.A.J., M. Köhler, and A.C.M. Beljaars, 2009: A dual mass flux framework for boundary layer convection. Part I: Transport. *To appear in J. Atmos. Sci.*
- Nieuwstadt, F.T.M., 1984: The turbulent structure of the stable, nocturnal boundary layer. *J. Atmos. Sci.*, **41**, 2202-2217.
- Obukhov, M., 1971: Turbulence in an atmosphere with a non-uniform temperature. *Bound.-Layer Meteor.*, **2**, 7-29.
- Ohya, Y., R. Nakamura, and T. Uchida, 2008: Intermittent bursting of turbulence in a stable boundary layer with low-level jet. *Bound.-Layer Meteor.*, **126**, 349-363.
- Oncley, S.P., C.A. Friehe, J.C. Larue, J.A. Businger, E.C. Itsweire, and S.S. Chang, 1996: Surface-layer fluxes, profiles, and turbulence measurements over uniform terrain under near-neutral conditions. *J. Atmos. Sci.*, **53**, 1029-1044.
- Parish, T. R., A.R. Rodi, and R.D. Clark, 1988: A case study of the summertime Great Plains low level jet. *Mon. Wea. Rev.*, **116**, 94-105.
- Poulos, G.S., W. Blumen, D. Fritts, J.L. Lundquist, J. Sun, S.P. Burns, C. Nappo, R. Banta, R. Newsom, J. Cuxart, E. Terradellas, B. Balsey, and M. Jensen, 2002: CASES-99: A comprehensive investigation of the stable nocturnal boundary layer. *Bull. Amer. Meteor. Soc.*, **83**, 555-581.
- Prandtl, L., 1925: Bericht über Untersuchungen zur ausgebildeten Turbulenz. *Z. Angew. Math. Mech.*, **5**, 136-139.
- Rama Krishna, T.V.B.P.S., M. Sharan, S.G. Gopalakrishnan, and Aditi, 2003: Mean structure of the nocturnal boundary layer under strong and weak wind conditions: EPRI case study. *J. Appl. Meteor.*, **42**, 952-969.
- Raupach, M.R., J.J. Finnigan, and Y. Brunet, 1996: Coherent eddies and turbulence in vegetation canopies: the mixing-layer analogy. *Bound.-Layer Meteor.*, **78**, 351-382.
- Reynolds, O., 1895: On the dynamical theory of incompressible viscous fluids and the determination of the criterion. *Philos. Trans. R. Soc.*, **186**, 123-164.
- Ronda, R.J., and H.A.R. de Bruin, 1999: A note on the concept of 'effective' bulk exchange coefficients for determination of surface flux densities. *Bound.-Layer Meteor.*, **93**, 155-162.
- Roode, S.R. de, F.C. Bosveld, and P.S. Kroon, 2009: Dew formation, eddy-correlation latent heat fluxes, and the surface energy imbalance at Cabauw during stable conditions. *Submitted to Bound.-Layer Meteor.*
- Salmond, J.A., and I.G. McKendry, 2005: A review of turbulence in the very stable nocturnal boundary layer and its implications for air quality. *Progress Phys. Geography*, **29**, 171-188.

- Schumann, U., and T. Gerz, 1995: Turbulent mixing in stably stratified shear flows. *J. Appl. Meteor.*, **34**, 33-48.
- Sharan, M., and S.G. Gopalakrishnan, 1997: Comparative evaluation of eddy exchange coefficients for strong and weak wind stable boundary layer modeling. *J. Appl. Meteor.*, **36**, 545-559.
- Siebesma, A.P., P.M.M. Soares, and J. Teixeira, 2007: A combined eddy-diffusivity mass-flux approach for the convective boundary layer. *J. Atmos. Sci.*, **64**, 1230-1248.
- Smedman, A.S., M. Tjernström, and U. Högström, 1993: Analysis of the turbulence structure of a marine low-level jet. *Bound.-Layer Meteor.*, **66**, 105-126.
- Song, J., K. Liao, R.L. Coulter, and B.M. Lesht, 2005: Climatology of the low-level jet at the southern Great Plains Atmospheric Boundary Layer Experiment Site, *J. Appl. Meteor.*, **44**, 1593-1606.
- Sorbjan, Z., 2006: Local structure of turbulence in stably-stratified boundary layers. *J. Atmos. Sci.*, **63**, 1526-1537.
- Steenefeld, G.J., 2007: *Understanding and prediction of stable atmospheric boundary layers over land*, PhD thesis, Wageningen University, 199 pp.
- Steenefeld, G.J., B.J.H. van de Wiel, and A.A.M. Holtslag, 2006: Modeling the evolution of the atmospheric boundary layer for three contrasting nights in CASES-99. *J. Atmos. Sci.*, **63**, 920-935.
- Steenefeld, G.J., B.J.H. van de Wiel, and A.A.M. Holtslag, 2007: Diagnostic equations for the stable boundary layer height: evaluation and dimensional analysis. *J. Appl. Meteor. Climatol.*, **46**, 212-225.
- Steenefeld, G.J., T. Mauritsen, E.I.F. de Bruijn, J. Vilà-Guerau de Arellano, G. Svensson, and A.A.M. Holtslag, 2008a: Evaluation of limited area models for the representation of the diurnal cycle and contrasting nights in CASES99. *J. Appl. Meteor. Climatol.*, **47**, 869-887.
- Steenefeld, G.J., A.A.M. Holtslag, C.J. Nappo, B.J.H. van de Wiel, and L. Mahrt, 2008b: Exploring the possible role of small-scale terrain drag on stable boundary layers over land. *J. Appl. Meteor. Climatol.*, **47**, 2518-2530.
- Steenefeld, G.J., M.J.J. Wokke, C.D. Groot-Zwaafink, S. Pijlman, B.G. Heusinkveld, A.F.G. Jacobs, and A.A.M. Holtslag, 2008c: Long term observations of longwave radiative flux divergence in the stable boundary layer over land. *18th Symposium on Boundary Layers and Turbulence*, Stockholm, Sweden, Amer. Meteorol. Soc., Boston, 17B.6.
- Stensrud, D.J., 1996: Importance of low-level jets to climate: a review. *J. Climate*, **9**, 1698-1711.

- Storm, B., J. Dudhia, S. Basu, A. Swift, and I. Giammanco, 2009: Evaluation of the Weather Research and Forecasting Model on forecasting low-level jets: implications for wind energy. *Wind Energy*, **12**, 81-90.
- Stull, R.B., 1988: *An Introduction to Boundary Layer Meteorology*. Kluwer Academic Publishers, Boston, 666 pp.
- Svensson, G., and A.A.M. Holtslag, 2006: Single column modeling of the diurnal cycle based on CASES99 data – GABLS second intercomparison project. *In: 17th Symposium on Boundary Layers and Turbulence*, San Diego, CA, U.S.A., May 22-25, 2006, Amer. Meteorol. Soc., Boston, p. 8.1.
- Svensson, G., and A.A.M. Holtslag, 2009: Modelling the turning of the wind with height in the stable boundary layer. *Accepted in Bound.-Layer Meteorol.*
- Teixeira, J., B. Stevens, C.S. Bretherton, R. Cederwall, J.D. Doyle, J.C. Golaz, A.A.M. Holtslag, S.A. Klein, J.K. Lundquist, D.A. Randall, A.P. Siebesma, and P.M.M. Soares, 2008: Parameterization of the atmospheric boundary layer. A view from just above the inversion. *Bull. Amer. Met. Soc.*, **89**, 453-458.
- Thorpe, A.J., and Guymer, T.H., 1977: The nocturnal jet. *Q. J. Roy. Meteor. Soc.*, **103**, 633-653.
- Tijm, A.B.C., 2004: Tuning CBR. *Hirham Newsletter*, **46**, 18-28.
- Tijm, A.B.C., A.J. van Delden, and A.A.M. Holtslag, 1999: The inland penetration of sea breezes. *Contr. Atmos. Phys.*, **72**, 317-328.
- Tjemkes, S.A., and P.G. Duynkerke, 1989: The nocturnal boundary layer: model calculations compared with observations. *J. Appl. Meteor.*, **28**, 161-175.
- Todd, M.C., R. Washington, S. Raghavan, G. Lizcano, and P. Knippertz, 2008: Regional model simulations of the Bodélé low-level jet of northern Chad during the Bodélé Dust Experiment (BoDEx 2005). *J. Climate*, **21**, 995-1012.
- Ulden, A.P. van, and A.A.M. Holtslag, 1985: Estimation of atmospheric boundary layer parameters for diffusion applications. *J. Climate Appl. Meteor.*, **24**, 1196-1207.
- Ulden, A.P. van, and J. Wieringa, 1996: Atmospheric boundary layer research at Cabauw. *Bound.-Layer Meteor.*, **78**, 39-69.
- Umlauf, L., and H. Burchard, 2005: Second-order turbulence closure models for geophysical boundary layers. A review of recent work. *Cont. Shelf Res.*, **25**, 795-827.
- Uppala, S.M., P.W. Kållberg, A.J. Simmons, U. Andrae, V. da Costa Bechtold, M. Fiorino, J.K. Gibson, J. Haseler, A. Hernandez, G.A. Kelly, X. Li, K. Onogi, S. Saarinen, N. Sokka, R.P. Allan, E. Andersson, K. Arpe, M.A. Balmaseda, A.C.M. Beljaars, L. van de Berg, J. Bidlot, N. Bormann, S. Caires, F. Chevallier, A. Dethof, M. Dragosavac, M. Fisher, M. Fuentes, S.

- Hagemann, E. Hólm, B.J. Hoskins, L. Isaksen, P.A.E.M. Janssen, R. Jenne, A.P. McNally, J.F. Mahfouf, J.J. Morcrette, N.A. Rayner, R.W. Saunders, P. Simon, A. Sterl, K.E. Trenberth, A. Untch, D. Vasiljevic, P. Viterbo, and J. Woollen, 2005: The ERA-40 re-analysis. *Q. J. R. Meteor. Soc.*, **131**, 2961-3012.
- Velde, I.R. van der, G.J. Steeneveld, B.G.J. Wichers Schreur, and A.A.M. Holtslag, 2009: Modeling and forecasting the onset and duration of a severe Dutch fog event. *Submitted to Mon. Wea. Rev.*
- Verkaik, J. W., and A. A. M. Holtslag, 2007: Wind profiles, momentum fluxes and roughness lengths at Cabauw revisited. *Bound.-Layer Meteor.*, **122**, 701-719.
- Vickers, D., and L. Mahrt, 2003: The cospectral gap and turbulent flux calculations. *J. Atmos. Ocean Tech.*, **20**, 660-672.
- Viterbo, P., A.C.M. Beljaars, J.F. Mahfouf, and J. Teixeira, 1999: The representation of soil moisture freezing and its impact on the stable boundary layer. *Q. J. Roy. Meteor. Soc.*, **125**, 2401-2426.
- Weng, W., and P.A. Taylor, 2003: On modelling the one-dimensional atmospheric boundary layer. *Bound.-Layer Meteor.*, **107**, 371-400.
- Whiteman, C. D, X. Bian, and S. Zhong, 1997: Low-level jet climatology from enhanced rawinsonde observations at a site in the Southern Great Plains. *J. Appl. Meteor.*, **36**, 1363-1376.
- Wiel, B.J.H. van de, 2002: *Intermittent turbulence and oscillations in the stable boundary layer over land*. PhD thesis, Wageningen University, 130pp.
- Wiel, B.J.H. van de, R.J. Ronda, A.F. Moene, H.A.R. de Bruin, and A.A.M. Holtslag, 2002: Intermittent turbulence and oscillations in the stable boundary layer over land. Part I: A bulk model. *J. Atmos. Sci.*, **59**, 942-958.
- Wiel, B.J.H. van de, A.F. Moene, O.K. Hartogensis, H.A.R. de Bruin, and A.A.M. Holtslag, 2003: Intermittent turbulence and oscillations in the stable boundary layer over land. Part III: A classification for observations during CASES99. *J. Atmos. Sci.*, **60**, 2509-2522.
- Wiel, B.J.H. van de, A.F. Moene, G.J. Steeneveld, O.K. Hartogensis, and A.A.M. Holtslag, 2007: Predicting the collapse of turbulence in stably stratified boundary layers. *Flow, Turb. and Comb.*, **79**, 251-274.
- Wiel, B.J.H. van de, A.F. Moene, W.H. De Ronde, and H.J.J. Jonker, 2008: Local similarity in the stable boundary layer and mixing-length approaches: consistency of concepts. *Bound.-Layer Meteor.*, **128**, 103-116.
- Wilczak, J.M., M.L. Cancillo, and C.W. King, 1997: A wind profiler climatology of boundary layer structure above the boreal forest. *J. Geophys. Res.*, **102**, 29.083-29.100.

- Wippermann, F., 1973: Numerical study on the effects controlling the low-level jet. *Beitr. Phys. Atmos.*, **46**, 137-154.
- Wyngaard, J.C., and O.R. Coté, 1974: The evolution of a convective planetary boundary layer – a higher-order-closure model study. *Bound.-Layer Meteor.*, **7**, 289-308.
- Yagüe, C., G. Maqueda and J. M. Rees, 2001: Characteristics of turbulence in the lower atmosphere at Halley IV station, Antarctica. *Dyn. Atmos. Oceans*, **34**, 205-223.
- Zanten M van, and co-authors, 2009: Large-eddy simulations of precipitating shallow cumuli., *Submitted to J. Atmos. Sci.*
- Zhang, K, H. Mao, K. Civerolo, S. Berman, J.Y. Ku, S.T. Rao, B. Doddridge, C.R. Philbrick, and R. Clark, 2001: Numerical investigation of boundary layer evolution and nocturnal low-level jets: local versus non-local PBL schemes. *Env. Fluid Mech.*, **1**, 171-208.
- Zhong, S., J.D. Fast, and X. Bian, 1996: A case study of the Great Plains low-level jet using wind profiler network data and a high-resolution mesoscale model. *Mon. Wea. Rev.*, **124**, 785-806.
- Zilitinkevich, S.S., 2002: Third-order transport due to internal waves and non-local turbulence in the stably stratified boundary layer. *Q. J. Roy. Meteor. Soc.*, **128**, 913-925.
- Zilitinkevich, S.S., and I.N. Esau, 2007: Similarity theory and calculation of turbulent fluxes at the surface for the stably stratified atmospheric boundary layer. *Bound.-Layer Meteor.*, **125**, 193-205.
- Zilitinkevich, S.S., T. Elperin, N. Kleeorin, and I. Rogachevskii, 2007: Energy- and flux-budget (EFB) turbulence closure model for stably stratified flows. Part I: steady-state, homogeneous regimes. *Bound.-Layer Meteor.*, **125**, 167-191.

Nederlandse samenvatting

Het onderwerp van dit proefschrift is de nachtelijke stabiele grenslaag boven land. De stabiele grenslaag ontstaat na zonsondergang, wanneer de langgolvlige stralingsafkoeling van het aardoppervlak niet meer gecompenseerd wordt door kortgolvlige straling van de zon. Hierdoor koelt het oppervlak af, waardoor lucht vlak boven het oppervlak een stabiele gelaagdheid krijgt. Dit betekent dat de temperatuur gaat toenemen met de hoogte. Een belangrijke eigenschap van stabiel gelaagde stromingen is dat verticale bewegingen (turbulentie) onderdrukt worden door *buoyancy* effecten: luchtpakketjes die vertikaal verplaatst worden in een stabiele omgeving neigen ernaar terug te bewegen naar hun oorspronkelijke positie als gevolg van de zwaartekracht. Aan de top van de stabiele grenslaag wordt vaak een maximum in het verticale windsnelheidsprofiel waargenomen. Dit verschijnsel wordt de nachtelijke *low-level jet* (LLJ) genoemd. Het ontstaat na zonsondergang als reactie op het plotselinge wegvallen van de hevige turbulentie van de convectieve grenslaag.

In de stabiele grenslaag spelen vele fysische processen een rol, bijvoorbeeld turbulentie, stralingstransport, zwaartekrachtsgolven, stromingen langs hellingen en interacties met het landoppervlak. De complexe interacties tussen deze processen bemoeilijken het modelleren van de stabiele grenslaag, vooral in situaties waarin de wind zwak is. Dit proefschrift heeft als doel een bijdrage te leveren aan de het begrijpen van processen die in de stabiele grenslaag een rol spelen, in het bijzonder turbulentie en de ontwikkeling van de LLJ. Een ander doel is om diverse turbulentieschema's uit de literatuur te testen in een *single-column model* (SCM) en om de resultaten te vergelijken met waarnemingen. Tenslotte is het de bedoeling een klimatologie en classificatie te maken van stabiele-grenslaag waarnemingen die geschikt is om de prestaties van atmosferische modellen te evalueren.

Hoofdstuk 2 presenteert een klimatologie van LLJs in Cabauw. Zeven jaar data van een 200-m mast en een windprofiler systeem zijn geanalyseerd om eigenschappen van de LLJ te bepalen. In dit onderzoek wordt een LLJ gedefinieerd als een maximum in het windsnelheidsprofiel in de onderste 500 m van de atmosfeer. Om als LLJ geclassificeerd te worden, moet de afname van de windsnelheid boven een windmaximum zowel groter dan 2 m s^{-1} als 20% van het waargenomen maximum zijn. Voor elke nacht is alleen het windprofiel zes uur na zonsondergang geanalyseerd. Dit garandeert dat de waargenomen LLJs zich ongeveer in dezelfde fase van hun ontwikkeling bevinden. Op dit tijdstip bereiken LLJs bij benadering hun maximale sterkte. In ruwweg 20% van de nachten wordt in Cabauw een maximum in het windprofiel geobserveerd. De LLJs bevinden zich

gemiddeld 140 tot 200 m boven het oppervlak en hebben een snelheid van 6 tot 10 m s^{-1} .

De waarnemingen zijn geclassificeerd in termen van de twee belangrijkste forceringen van de stabiele grenslaag, namelijk de geostrofe windsnelheid en de stralingsafkoeling. Op deze manier worden negen stabiele-grenslaag klassen gedefiniëerd, variërend van onbewolkte en windstille omstandigheden tot bewolkte en winderige omstandigheden. Voor elk van deze klassen zijn LLJ eigenschappen bepaald. Significante LLJs komen het vaakst voor in het geval van een matige geostrofe wind in combinatie met een onbewolkte hemel. In het algemeen blijkt dat de frequentie van voorkomen van LLJs toeneemt met afnemende wind en met toenemende stralingsafkoeling. De draaiing van de windvector tussen de ‘neus’ van de LLJ en het oppervlak lijkt niet erg gevoelig voor de grootte van de geostrofe wind, maar neemt toe naarmate de stralingsafkoeling toeneemt. De gemiddelde hoogte van de LLJ neemt toe met een sterkere geostrofe wind en met een mindere afkoeling.

Een vergelijking van de waargenomen klimatologie met model *reanalysis* (ERA40) illustreert het potentieel voor model evaluatie. In ERA40 worden de frequentie van voorkomen van LLJs en de winddraaiing tussen de jet en het oppervlak onderschat. Verder bevinden de LLJs zich in het algemeen op een hoger niveau dan de in waarnemingen.

De representatie van LLJs in atmosferische modellen hangt af van de manier waarop turbulente menging geformuleerd is. Turbulentie kan niet direct opgelost worden, maar moeten worden geparameteriseerd. In veel modellen worden effecten van stabiliteit meegenomen door gebruik te maken van de semi-empirische flux-gradiënt relaties. Hoofdstuk 3 presenteert een kritische discussie over deze relaties. In de literatuur blijkt steeds weer dat de spreiding in de dimensieloze temperatuurgradiënt, ϕ_h , veel groter is dan in de dimensieloze windgradiënt, ϕ_m , als deze grootheden geplot worden tegen de stabiliteitsparameter z/Λ (hier staat Λ voor de lokale Obukhov lengte). Hoofdstuk 3 laat zien dat dit verschijnsel een resultaat is van schijnrelatie, die ontstaat doordat de x en y-as gemeenschappelijke variabelen hebben. Schijnrelatie is een wiskundig effect wat spreiding in scatterplots maskeert. Het blijkt dat hierdoor de spreiding in ϕ_m kunstmatig onderdrukt wordt, terwijl dit bij ϕ_h niet het geval is. In het geval van ϕ_m kan dit leiden tot onterecht vertrouwen in de gevonden relaties, zeker voor zeer stabiele omstandigheden wanneer meetfouten aanzienlijk kunnen zijn. Om schijnrelatie en de grote relatieve fouten gerelateerd aan de op fluxen gebaseerde Monin-Obukhov theorie te vermijden, wordt voorgesteld om in plaats daarvan en schalingsmethode gebaseerd op gradiënten toe te passen.

Flux-gradiënt relaties worden toegepast in zogenaamde eerste-orde turbulentieschema's, waarbij de grootte van de flux direct gerelateerd is aan de

lokale gradiënt van de gemiddelde grootheid. Een andere populaire manier om turbulentie te modelleren is de zogenaamde 1.5-orde of turbulente kinetische energie (TKE) sluitingsmethode. In dit geval wordt de efficiëntie van turbulente menging beschreven als een functie van de TKE, die nu prognostisch opgelost moet worden. Hoofdstuk 4 bespreekt hoe het schalingsgedrag van een TKE schema zich verhoudt tot de flux-gradiënt relaties van Hoofdstuk 3. De analyse is gedaan met een *single-column model* (SCM). Uitgaande van de modelvergelijkingen zijn uitdrukkingen afgeleid voor de stabiele limiet van het TKE schema in termen van de flux-gradiënt relaties. Het blijkt dat slechts een paar parameters het schalingsgedrag van het model bepalen en dat het model strik de theorie van lokale schaling volgt. De analytische resultaten worden geïllustreerd met model runs van de tweede GEWEX Atmospheric Boundary Layer Studies (GABLS) vergelijkingsstudie. De situatie waarin een empirische correctiefunctie is opgenomen die bij een toenemend Richardson getal de menging van momentum laat toenemen ten opzichte van de menging van warmte is apart bestudeerd. Het blijkt dat het opnemen van dergelijke empirische correctiefuncties ongewenste effecten kunnen hebben op het gedrag van het model.

In Hoofdstuk 5 komt veel van de in eerdere hoofdstukken besproken materie samen. SCMs worden veel gebruikt om grenslaag parameterisaties te testen. Echter, om deze modellen te kunnen gebruiken moeten grootschalige forceringen, zoals de geostrofe wind en de advectieve tendensen, worden voorgeschreven. Helaas zijn deze forceringen intrinsiek onzeker en zijn ze niet zelden verstoord door mesoschaal fenomenen. Dit bemoeilijkt een vergelijking van SCM resultaten met waarnemingen. Een belangrijke vraag is dan ook: kunnen waarnemingen eigenlijk wel gebruikt worden om onderscheid te maken tussen verschillende parameterisaties of is de spreiding als gevolg van onzekerheden in de forceringen simpelweg te groot? Hoofdstuk 5 onderzoekt deze vraag voor de nachtelijke LLJ.

Ten eerste is een individuele LLJ geanalyseerd. Dezelfde case is gebruikt voor de derde GABLS vergelijkingsstudie. Om de grootschalige forceringen te kunnen schatten is gebruik gemaakt van een mengeling van waarnemingen en modeluitvoer. Met het SCM van het ECMWF-model is een gevoeligheidsstudie gedaan naar zowel de invloed van de forceringen als naar die van de formulering van de turbulente menging. Het blijkt dat de gevoeligheid voor de modelfysica het grootst is in het middelste deel van de stabiele grenslaag, terwijl de invloed van de forceringen zich vooral manifesteert in het bovenste gedeelte van de stabiele grenslaag en in de residulaag erboven.

Ten tweede is een ensemble van LLJ nachten onderzocht. Uit de database van Cabauw waarnemingen zijn acht nachten met vergelijkbare LLJs geselecteerd. Deze nachten zijn gedraaid met het SCM, waarbij de forceringen direct afgeleid

zijn uit modelruns van 3D model. De SCM resultaten van de individuele nachten vertonen aanzienlijke verschillen met de waarnemingen. Dit laat zien dat forceringen afgeleid van 3D model uitvoer niet geschikt is voor een vergelijking op basis van een enkele case. Echter, het gemiddelde van de acht SCM integraties komt goed overeen met het gemiddelde van de waarnemingen. Door de forceringen van de acht nachten te middelen is een samengestelde case gedefinieerd. De overeenkomst tussen de resultaten van de samengestelde SCM case en de samengestelde waarnemingen is goed. De resultaten laten zien dat als meerdere gevallen worden beschouwd, het gebruik van forceringen afgeleid van 3D model uitvoer wel goede resultaten geeft. Blijkbaar middelen in dit geval willekeurig verspreide mesoschaal verstoring uit. Het gebruik van een samengestelde case maakt het mogelijk om beter onderscheid te kunnen maken tussen verschillende parameterisaties in een vergelijking met waarnemingen.

Dankwoord

Een proefschrift schrijven doe je niet alleen. Daarom wil ik hier graag een aantal mensen bedanken. Als eerste mijn promotor Bert Holtslag. Onder jouw leiding werd het NWO voorstel binnengehaald. Bedankt voor de vele motiverende gesprekken, de creatieve suggesties en de opbouwende kritiek op mijn werk. Altijd op zoek naar ‘wat kunnen we hier nu eigenlijk mee?’. Je hebt me steeds gestimuleerd nieuwe resultaten te presenteren op conferenties en symposia, wat denk ik erg belangrijk is.

Fred Bosveld, co-promotor en dagelijks begeleider, bedankt voor je inzet en de fijne samenwerking. Ook al zat je zelf tot over je oren in het werk, je nam altijd rustig en ruim de tijd voor me als ik je kamer weer eens binnen kwam vallen. Je was altijd geïnteresseerd in waar ik mee bezig was en niet tevreden met snelle oplossingen. Je scherpe oog voor detail en uitgebreide commentaar op mijn artikelen heb ik erg gewaardeerd. Bedankt ook voor het beheren van het enorme archief van de Cabauw mast. Met het reuze-handige Mobibase programma had ik alle data die ik me maar kon wensen binnen no-time bij elkaar geraapt.

Waar was ik geweest zonder mijn grote schare medeauteurs? Dank voor de vele discussies, adviezen en de rood-gecorrigeerde manuscripten. Ik heb met veel plezier met jullie samengewerkt. Gert-Jan Steeneveld en Bas van de Wiel, ik hoop dat jullie ook dit derde stabiele-grenslaag proefschrift kunnen waarderen. Het afstudeervak dat ik bij jullie volgde heeft me destijds de stabiele grenslaag ingetrokken. Henk Klein Baltink, daar waar de Cabauw-mast ophoudt begint jouw domein. Hartelijk dank voor het verwerken van de windprofieler data tot een mooie dataset, zonder welke de low-level jet studie niet mogelijk was geweest. Geert Lenderink, ik heb veel geleerd van je brede kennis van atmosferische modellen. We spraken ook regelmatig over de voortgang van mijn werk. Dankjewel voor de richtinggevende tips en je realistische kijk op de zaken. Stephan de Roode, bedankt voor de inspirerende samenwerking. Samen hebben we heel wat kladjes volgend met het analyseren van de modelvergelijkingen van het TKE schema. Erik van Meijgaard, bedankt voor je grondige feedback en de steun bij het modelwerk. Zonder jullie tijd, energie en enthousiasme waren de papers van dit proefschrift er niet gekomen. Ik wil graag ook Roel Neggers en Bert van Uft bedanken voor de hulp het opzetten van de GABLS3 case en het aan de praat krijgen van 3D RACMO op mijn werkstation. Tenslotte wil ik iedereen bedanken met wie ik de afgelopen jaren op welke wijze dan ook heb samengewerkt.

Special thanks to the GABLS community. I enjoyed the stimulating discussions during the workshops. With pleasure I participated in preparing a 3rd

intercomparison case with Cabauw data. Chapter 5 of this thesis is a direct spin-off of this project.

Ik heb het geluk gehad om vier jaar lang van twee walletjes te mogen eten. Niet allen ben ik het KNMI erkentelijk voor de werkplek en de support van de afgelopen jaren, ik wil ook de leerstoelgroep Meteorologie en Luchtkwaliteit van de Wageningen Universiteit nadrukkelijk bedanken voor de werkplek waar ik elke donderdag gebruik van mocht maken. De samenwerking heb ik altijd als zeer positief ervaren en is zeker een meerwaarde geweest de afgelopen jaren.

Collega's, zowel op het KNMI als in Wageningen, bedankt voor alle koffie- en lunchpauzes, gezelligheid, fietstochten (waar dan ook...), volleybaltoernooien, afdelingsuitjes, etcetera. Papa en mama, bedankt voor alle kansen die jullie mij geboden hebben. Jantine, het heeft even geduurd, maar ik heb je dan toch over weten te halen een carrière in het weer te beginnen. Dankjewel voor je onvoorwaardelijke steun, interesse en betrokkenheid.

Hartelijk dank!

Curriculum Vitae

Pieter Baas werd geboren op 8 juli 1980 te IJsselstein. Na het doorlopen van de basisschool werd in 1998 het VWO diploma behaald aan het Ichthus-College in Veenendaal. Intussen was de interesse in de meteorologie gewekt en daarom begon hij aan de studie Bodem, Water en Atmosfeer aan de toenmalige Landbouw Universiteit te Wageningen. Na het eerste studiejaar koos hij dan ook niet verrassend voor de specialisatie Meteorologie. Het eerste afstudeervak werd gedaan onder supervisie van Adrie Jacobs. In alle vroegte werd de hoeveelheid dauwval gemeten op de grasmat van het weerstation op de Haarweg. Deze experimentele resultaten werden vervolgens vergeleken met enkele modelletjes uit de literatuur. De stage werd ingevuld op het KNMI (Hans Roozekrans), waar de mogelijkheden voor mistdetectie met satellietbeelden tijdens de nachtelijke uren werd onderzocht. Als afsluiting van de doctoraalstudie volgde een tweede afstudeervak waarin onderzoek naar de flux-profiel relaties in de stabiele grenslaag centraal stond (Bas van de Wiel en Gert-Jan Steeneveld). In april 2004 werd het BWA diploma in ontvangst genomen. In januari 2005 begon hij op het KNMI aan het OIO project waarvan dit proefschrift de resultaten beschrijft.

Publications

Peer-reviewed

- Baas, P., G.J. Steeneveld, B.J.H. van de Wiel, and A.A.M. Holtslag, 2006: Exploring self-correlation in stably stratified conditions. *J. Atmos. Sci.*, **63**, 3045-3054.
- Baas, P., S.R. de Roode, and G. Lenderink, 2008: The scaling behaviour of a turbulent kinetic energy closure model for stably stratified conditions. *Bound.-Layer Meteor.*, **127**, 17-36.
- Baas, P., F.C. Bosveld, H. Klein Baltink, and A. A. M. Holtslag, 2009: A climatology of nocturnal low-level jets at Cabauw. *J. Appl. Meteor. Climatol.*, **48**, 1627-1642.
- Baas, P., F.C. Bosveld, G. Lenderink, E. van Meijgaard, and A.A.M. Holtslag, 2009: How to design single-column model experiments for comparison with observed nocturnal low-level jets?, *Revised version for Q. J. Roy. Meteor. Soc.*
- Wiel, B.J.H. van de, A.F. Moene, G.J. Steeneveld, P. Baas, F.C. Bosveld, and A.A.M. Holtslag, 2009: A conceptual view on inertial oscillations and nocturnal low-level jets. *Submitted to J. Atmos. Sci.*

Popular Scientific

- Baas, P., F.C. Bosveld, and H. Klein Baltink, 2008: Low-level jets boven Cabauw, *Meteorologica*, **17**, 20-23.

Buys-Ballot Research School Education Plan Activities

Review of literature

- Nieuwstadt, F.T.M., 1998: *Turbulentie, inleiding in de theorie en toepassing van turbulente stromingen*, Epsilon Uitgaven, Utrecht, 211 pp.
- Frisch, U., 1995: *Turbulence, the legacy of A.N. Kolmogorov*, Cambridge University Press, Cambridge, 296 pp. Discussion group led by prof. H. Dijkstra, IMAU, December 2005.

Post-graduate courses

- Summerschool on boundary layers over complex and vegetated terrain*, Finnish Meteorological Institute, Sodankylä, Finland, June, 2005.
- Introductie cursus klimaat*, KNMI, De Bilt, June 2005.
- Parameterization of diabatic processes*, European Centre for Medium Range Weather Forecasts (ECMWF), England, May 2006.
- Writing in English for publication*, James Boswell Institute, Utrecht, May 2007.
- Summerschool on atmospheric boundary layers: Concepts, Observations, and Numerical Simulations*, IMAU / WUR, Les Houches, France, June 2008.

International Workshops, Symposia, and Conferences

- 5th Annual Meeting of the European Meteorological Society, Utrecht, The Netherlands, 12-16 September 2005.
- GLASS/GABLS Workshop on local land-atmosphere coupling, De Bilt, The Netherlands, 19-21 September 2005.
- 17th Symposium on Boundary Layers and Turbulence, San Diego (CA), USA, 22-25 May 2006, American Meteorological Society.
- GABLS Workshop on Stable Boundary Layers, Stockholm, Sweden, 19-21 June 2007.
- 7th Annual Meeting of the European Meteorological Society, Escorial, Spain, 1-5 October 2007.
- 18th Symposium on Boundary Layers and Turbulence, Stockholm, Sweden, 9-13 June 2008, American Meteorological Society.
- 8th Annual Meeting of the European Meteorological Society, Amsterdam, The Netherlands, 29 September – 3 October 2008.

Buys Ballot Research School Meetings and Seminars

- BBOS Autumn Symposia 2005-2008.
- BBOS Spring Symposium 2006-2008.
- BBOS Boundary Layer Workshop, 21 November 2005, Wageningen Univ.
- BBOS Boundary Layer Workshop, 13 October 2006, IMAU.



A school for the study of fundamental processes in the climate system

Director: Prof. dr. ir. J. D. Opsteegh
Address: IMAU, Princetonplein 5, 3584 CC Utrecht, The Netherlands
Telephone: +31 30 253 3275
Email: IMAU@phys.uu.nl
Web site: <http://www.phys.uu.nl/~wwwimau/education/bbos/home.html>

De Heer P. Baas
KNMI
Postbus 201
3730 AE De Bilt

Utrecht, 27 juli 2009

Geachte heer Baas,

Hiermee bevestig ik u dat u lid bent geweest van de Buys Ballot Onderzoekschool en het hierbij behorende opleidingsplan naar behoren hebt afgerond.
Ik heb geen bezwaar tegen de verdediging van uw proefschrift op 14 oktober 2009.
Ik wens u succes met de voortzetting van uw wetenschappelijke carrière.

Met vriendelijke groet,

Prof. dr. ir. J. D. Opsteegh,
directeur BBOS

members

associate members

institute for Marine and Atmospheric Research, Utrecht University (penvoerder)
Department of Meteorology and Air Quality, Wageningen University
Royal Netherlands Meteorological Institute (KNMI)
Royal Netherlands Institute for Sea Research (NIOZ)
Research Group of Atmospheric Physics, Eindhoven University
National Institute of Public Health and the Environment (RIVM)
Max-Planck-Institut für Chemie, Mainz

Photo front cover: Cabauw tower with fog layer, photo by Jacques Warmer

The research described in this thesis was financially supported by the Netherlands Organization for Scientific Research (NWO), in particular through the project “land surface climate and the role of the stable boundary layer”.

Financial support from Wageningen University and KNMI for printing this thesis is gratefully acknowledged.

